PHYSICS AND ENGINEERING OF ORGANIC SOLAR CELLS

A Dissertation
Presented to
The Academic Faculty

By

William J. Potscavage, Jr.

In Partial Fulfillment
Of the Requirements for the Degree
Doctor of Philosophy in Electrical Engineering

Georgia Institute of Technology

May, 2011

PHYSICS AND ENGINEERING OF ORGANIC SOLAR CELLS

Approved by:

Dr. Bernard Kippelen, Advisor
School of Electrical and Computer Engineering
Georgia Institute of Technology

Dr. Miroslav M. Begovic
School of Electrical and Computer Engineering
Georgia Institute of Technology

Dr. William Alan Doolittle
School of Electrical and Computer Engineering
Georgia Institute of Technology

Dr. Elsa Reichmanis
School of Chemical and Biomolecular Engineering
Georgia Institute of Technology

Dr. Ajeet Rohatgi
School of Electrical and Computer Engineering
Georgia Institute of Technology

Date Approved: December 7, 2010

ACKNOWLEDGEMENTS

This thesis would not have been possible without the support and encouragement of many people including coworkers, friends, and family. First and foremost, I must thank Prof. Bernard Kippelen for his guidance and training throughout the past few years that will continue to be of value going forward. I am thankful to Prof. Alan Doolittle, Prof. Ajeet Rohatgi, Prof. Miroslav Begovic, and Prof. Elsa Reichmanis for taking the time to serve on my committee and evaluate my work.

Much of this work would not have been possible without the help of numerous people from both in and out of the Kippelen group. I thank Dr. Benoît Domercq and Prof. Seunghyup Yoo for getting me started and setting me on the right path. I am indebted to Dr. Andreas Haldi and Dr. Canek Fuentes-Hernandez for their support both in and out of the lab. Thank you to all of my past and present colleagues in the Kippelen group for their help and friendship.

Regarding the work in this thesis, I am particularly grateful to Dr. Peter Hotchkiss of Prof. Seth Marder's group for supplying the phosphonic acids, Dr. Asha Sharma for help with the surface modification and Kelvin probe measurements, and Dr. Seungkeun Choi for his work fabricating the grid structures. I also greatly appreciate the discussions with Prof. Ajeet Rohatgi and his group at Georgia Tech and Dr. Michael Brumbach and Prof. Neil Armstrong at the University of Arizona that helped to shape this work.

This work was made possible through the generous support of the STC Program of the National Science Foundation under Agreement No. DMR-0120967, the Office of Naval Research, the Georgia Research Alliance, Solvay S.A., and BIONIC.

Finally, I am most grateful to my family and my friends who have become family for all their support and love.

TABLE OF CONTENTS

LIST OF TABLES

LIST OF FIGURES

LIST OF SYMBOLS AND ABBREVIATIONS

η	Power-conversion efficiency
λ	Wavelength
Λ	Reorganization energy
A	Area
ALD	Atomic layer deposition
BCP	Bathocuproine
c	Speed of light (299,792,458 m/s)
CuPc	Copper phthalocyanine
e	Elementary charge (1.6×10^{-19} coul)
EQE	External quantum efficiency
F5BPA	Pentafluorobenzyl phosphonic acid
FF	Fill factor
G_0	Gibbs free energy
h	Planck's constant (6.626×10^{-34} J·s)
HOMO	Highest occupied molecular orbital
I	Current
I_0	Reverse saturation current
I_L	Irradiance (power per unit area)
I_{ph}	Photocurrent
I_{SC}	Short-circuit current
ITO	Indium-tin oxide
J	Current density
J_0	Reverse saturation current density
J_{ph}	Photocurrent density
J_{SC}	Short-circuit current density
k	Boltzmann constant (8.617×10^{-5} eV/K)
LUMO	Lowest unoccupied molecular orbital
MEH-PPV	Poly[2-methoxy,5-(2'-ethyl-hexyloxy)-*p*-phenyl-ene vinylene]
n	Ideality factor
P	Power
P3HT	Poly(3-hexylthiophene)
$PC_{71}BM$	[6,6]-phenyl C_{71} butyric acid methyl ester
PCBM	[6,6]-phenyl C_{61} butyric acid methyl ester
PEDOT:PSS	Poly(3,4-ethylenedioxythiophene):poly(styrene sulfonate)
PTCBI	3,4,9,10-perylenetetracarboxylic-bis-benzimidazole
R_P	Parallel (or shunt) resistance
R_S	Series resistance
SnPc	Tin phthalocyanine
SubNc	Chloroboron subnaphthalocyanine
SubPc	Subphthalocyanine
T	Temperature
TiOPc	Titanyl phthalocyanine

V	Voltage
V_{if}	Electronic coupling matrix element
V_{OC}	Open-circuit voltage
WVTR	Water vapor transmission rate
ZnPc	Zinc phthalocyanine

SUMMARY

Organic solar cells have the potential to be portable power sources that are light-weight, flexible, and inexpensive. However, the highest power conversion efficiency for organic solar cells to date is ~8%, and most high-efficiency solar cells have an area of less than 1 cm^2. This thesis advances the field of organic solar cells by studying the physics and engineering of the devices to understand the reverse saturation current, which is related to efficiency, and the effects of area scaling.

The most commonly accepted models to describe the physics of organic photovoltaic devices are reviewed and applied to planar heterojunction solar cells based on pentacene / C_{60} as a model system. The equivalent circuit model developed for inorganic solar cells is shown to work well to describe the behavior of organic devices and parameterize their current-voltage characteristics with five parameters. Changes in the parameters with different material combinations or device structures are analyzed to better understand the operation of the presented organic solar cells. A one-dimensional diffusion model for the behavior of excitons and treatment of the organic layers as planes is demonstrated to adequately model the external quantum efficiency and photocurrent in pentacene / C_{60} solar cells.

The origin of the open-circuit voltage is studied using cells with different electrodes and different donor materials. While changing the electrodes does not affect open-circuit voltage, it is greatly modified by changes in the donor. Tests with additional semiconductors show the change in open-circuit voltage is not consistent from donor to donor as the acceptor is varied, suggesting a more complex relation than just the

difference in energy levels. Study of the temperature dependence of the equivalent circuit parameters shows that the reverse saturation current, which has a significant role in determining the open-circuit voltage, has a thermally activated behavior. From this behavior, the reverse saturation current is related back to charge transfer at the donor / acceptor heterojunction to suggest that both the effective energy barrier presented by the energy levels and the electronic coupling are important in determining the reverse saturation current and open-circuit voltage. This marks a shift from just considering a built-in voltage or the energy levels to also considering the electronic coupling of the donor and acceptor materials. Temperature-dependent performance characteristics are also used to show key differences between organic and inorganic devices.

Finally, the effect of area scaling is explored with pentacene / C_{60} solar cells having areas of 0.11, 7, and 36.4 cm^2. Analysis with the equivalent circuit model shows that performance decreases as area increases because of an increasing series resistance presented by the transparent electrode. A metal grid, to provide low resistance pathways for current, fabricated on top of the transparent electrode is proposed to reduce the effective resistance. The grid is unique in that it is placed between the electrode and the semiconductor layer and must be passivated to prevent shorts through the thin semiconductor to the back metal electrode. Analysis of the grid predicts greatly reduced series resistance, and experimental results show reduced resistance and improved performance for the 7 cm^2 and 36.4 cm^2 devices when including the grid.

CHAPTER 1

INTRODUCTION

1.1 Solar Cells

New power generation and storage equipment, ranging from batteries to power plants, must be continually developed and manufactured to meet the ever increasing demand for electrical power around the globe for a wide variety of applications. Solar cells have the ability to meet some of these power demands by directly converting sunlight into electricity and can potentially generate power anywhere there is light. Alexandre-Edmond Becquerel first observed the photovoltaic effect in an electrolyte solution in 1839 [1], and the modern era of solid-state solar cells was ushered in with developments at Bell Labs in 1954 [2]. Even with over 50 years of research, solar cells accounted for only about 1,636 GWh of the 18,307 TWh of electricity produced globally in 2005 according to the International Energy Agency [3]. Solar energy has great potential because the surface of the earth receives, on average, about 1.2×10^{17} W of solar power, so enough energy to supply global demand for an entire year is received from the sun in less than one hour [4]. While numerous solar cell technologies exist at this point, this dissertation will focus on the understanding and development of one of these technologies, organic solar cells.

1.2 Current Solar Cell Technologies

Many solar technologies exist with varying degrees of development, and organic solar cells are one of the newer classes of these technologies. This section will briefly discuss the main solar cell technologies at present to help put the role of organics in

context. The most commercially available solar cell technologies can be divided into two main groups: crystalline and multicrystalline silicon and inorganic thin films. After these two main groups, there are several emerging technologies that have not yet seen broad commercial availability but are still being heavily investigated in the laboratory for future application, including GaAs, concentrator, dye-sensitized, and organic thin-film solar cells.

1.2.1 Crystalline and multicrystalline silicon

Solar cells based on crystalline and multicrystalline silicon are by far the most developed and produced of all the solar cell technologies and currently account for ~80% of the solar cell market [5]. The development of silicon solar cells greatly benefited from the large-scale effort to understand and process silicon as a semiconductor for electronics and integrated circuits. In silicon solar cells, a photon is absorbed to generate a free hole and electron that are separated and collected to generate current [1]. Recombination of the carriers before collection, which leads to losses, can be reduced by using high-purity silicon and by applying processing techniques and device structures made possible by the deep understanding of the physics in silicon. Furthermore, the optical absorption spectrum of silicon is well matched to the solar spectrum for solar cells based on a single material [2]. While there are concerns about the supply of silicon wafers going into the future [6], the widespread availability of silicon from the integrate circuit industry has also contributed to the success of silicon solar cells. Power conversion efficiencies, which define the percent of incoming light power converted into electrical power, up to 25% and 20.4% have been demonstrated in crystalline and multicrystalline silicon solar cells, respectively [7].

While silicon is by far the leading solar cell technology, there are still many areas for improvement either with advances in silicon or with other material systems. First, high-purity silicon is generally expensive and slow to grow. Because silicon is an indirect band-gap semiconductor and has a weaker absorption compared to other semiconductors, thicker layers of silicon are generally required compared to other materials [2]. For these and other reasons, the silicon alone accounts for nearly 50% of the cost of a completed solar module [6]. To circumvent some of these limitations and potentially achieve lower costs per produced power, technologies are also being developed that can use less material either by having thinner active layers based on thin films or smaller active layers with light from a large area concentrated onto the small cell.

1.2.2 Inorganic thin film

Inorganic thin-film solar cells are the basis for nearly all of the presently available commercial solar cells that are not based on crystalline and multicrystalline silicon. Thin-film solar cells attempt to reduce the expensive cost of wafers in silicon cells by using thin films of semiconductors that are usually deposited onto a supporting substrate. The active layers are only a few microns thick but can still absorb significant amounts of light because of strong absorption in the materials. More impurities in the semiconductors can be tolerated since charges have a shorter distance to travel through the thin films [2]. Deposition and processing of thin-film materials also uses lower temperatures compared to silicon. Lower active material volume, purity, and processing temperatures can all lead to lower cost per area for thin-film solar cells, though it generally comes with a tradeoff of efficiency relative to crystalline and monocrystalline silicon. The net effect is a cost per Watt that is competitive with silicon. The leading material platforms for inorganic

thin-film cells are amorphous silicon (a-Si), $Cu(InGa)Se_2$ (CIGS), and CdTe with highest efficiencies of 10.1%, 19.4%, and 16.7%, respectively [7].

While the production of inorganic thin-film cells is rapidly growing, barriers still exist. Whereas silicon purification, wafer production, cell processing, and encapsulation have already developed as separate operations, all of these functions are often grouped into one facility for thin-film cells, leading to high capital costs [6]. The toxicity of cadmium itself is a major concern for CdTe solar cells, and the limited amount of indium reserves poses a long-term issue for CIGS, which requires the metal in the semiconductor [6]. Novel solutions to each of these challenges might be found with continued development.

1.2.3 Emerging technologies

Numerous other solar cell technologies exist that are still not widely available commercially. The highest efficiencies have been demonstrated in cells based on GaAs for both single and multijunction devices. Multijunction solar cells use multiple layers that are tailored to more efficiently convert different portions of the solar spectrum based on the band gap of the layers. However, GaAs solar cells have generally been limited to space applications because of their higher cost [2].

The high cost of high efficiency cells can potentially be offset by concentrating a large area of sunlight onto a solar cell with a small area. Concentration can produce a large amount of power with only a small amount of semiconductor. Furthermore, higher efficiencies can be obtained under concentrated light compared to the standard one sun illumination [8]. Efficiencies of 41.6% have been obtained in multijunction solar cells under concentrated sunlight [7]. However, concentrator systems are more complex

because of the additional hardware for focusing light, tracking of the sun, and cooling the cell.

Two other technologies that have been garnering significant attention are based on organic materials. Dye-sensitized solar cells use an organic dye coating a porous electrode with high surface area to absorb light. Efficiencies of up to 11% have been achieved for dye-sensitized solar cells [7]; however, the use of a liquid electrolyte in the cells is presently a source of reliability issues. Another organic technology is thin-film solar cells based on solid-state organic semiconductors. Organic semiconductors can have their chemical and electrical properties tailored in numerous ways by modifying the chemical structures and can allow for new processing methods. Organics have great potential for light-weight, flexible devices fabricated with high-throughput processes from low-cost materials in a variety of colors. However, organic semiconductors are still a relatively young field, and the highest efficiencies are only around 8% for the very best organic thin-film cells [7, 9].

1.2.4 State of the art

Figure 1.1 summarizes the highest efficiencies in various solar cell technologies obtained throughout the years. It should be noted that commercially available solar cells have, sometimes drastically, lower efficiencies compared to the records because of additional complexities when manufacturing cells on a large scale. While multijunction concentrators and GaAs cells have the highest record efficiencies, crystalline and multicrystalline silicon are still the market leaders. Even with their lower efficiencies, thin-film solar cells are making significant market penetration because of tradeoffs between efficiency and cost. However, it is clear that there are many different approaches

to reach the same goal of converting sunlight to electricity, and each technology may be able to fill an appropriate role based on its individual advantages and tradeoffs.

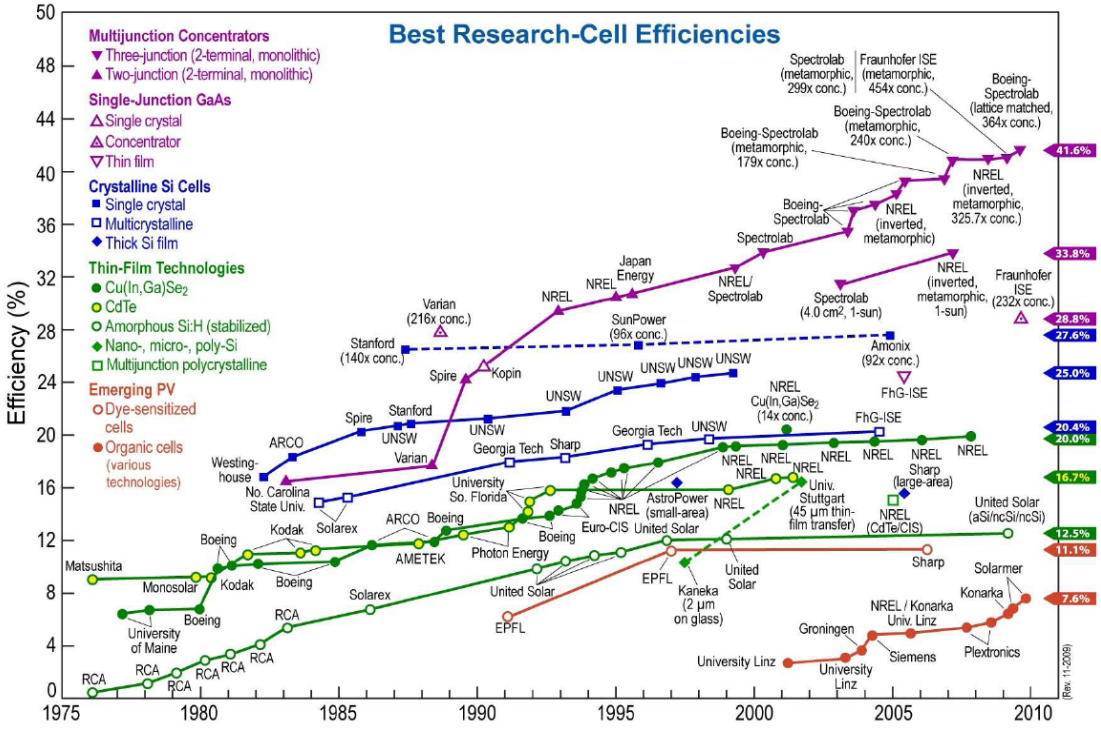

Figure 1.1. Timeline of highest efficiencies in various solar cell technologies. Reprinted from [8] with permission.

1.3 Solar Cell Basics

Having reviewed the main solar cell technologies, this section will cover the basic electrical characteristics common to all solar cells. When measured in the dark, the current-density vs. voltage (*J-V*) characteristics of most efficient inorganic and organic solar cells resemble the exponential response of a diode with high current in forward bias and small current in reverse bias. Shining light on a device generates a photocurrent in the cell in addition to the diode behavior, and the *J-V* characteristic under illumination is ideally the superposition of the dark characteristic and the photocurrent. The *J-V*

characteristics of an ideal device can be described by the Shockley equation with an additional photocurrent term, J_{ph}:

$$J = J_0\left[\exp\left(eV/nkT\right)-1\right]-J_{ph}, \tag{1.1}$$

where J is the current density, V is the applied voltage, J_0 is the reverse saturation current density of the diode, e is the elementary charge, n is the ideality factor, k is the Boltzmann constant, and T is temperature [10]. In reality, the photocurrent will have a dependence on applied voltage, and the illumination can affect the characteristics of the diode.

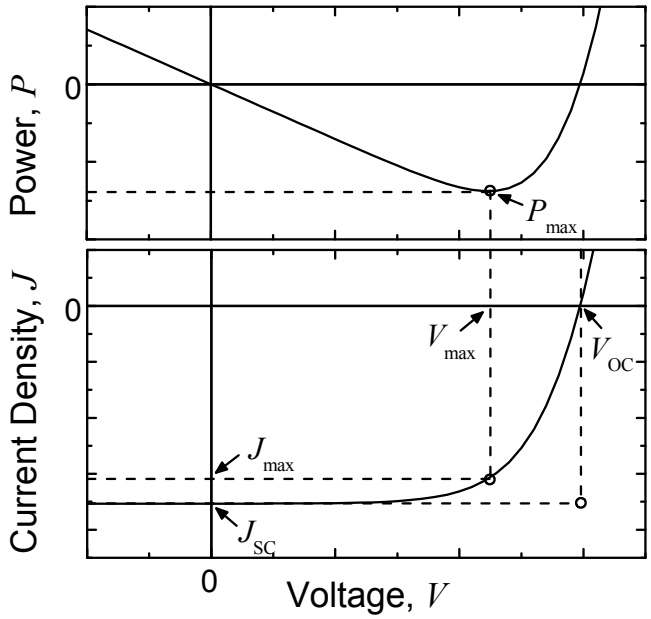

Figure 1.2. Graphs of power and current density as a function of voltage for a solar cell along with key parameters.

Figure 1.2 depicts the *J-V* plot for an idealized solar cell in the region of power generation. Power density, the product of voltage and current density, versus voltage is also plotted, and negative power indicates power generation. The most discussed

performance parameters that can be found from the *J-V* curve of a device under a known illumination source are open-circuit voltage (V_{OC}), short-circuit current density (J_{SC}), fill factor (FF), and power conversion efficiency (η).

1.3.1 Open-circuit voltage

The open-circuit voltage V_{OC} is the voltage across the solar cell when $J = 0$, which is the same as the device being open-circuited. Because $J = 0$ and power is the product of current and voltage, no power is actually produced at this voltage. However, the V_{OC} marks the boundary for voltages at which power can be produced. The open-circuit voltage can also be thought of as the point at which the photocurrent generation and dark current processes compensate one another.

1.3.2 Short-circuit current

Similar to V_{OC}, the short-circuit current density J_{SC} is the current density when $V = 0$, which is the same conditions as the two electrodes of the cell being short-circuited together. Again, there is no power produced at this point, but the J_{SC} does mark the onset of power generation. In ideal devices, the J_{SC} will be the same as the photocurrent density J_{ph}. However, it will be seen later that several effects can lower the J_{SC} from this ideal value (see Section 5.2.1). Although J_{SC} is technically a negative number with the conventions used here, discussions of different J_{SC} values will focus primarily on the magnitude of the value and treat it as a positive number, *e.g.*, a higher J_{SC} corresponds to a higher J_{ph}.

1.3.3 Fill-factor

While V_{OC} and J_{SC} mark the boundaries of power production in a solar cell, the maximum power density produced P_{max} occurs at the voltage V_{max} and current-density J_{max} where the product of J and V is at a minimum (or maximum in absolute value), as shown in Figure 1.2. Because of the diode behavior and additional resistance and recombination losses, $|J_{max}|$ and V_{max} are always less than $|J_{SC}|$ and V_{OC}, respectively. The fill factor FF describes these differences and is defined as

$$\mathrm{FF} = \frac{J_{max}V_{max}}{J_{SC}V_{OC}}. \tag{1.2}$$

FF is an indication of how close J_{max} and V_{max} come to the boundaries of power production of J_{SC} and V_{OC} and also and indication of the sharpness of the bend in the exponential J-V curve that connects J_{SC} and V_{OC}. Since higher FF is related to higher maximum power, high FF is desired; however, the diode-like behavior of solar cells results in FF always being less than one. Devices with high $|J_{SC}|$ and V_{OC} can still have low FF, suggesting that something must be done to improve device quality.

1.3.4 Power conversion efficiency

The most discussed performance parameter of a solar cell is the power conversion efficiency η and is defined as the percentage of incident irradiance I_L (light power per unit area) that is converted into output power. Because the point where the cell operates on the J-V curve changes depending on the load, the output power depends on the load. For consistency, the maximum output power is used for calculating efficiency. In equation form, efficiency is written

$$\eta = \frac{|J_{max}| \times V_{max}}{I_L} \times 100\% = \frac{\mathrm{FF} \times |J_{SC}| \times V_{OC}}{I_L} \times 100\%. \tag{1.3}$$

This form clearly shows that FF, J_{SC}, and V_{OC} all have direct effects on η. Furthermore, the area used to calculate J can affect η and should include inactive areas that are integral to the solar cell, such as grids and interconnects, when calculating efficiency for large area devices or modules.

Power conversion efficiency is important since it determines how effectively the space occupied by a solar cell is being used and how much area must be covered with solar cells to produce a given amount of power. Since larger areas require more resources to cover with solar cells, higher η is often desirable. However, there are tradeoffs between η and cost for each solar cell technology that must be balanced.

Power conversion efficiency is also very dependent on the power and spectrum of the light source since solar cells do not absorb and convert photons to electrons at all wavelengths with the same efficiency. To draw comparisons between various solar cells, a standard spectrum must be chosen for the calculation of η. Although the spectrum of the sunlight at the earth's surface varies with location, cloud coverage, and other factors, the AM1.5 G spectrum in Figure 1.3 is the most commonly used standard spectrum for measuring and comparing the performance of photovoltaics that are intended for outdoor use. Because of difficulties recreating this exact spectrum in the laboratory with standard lamps, power conversion efficiency measurements must often be corrected based on the external quantum efficiency.

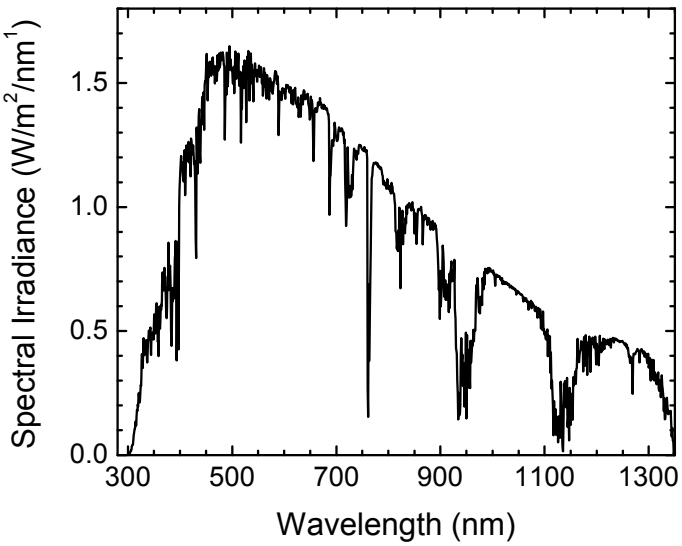

Figure 1.3. Spectral irradiance of the AM1.5 G solar spectrum up to 1,350 nm.

1.3.5 External quantum efficiency

The external quantum efficiency (EQE) of a device is the fraction of incident photons converted into current and depends on wavelength. One reason for the wavelength dependence is that the absorption in the active layers is a function of wavelength. Another reason, especially in inorganic solar cells, is that the location where a photon is absorbed in a device can also affect the probability of the resulting charges being collected or recombining and being lost.

The short-circuit current density expected under a light source can be estimated from the EQE and the spectral irradiance of the light source by integrating the product of the EQE and the photon flux density. For the standard AM1.5 G spectrum, the calculation is

$$J_{\mathrm{SC}} = \int_0^\infty eEQE(\lambda)\frac{\lambda}{hc}E_\lambda^{AM1.5G}(\lambda)\mathrm{d}\lambda, \tag{1.4}$$

where $E_{\lambda}^{AM1.5G}$ is the spectral irradiance of the AM1.5 G spectrum, λ is the wavelength, h is Planck's constant, c is the speed of light, and e is the elementary charge. If the EQE was measured at low light intensities, then this calculation will only be accurate if the short-circuit current density is a linear function of irradiance, as is expected for ideal devices. Otherwise, EQE must be measured with a dc bias light source that generates a photocurrent in the device similar to what is expected under AM1.5 G.

1.4 Organic Solar Cells

Thin-film solar cells based on organic semiconductors are interesting for several reasons. For one, the electrical and chemical properties of organic semiconductors can be tailored by modifying the chemical structure of the compounds in endless combinations. Though specific design rules are still under investigation, the potential for tailoring molecules to different applications is great. Furthermore, the organic molecules have the potential to be cheaply synthesized without significant concern on the limit of raw materials. Next, organic semiconductors can be deposited in a number of low-temperature and high-throughput ways, such as evaporation and solution processing, that can lower manufacturing costs. Because organic materials can have high absorption coefficients, a layer of only a few hundred nanometers is often enough to absorb a large fraction of light in the material's absorption spectrum. The use of such thin layers reduces the amount of active material needed and also makes light-weight and flexible devices possible. For these and other reasons, organic solar cells have gained significant attention.

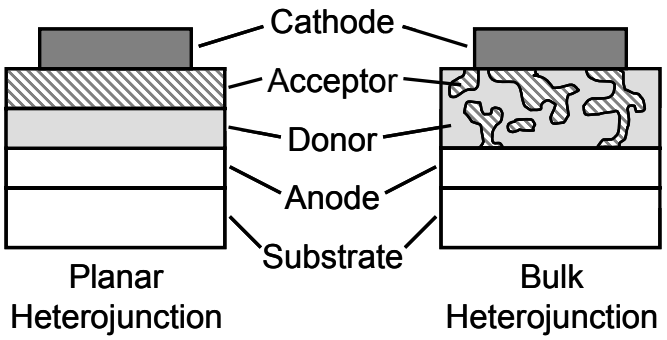

Figure 1.4. Schematics of the basic structures for solar cells based on a planar heterojunction and on a bulk heterojunction.

The first modern solid-state solar cell based on organic materials with an efficiency close to or higher than 1% was developed by C. W. Tang during his time at Eastman Kodak [11]. Tang stacked an organic material that donates electrons, or a donor, and an organic material that accepts electrons, or an acceptor, between the electrodes. When a photon is absorbed in an organic material, a bound electron-hole pair, called an exciton, is created and must be dissociated to contribute to the current. Stacking an acceptor material on top of a donor material (Figure 1.4), in this case 3,4,9,10-perylenetetracarboxylic-bis-benzimidazole (PTCBI) on copper phthalocyanine (CuPc), creates an interface that drives the dissociation of light-generated excitons and preferentially separates the electrons into the acceptor layer and the holes into the donor layer. This architecture yielded larger fill factors than those seen in previous single-layer devices [12] and *J-V* characteristics similar in shape to their high-efficiency inorganic counterparts. The architecture is commonly referred to as a planar heterojunction because the deposited layers can be idealized as stacked planes of different materials. Vacuum

thermal evaporation is the most common method of depositing the organic layers for these devices.

1.4.1 Planar heterojunctions

Advances were made using the planar-heterojunction structure with additional layers and new materials. Peumans *et al.* demonstrated that including a layer of bathocuproine (BCP) between the acceptor and metal cathode increased the power conversion efficiency in CuPc / PTCBI devices to 2.4% [13]. The BCP layer is thought to prevent the recombination of excitons at the interface between the organic layer and the metal and to prevent damage to the acceptor layer by the metal deposition. The next improvement came with the introduction of the fullerene C_{60} as the acceptor, resulting in power conversion efficiencies of 3.6% [14, 15]. The increase in efficiency is primarily attributed to a longer exciton diffusion length in C_{60} compared to PTCBI. The exciton diffusion length is the average distance that an exciton travels before recombining and is critical in planar-heterojunction devices because a photogenerated exciton must travel a distance to the donor / acceptor interface to be separated into a hole and electron. Short exciton diffusion lengths in most organic materials (on the order of tens of nanometers) limit the thickness of the organic layers. While thick layers are desired for high absorption, layers must also be sufficiently thin to prevent excessive recombination because of the short exciton diffusion lengths.

Other donor materials that have been demonstrated to work well in planar heterojunctions include pentacene [16, 17], tetracene [18], DCV5T [19], subphthalocyanine (SubPc) [20], chloroboron subnaphthalocyanine (SubNc) [20], and squaraine dyes [21] with efficiencies from 1.8% to 4.1% with C_{60} as donor. Researchers

have also begun experimenting with doping the layers to increase absorption, such as by doping CuPc with rubrene [22], and to improve carrier transport, such as by doping CuPc with pentacene [23]. Inserting an additional thin layer of zinc phthalocyanine (ZnPc) or CuPc between the donor and acceptor has been shown to increase the open-circuit voltage, but whether there is any trade-off in photocurrent when compared with the most efficient devices without the layer is still unclear [24, 25]. Donor layers of pentacene and a squaraine dye have also been processed from solution to make solar cells with vacuum-deposited acceptor layers with good success [21, 26].

1.4.2 Bulk heterojunctions

To overcome some of the limitations of the small exciton diffusion length, the donor and acceptor layers can be blended together to minimize the distance an exciton must travel to reach a donor / acceptor interface, as shown in Figure 1.4. This structure is called a bulk heterojunction since the heterojunction is dispersed throughout the bulk of the layer. However, morphology of these layers can be very important, as percolation pathways for the holes and electrons through donor and acceptor phases to the correct electrode are necessary. Hiramoto *et al.* first demonstrated the bulk-heterojunction structure with a co-deposited layer of metal-free phthalocyanine (as donor) and a perylene tetracarboxylic derivative (as acceptor) between neat layers of the donor and acceptor [27]. This structure led to higher photocurrent compared to devices without the mixed layer. Since then, bulk heterojunctions formed with other vacuum-deposited small molecules have also been demonstrated, primarily with CuPc and C_{60} or PTCBI [28, 29, 30, 31, 32].

Bulk heterojunctions also helped facilitate the transition to solution processing of the organic layers. Solution processing is attractive because it might be more easily applied to large-scale, high-speed manufacturing processes such as printing compared to vacuum processing. While a single layer of a semiconductor can easily be spin-coated from solution with the subsequent layers vacuum deposited [21, 26, 33], solution processing of both layers for a planar heterojunction is challenging because the deposition of the second layer must not dissolve and remove the first layer. Application of bulk heterojunctions would simplify solution processing by depositing a single layer that is a blend of donor and acceptor. The main challenge would be creating percolation pathways for the holes and electrons to be efficiently transported to and collected at the electrodes.

The first solution-processed organic solar cells incorporating a blend for the active layer were demonstrated by blending the polymers MEH-PPV and cyano-PPV (CN-PPV) as donor and acceptor and reached external quantum efficiencies up to 6% [34, 35]. The natural phase segregation of polymer blends was expected to create pathways to enhance carrier transport [34], and the work functions of the electrodes are thought to determine the extracted carrier type [35]. Yu *et al.* showed that the acceptor polymer could be replaced with a soluble derivative of C_{60}, [6,6]-phenyl C_{61} butyric acid methyl ester (PCBM), to yield devices with power conversion efficiencies up to ~1.5% under low-intensity broadband illumination [36]. The combination of polymer and small molecule has become the most common approach to solution-processed bulk heterojunctions.

Much effort has been spent exploring new polymers and acceptors for bulk-heterojunction solar cells to increase absorption and carrier transport. One of the most researched combinations to date is regioregular poly(3-hexylthiophene) (P3HT) blended with PCBM, which reaches power conversion efficiencies close to 5% [37, 38]. Recently, new polymers (PCPDTBT, PTB1, and PCDTBT) with absorption spectra that extend farther into the red part of the spectrum have been reported in blends with $PC_{71}BM$ yielding efficiencies greater than 5% [39, 40, 41]. The phase segregation in the films has become apparent as a major factor influencing overall device efficiency. Annealing of devices [37, 38], changing the solvent and the drying speed of the film [38], and adding chemicals with selective solubility of the fullerene component to affect crystallization [39, 42, 43, 44, 45] have been found to affect the phase segregation and improve performance. However, finding the optimum conditions can be very tedious and time consuming. Solution-processed cells based on blends of small molecules are now starting to be reported with efficiencies above 3% [21, 46]. Researchers are taking advantage of the ability to solution process by demonstrating cells fabricated by screen printing [47], inkjet printing [48], gravure printing [49], brush painting [50], and even roll-to-roll printing [51].

1.4.3 Tandem solar cells

Tandem solar cells provide one way of increasing the overall absorption and efficiency of a solar cell. A tandem cell is essentially two (or more) solar cells stacked directly on top of each other with a transparent electrode (recombination layer) in the middle. Light will travel through the front cell, past the transparent electrode, and into the back cell. Ideally, a tandem cell will behave like two cells in series. Therefore, the

voltages produced by the two cells will add, and the current of the tandem cell will be limited by the lower current of the two cells. If the same material is used for the front and back cell, a tandem configuration can allow for an overall thicker cell to absorb more light, though the layers must be carefully designed to ensure similar photocurrent in both cells. Alternatively, materials with complementary absorption spectra can be used in the two cells to cover a broader portion of the solar spectrum, which may also reduce energy lost if photons are absorbed in materials with a band gap closer the energy of the photons.

Hiramoto *et al.* reported the first organic, tandem solar cell using a thin layer of Au between two bilayer cells of metal-free phthalocyanine and a perylene tetracarboxylic derivative (Me-PTC) deposited by thermal evaporation [52]. Although the tandem cell had a reduced photocurrent compared to a single cell because of reduced light intensity and photocurrent in the back cell, inclusion of a gold layer with an effective thickness of 0.6 nm was sufficient as a recombination site connecting the two cells and led to a doubling of V_{OC}. Cells without the Au layer did not show an increase in V_{OC}. By adding additional layers to optimize optical interference effects, with the front cell tuned to long wavelengths and the back cell to short wavelengths, and using CuPc / C_{60} as the absorbing layer, vacuum-deposited tandem cells up to 5.7% have been demonstrated [53].

Stacked structures have been reported using vacuum deposition with CuPc / PTCBI [54], ZnPc / C_{60} [55, 56, 57], SnPc / C_{70} [58, 59], and pentacene / C_{60} [60] heterojunctions. The connecting layer is usually Ag or Au [61] often surrounded by thin metal oxide [20, 62] or doped organic layers [53], but doped organic layers without a metal have also been demonstrated [57]. The first reported tandem cells employing materials with different absorption spectra contained three heterojunctions with CuPc as

the donor and perylene derivatives with different absorption spectra as the acceptors, but overall efficiency was still below 1.5% because of low fill factor and poor photocurrent matching in the junctions [63]. More recently, 5.1% has been achieved in tandem cells with SubNc and SubPc as the donors [20], and Heliatek has reported an efficiency of 8.3% in tandem cells made from small molecules with undisclosed structures [9].

When tandem devices incorporate active materials deposited with solution processing, the steps must be carefully chosen to prevent the solution processes from damaging previously deposited layers. One way to ensure compatibility between steps is by depositing the first cell with solution processes and the second cell with vacuum deposition. Using this structure, cells of ZnPc / C_{60} and CuPc / C_{60} vacuum deposited on top of spin-coated P3HT / PCBM cells have been demonstrated with higher V_{OC}, but there is not an improvement in efficiency compared to a single, optimized P3HT / PCBM cell [64, 65, 66].

To prevent the second cell from damaging the first when both cells are processed from solution, a material that is insoluble in the solvent of the second cell is usually placed between the two cells by either physical vapor deposition or solution processing. Insoluble layers deposited by physical vapor deposition include sputtered indium-tin oxide (ITO) [67, 68] and thermally evaporated Au [69, 70] or Al [71]. Solution processed spacer layers of ZnO nanoparticles in acetone [72, 73] and TiO_X from a precursor in isopropanol [74] have been demonstrated. The most efficient published solution-processed tandem cell to date reaches an efficiency of 6.5% and consists of a front cell of the low-band-gap polymer PCPDTBT and PCBM, a back cell of P3HT and $PC_{71}BM$, and an internal electrode of TiO_X and PEDOT [74]. However, most organic, tandem solar

cells to date have a lower efficiency than single-heterojunction cells with optimized geometries because of difficulties matching the photocurrent of the series-connected cells. Much research is still needed to take full advantage of the larger absorption of the solar spectrum in tandem cells and increase the overall efficiency.

1.4.4 State of the art

Considering only published single-heterojunction devices, the highest AM1.5 G efficiency reported to date for vacuum-deposited organic solar cells is 3.6% for CuPc / C_{60} / BCP devices [14]. For a planar heterojunction with a spin-coated donor layer, 4.1% has been reported for a squaraine dye / C_{60} / BCP device [21]. Vacuum-deposited bulk-heterojunction devices using a mixed layer of CuPc and C_{60} deposited by thermal evaporation with the assistance of a carrier gas have been reported with efficiencies up to 4.4% [75]. The best AM1.5 G efficiency reported for solution-processed devices with a polymer is 6.1% for a blend of PCDTBT and $PC_{71}BM$ [41]. Small-molecule solution-processed devices have now reached efficiencies of 4.4% with blends of $DPP(TBFu)_2$ and $PC_{71}BM$ [46]. Table 1.1 summarizes the key performance parameters for all of these state-of-the-art devices.

Higher efficiencies that have been certified by a recognized laboratory have been reported, but details of the materials and structures are unpublished because they are proprietary to the companies that developed them. The highest efficiency to date is 8.1% in single-junction polymer solar cell achieved by the company Solarmer. However, these devices are presumed to have an area less than 1 cm^2. The highest confirmed efficiency for a single junction with an area larger than 1 cm^2 is 5.1% based on proprietary polymers developed by Konarka [7].

For organic, tandem solar cells, the highest AM1.5 G efficiencies published for vacuum-deposited, small-molecule devices and solution-processed devices are 5.7% and 6.5%, respectively [53, 74]. Again, both of these devices are very small with active areas less than 0.06 cm^2. The small-molecule solar cell had mixed layers of CuPc:C_{60} between neat layers of CuPc and C_{60} as the active layers in both cells, PTCBI and BCP as the exciton blocking layers in the front and back cells, respectively, and Ag nanoclusters buried in a layer of m-MTDATA doped with F4-TCNQ as the connecting layer [53]. The solution-processed cell used a front cell of PCPDTBT and PCBM, a back cell of P3HT and $PC_{71}BM$, and an internal electrode of TiO_X and PEDOT [74]. The highest certified efficiency for an organic, tandem solar cell is now 8.3% as reported by Heliatek for a vacuum-processed small-molecule device with an area of 1.1 cm^2; however, few details are known about the device [9].

Table 1.1. List of organic solar cells with the highest reported efficiencies.

Junctions	Active Materials	J_{SC} (mA/cm^2)	V_{OC} (mV)	FF	η (%)	Area (cm^2)
1	CuPc / C_{60} / BCP [14]	12	530	0.52	3.6	0.0079
	Squaraine dye / C_{60} / BCP [21]	8.9	790	0.54	4.1	0.0079
	Mixed CuPc:C_{60} [75]	17	460	0.56	4.4	0.0079
	PCDTBT:$PC_{71}BM$ [41]	10.6	880	0.66	6.1	0.127
	Proprietary (Solarmer) [7]	14.7	756	0.709	7.9	0.0441
	Proprietary (Solarmer) [76]	-	-	-	8.1	-
	Proprietary (Konarka) [7]	9.39	876	0.625	5.15	1.021
2	CuPc / C_{60} and CuPc / C_{60} [53]	9.7	1030	0.59	5.7	0.007 – 0.06
	PCPDTBT:PCBM and P3HT:$PCB_{71}M$ [74]	7.8	1240	0.67	6.5	0.045
	Proprietary (Heliatek) [7]	6.18	1589	0.619	6.1	1.989
	Proprietary (Heliatek) [9]	-	-	-	8.3	1.1

1.4.5 Challenges

While the primary factor preventing the commercial application of organic solar cells is their limited efficiency, other major challenges that must be addressed include stability and scaling. The oxygen and water present in ambient air are known to degrade the performance of most organic solar cells [77, 78, 79, 80]. Therefore, either structures that are insensitive to air must be developed or organic cells must be encapsulated to protect them from the ambient atmosphere. For example, structures that remove the low work function electrode from the top layer of the device are being developed to help improve air stability [81, 82]. However, developing completely air stable molecules is a big challenge, so encapsulation methods are still needed.

To take full advantage of the potential for lightweight and flexible organic solar cells, encapsulation technologies that are also lightweight, thin, and flexible must be developed. The encapsulation must also be processed at temperatures that are compatible with the organic materials and flexible substrates. It has been suggested that water vapor transmission rates and oxygen transmission rates on the order of $10^{-4} – 10^{-6}$ g m^{-2} day^{-1} and $10^{-3} – 10^{-5}$ cm^3 m^{-2} day^{-1} atm^{-1}, respectively, are necessary to maintain long shelf lifetime in organic solar cells [83]. Currently, the most promising candidates for encapsulation are alternating thin films of inorganic and organic materials. The inorganic layers serve as the primary barrier to water and oxygen, while the organic layers serve to interrupt defects that would propagate though a single, continuous inorganic film [84].

Thin-film encapsulation by deposition of a single layer on top of the devices has been demonstrated with Al_2O_3 [85], SiN_X [86], and a SiO_2-silicone hybrid [87] for organic light-emitting diodes (OLED's). To reduce the impact of defects generally found in a single film, encapsulation consisting of two or three layers has been tested using

SiN_X / AlO_X [88], parylene / AlO_X [79, 89, 90], and parylene / SiN_X / AlO_X [89], and multilayer films with four to five repetitions of polyacrylate / Al_2O_3 have been used [91]. Thin-film encapsulation layers on top of organic solar cells are now starting to be demonstrated with layers such as Al_2O_3 [80], Al_2O_3 / parylene [79], SiO_X / Al_2O_3 / parylene [92], and Al_2O_3 / Hf_2O [93] yielding significantly improved lifetimes. Instead of directly coating the devices, barrier coatings on plastic substrates between which devices can be sealed are also under development [94, 95].

The issues that arise when scaling up to large-area devices must also be addressed. Presently, many of the high-efficiency devices that are reported in the literature have active areas of 1 cm^2 or less. The large-area devices that have been reported are usually modules consisting of several smaller cells with overall efficiencies less than half that of a single, optimized, small-area cell [83, 96, 97, 98, 99]. The main problem with increasing cell size stems from the use of a transparent electrode with a relatively high sheet resistance, as is discussed in detail in Section 5.2. The low conductivity of the transparent electrodes results in low fill factor and short-circuit current in large-area devices; therefore, overall efficiency is expected to decrease as device area is increased. Strategies must be developed to deal with these losses as area increases. While significant progress has been made in the field of organic solar cells, it is clear that many challenges still remain.

1.5 Goals and Structure of the Dissertation

Organic solar cells have seen significant improvement in the last two decades, but more progress in several areas must still be made before they are ready for commercial applications. These challenges include increasing efficiency, improving stability,

developing encapsulation, increasing area, and improving device reproducibility. Fundamental to solving many of these challenges is a better understanding of all the physical process occurring in organic solar cells. As organic semiconductors are still a relatively new field, the framework for explaining the physics of device operation is still not nearly as well developed as for inorganic solar cells and many questions remain. The primary goals of this thesis are to study the physics of organic solar cells with a focus on the origin on the open-circuit voltage and to develop and demonstrate strategies for improving the performance of large-area cells.

The research in this thesis can be divided into three main sections. First, the current state of understanding on the physics of organic solar cells is discussed in Chapter 3. Pentacene / C_{60} solar cells are used as a model system to explore and demonstrate how well the various models that are currently available to explain the *J-V* characteristics, short-circuit current, and open-circuit voltage agree with experimental results. Each of these is fundamentally important to determining the performance of organic solar cells. While good agreement can be found in the case of model characteristics and short-circuit current, it is shown that there is still confusion as to what ultimately determines open-circuit voltage in the devices.

The next section of the thesis (Chapter 4) investigates the origin of the open-circuit voltage by studying a combination of donor and acceptor materials with different properties. An equivalent circuit model is used to help understand the change in device performance with varying active layers. In particular, how the reverse-saturation current is affected is studied and connections are made with the properties of the active layers and molecular interactions. Furthermore, comparisons are made between the behavior of

organic solar cells at different temperatures and inorganic solar cells to begin to evaluate the overlap in physical processes in the different devices.

Finally, the more applications-oriented problem of reduced device performance with increased area is studied in Chapter 5. While understanding of physics is important to fundamentally improving organic solar cells, engineering approaches to minimize performance loss as cell area increases are also important as cell area will eventually be increased for practical applications. After studying the influence of area scaling on cell performance, a metal grid is used to improve performance by minimizing the resistance of the transparent electrode. Implementation of the grid presents unique challenges because the limiting electrode is sandwiched between the substrate and the active layer. The following chapter summarizes all of the experimental methods used in performing these studies.

CHAPTER 2

EXPERIMENTAL METHODS

2.1 Introduction

For convenience, all of the experimental procedures used to perform the studies in this thesis are compiled in this chapter. While specifics of the device geometries, such as thicknesses, are listed in the text when a new device is presented, all of the steps for device fabrication and measurement, including processing conditions, are summarized here.

2.2 Fabrication

Devices fabrication consists of three main steps. First, the organic semiconductors must be purified to obtain high performance. Second, the substrates for the devices are cut to size, cleaned, and optionally modified with different processes to affect how the deposited organic layers will interact with the substrate. Finally, the organic layers and back contact are deposited. In these experiments, all of the active organic layers were deposited by heating and subliming the compounds under vacuum. The following sections describe the steps used in this research to fabricate devices with reproducible results.

2.2.1 Material purification

Prior to the fabrication of any device, the organic semiconductors are first purified to remove impurities that can contaminate the semiconductor layer and the vacuum deposition system. Several reports have shown that J_{SC}, V_{OC}, and η can all be improved by first purifying commercially received materials before deposition [100, 101]. For

organic small molecules that can be sublimed at high vacuum, gradient sublimation is the most common method for purification [102] and does not require any solution processing of the compounds. On the other hand, polymers can be more difficult to purify and require different techniques depending on the nature of the polymer. All the organic compounds used for the active layers here are small molecules that can be sublimed, so gradient sublimation was used for purification.

The basic process of gradient sublimation is to load the source material into the closed end of a process tube lined with inner tubes (see Figure 2.1). The process tube is then placed into a furnace and pumped down to high vacuum using a dry pump. Next, the furnace zone encompassing the source material is gradually heated until the source begins to sublime. Crystals of the purified material deposit on the warm walls of the inner tubes in the middle portion of the process tube. Volatile impurities travel to the pump end of the tubing, while nonvolatile impurities remain at the source end. The purified material can then be extracted from the walls of the inner tubes.

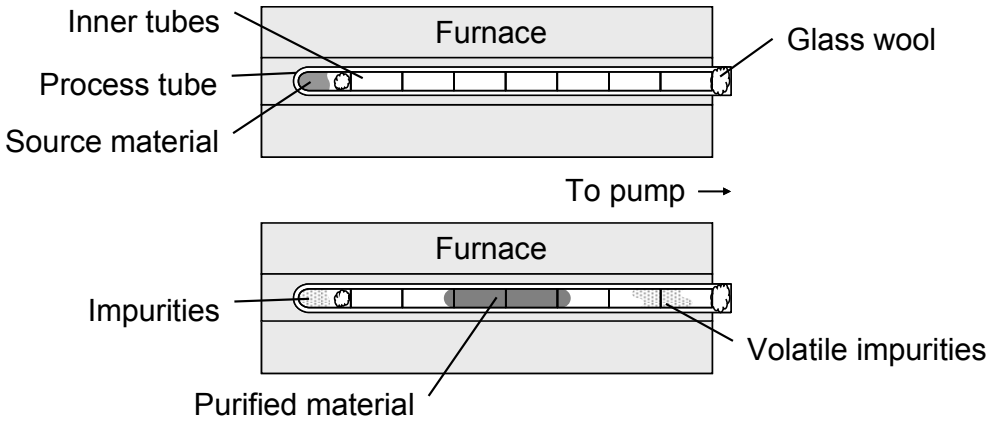

Figure 2.1. Schematics of the gradient sublimation system before (top) and after (bottom) purification of a small molecule.

The complete process used for preparing the system and purifying the organic semiconductors is as follows. First, the process tube (1.125” outer diameter × 36”) was rinsed with acetone, blown dry with nitrogen, rinsed with isopropanol, and again blown dry. The process tube was then evacuated to high vacuum using the turbomolecular pump and annealed at 500 °C overnight. After cooling, the process tube could be removed from the vacuum pump.

A set of inner tubes (0.875” outer diameter × 3”) were next thoroughly cleaned in a piranha solution. A set consists of one inner tube with a closed end to hold the source material and 10 inner tubes with both ends open to line the process tube. Enough sulfuric acid to submerge all of the inner tubes was heated to 120 °C in a crystallizing dish on a hot plate in a fume hood. After carefully placing the inner tubes in the heated acid, enough H_2O_2 was added (~10 ml) to the solution to begin the cleaning reaction, as evidenced by bubbling. After letting the inner tubes soak for about one hour, the solution was allowed to cool to room temperature. The inner tubes were then rinsed with copious amounts of deionized water and blown dry with nitrogen. The inner tubes were baked overnight in a vacuum oven at 100 °C. Finally, the inner tubes were loaded into a cleaned and baked process tube, evacuated to high vacuum, and baked at 500 °C overnight.

After cooling and removing the inner tubes, the organic source material was loaded into the first inner tube, which has a sealed end. Table 2.1 lists the organic materials and vendors used. A piece of glass wool was used to prevent material from spilling out of the tube and contaminating the other zones of the system. While the solid material cannot pass through the glass wool, the sublimed material can easily pass. After loading all of the inner tubes into the process tube, an additional piece of glass wool was

used to help keep the inner tubes in place and to prevent volatile impurities from getting into the pump. The process tube was then pumped to high vacuum (< 10^{-5} Torr).

Table 2.1. List of organic semiconductors used in the experiments, their vendors, and the sublimation temperature used for purification.

Semiconductor	Vendor	Sublimation Temperature (°C)
Pentacene	Sigma Aldrich	275
Tetracene	TCI America	200
CuPc	Stern Chemicals	475
TiOPc	Sigma Aldrich	500
C_{60}	Alfa Aesar	540
C_{70}	Nano-C	580
PTCBI	H.W. Sands Corp.	425
BCP	TCI America	240

The furnace zone in which the source material is located was then gradually heated to the sublimation temperature (see Table 2.1), making sure to slow the rate of heating if the pressure levels began to rise. Although the furnace consists of three heating zones, only the zone containing the source material is heated to create a gradient across the processing tube and because the furnace is insulated well enough that the other zones do also increase in temperature, though lower than the source zone. When subliming materials for which the sublimation temperature was not previously known, the procedure was to increase the temperature in increments of ~25 °C and wait several hours to see if any sublimed material could be visually detected. This gradual temperature increasing and monitoring was continued until a steady rate of sublimation was found.

Once most of the source material had sublimed, the furnace and tubes were cooled. After removing from vacuum, the inner tubes were carefully slid out of the process tube.

The purified material was then collected from the middle inner tubes by scraping the material off the walls with a clean spatula. The collected material was then immediately loaded into a nitrogen-filled glovebox for storage until use in the vacuum deposition system.

2.2.2 Substrate preparation

Preparation of the substrates is extremely important for obtaining reproducible results. All of the solar cells presented in this research used glass coated with the transparent conductor ITO as the substrate upon which the active layers and back electrode were grown. Because the illumination enters the cell through the glass of the substrate, the geometry is considered a superstrate configuration. After cutting the ITO-coated glass to the appropriate size, the ITO was etched to define the transparent electrode. The ITO glass was then thoroughly cleaned to prepare it for subsequent surface modification, if applicable, and the deposition of organic layers. Each of these processes is explained in more detail below.

All of the ITO-coated glass used in this research was obtained from Colorado Concept Coatings LLC. The glass is a polished soda lime float glass with a thin coating of SiO_2 followed by the ITO with a sheet resistivity of ≤ 15 Ω/sq. (part #96041). Because the ITO-coated glass comes in 14" × 14" × 0.043" sheets, the glass had to be cut to the size needed for devices. A 1" perimeter around the edge of the ITO-coated glass was always cut off and discarded since there were non-uniformities in the ITO layer that could be visually observed. For all the devices except the large-area solar cells (see Section 2.2.4), the ITO-coated glass was first cut into 1" strips by placing the ITO side on a soft cleanroom wipe, scoring with a glass cutting, and breaking along the score.

Next, the 1” strips were masked off for the etching process by applying a 0.5”-wide strip of Kapton tape on one half of the ITO coating along the entire length of the glass strip. The glass side was then scored, and the glass was broke into 1” × 1” samples with the Kapton tape serving to protect the ITO that would be used for the transparent electrode. Before breaking the glass along the score, a razorblade was used to cut the Kapton tape along the score line, which was on the opposite side.

For etching, the substrates were loaded into a sample holder and suspended in a plastic container on a wire grating. Approximately 30 ml of magnesium turnings were dropped through the grating to the bottom of the container, followed by 40 ml of HCl. The container was covered, and the vapor produced from the chemical reaction etched the exposed ITO. After 105 seconds, the substrates were removed from the vapor etch and rinsed with water. The Kapton tape was removed to reveal the remaining ITO electrode.

Finally, the substrates were thoroughly cleaned in four ultrasonic baths, each lasting 20 minutes. The first bath was of deionized (DI) water and detergent (Liquinox) followed by rinsing under a stream of DI water. Next, baths of DI water, acetone, and isopropanol were used. After each of these baths, the substrates were blown dry with nitrogen before proceeding. The cleaned substrates were loaded into the glovebox for storage. In the cases when substrates were not used immediately after the full cleaning, they were removed from the glovebox, cleaned in an ultrasonic bath of isopropanol for 20 minutes, and blown dry with nitrogen immediately prior to use.

2.2.3 Surface treatment

Two types of surface treatments were used to modify the work function of the ITO used in some of the solar cells: air plasma and a self-assembled monolayer of

phosphonic acid. Air plasma treatment was performed for 3 minutes on cleaned ITO substrates using a plasma etching system (Plasma-Preen II, Plasmatic Systems, Inc.). Following plasma treatment, the substrates were immediately loaded into a nitrogen-filled glovebox.

The self-assembled monolayer treatment with phosphonic acid was done in a nitrogen-filled glovebox. The phosphonic acid, pentafluorobenzyl phosphonic acid (F5BPA), was synthesized by and obtained from Peter Hotchkiss in the research group of Prof. Seth Marder in the School of Chemistry and Biochemistry at the Georgia Institute of Technology. Treatment solutions were made in a mixture of chloroform ($CHCl_3$) and ethanol (C_2H_5OH) in a ratio of $CHCl_3$:C_2H_5OH::2:1. The phosphonic acid was dissolved in the mixture for concentrations of 1 mM, and the solutions were stirred overnight. Cleaned ITO substrates were then dipped into petri-dishes containing the filtered mixtures (0.2 μm PTFE filters) for 30 minutes. The substrates were removed from the mixture and baked on a hot plate at 120 °C for 1 hour. After cooling, the substrates were thoroughly rinsed with a $CHCl_3$:C_2H_5OH (2:1) solution. The rinsed substrates were again baked on the hot plate at 120 °C, and the hotplate and substrates were then allowed to cool to room temperature.

Additionally, a thin layer of poly(3,4-ethylenedioxythiophene):poly(styrene sulfonate) (PEDOT:PSS) was spin-coated onto the ITO before deposition of tetracene for all of the devices with tetracene as the donor. PEDOT:PSS is a hole-transport layer and was needed to improve film growth. After treating cleaned ITO with air plasma for 3 minutes, PEDOT:PSS (Clevios P VP AI 4083, H.C. Starck) was filtered (0.45 μm PVDF filter) and spin coated on the ITO in air at 5000 rpm for 1 minute. Finally, the ITO coated

with PEDOT:PSS was annealed on a hot plate for 10 minutes at 140 °C before loading into a glovebox.

2.2.4 Grid fabrication

Large-area devices with and without a metal grid were also fabricated as part of this research (see Chapter 5). Figure 2.2 depicts a cross-sectional view of the steps used to fabricate the metal grid. First, a seed layer was deposited on top of ITO-coated glass. Photoresist was then spin-coated and patterned using standard photolithography techniques to define mold structures for growth of the copper grid by electroplating. After electroplating and removing the photoresist, an additional photoresist layer was spin-coated and patterned to passivate the exposed copper that is not in contact with the seed layer / ITO. Finally, the excess seed layer was removed by etching to expose the ITO for subsequent deposition of the organic layers and back electrode on top of the grid / ITO structure. Detailed steps for the grid fabrication follow.

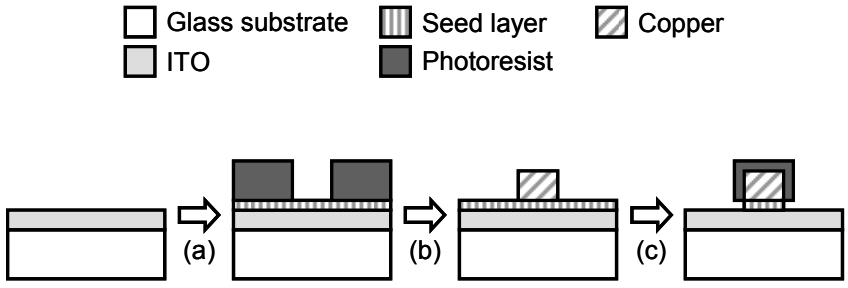

Figure 2.2. Process sequence for fabrication of the metal grid: (a) seed layer deposition on top of patterned ITO followed by deposition and patterning of photoresist to create mold structures; (b) electroplating of copper electrode and mold structure removal; (c) deposition and patterning of photoresist passivation layer and removal of excess seed layer.

ITO-coated glass (≤ 15 Ω/sq., Colorado Concept Coatings LLC) was cut into 3.5" × 3.5" substrates, and the ITO was patterned using photolithography and wet chemical etching. The area to be etched was defined by spin-coating a photoresist layer (SPR220, Shipley), heating at 100 °C for 20 minutes, exposing to UV light through a mask, and immersing in a developer (MF319) for 1 minute to remove the unwanted areas. The exposed ITO areas were etched in a solution of $HCl:HNO_3$:DI water in a ratio of 3:4:1 at room temperature for 10 minutes and then rinsed with DI water. After submerging the substrate in a 60 °C bath of photoresist remover (Remover 1165, Shipley) for 10 minutes to remove the photoresist, the ITO was then cleaned in sequential ultrasonic baths of DI water with detergent, acetone, and isopropanol for 60 minutes each.

To begin the grid fabrication, seed layers consisting of 20 nm of chromium and 200 nm of copper were deposited over the entire ITO surface using a filament evaporator. Electroplating mold structures were created with a thick photoresist (Shipley SPR220). The photoresist was patterned using similar steps as for the ITO etching but with a mask to define the grid shape.

Copper plating solution was prepared by mixing 250 mg $CuSO_4 \cdot 5H_2O$ and 25 ml H_2SO_4 in 1 liter of deionized water, following the procedures in [103]. A copper layer of 5 μm was electroplated by applying a dc current density of 10 mA/cm^2 between the ITO / seed layer as cathode and a copper plate as anode, both submerged in the plating solution. The substrate was rotated in the plating solution every 50 seconds to make the electroplated copper layer more uniform. The molding structures were removed by dipping, for 10 minutes, the substrate in a photoresist remover (Shipley Microposit Remover 1165) heated to 80 °C.

Next, photoresist (NR9-8000P, Futurex) was used to form a passivation layer on top of electroplated grid by spin-coating, exposing to UV light through an aligned shadow mask, and developing the resist. The chromium and copper seed layers were removed by wet chemical etching in H_2O_2:H_2SO_4:DI water (1:2:7) and HCl:DI water (1:1). Although the seed layer acts to protect the ITO surface throughout the processing, devices made directly on the ITO showed blocking characteristics. To improve the ITO / organic contact, the ITO surface was treated with oxygen plasma. Next, the substrates were treated with phosphoric acid by dipping in 20% H_3PO_4 for 10 minutes. Finally, the substrates were rinsed with deionized water, dried on a hotplate, and transferred into a glovebox for subsequent deposition of the active organic layers.

2.2.5 Evaporation

The active organic layers and back metal electrode were all deposited using a vacuum thermal evaporation system (SPECTROS, Kurt J. Lesker). In vacuum thermal evaporation, substrates are loaded into a deposition chamber that is pumped down to high vacuum. Organic or metal source material inside the chamber is heated in a crucible until the source sublimes or evaporates, thus coating the surfaces exposed to the stream of evaporated material. Deposition rate and thickness is usually monitored with quartz crystal microbalances and can be adjusted by changing the power applied to the source heaters. Shadow masks close to the substrates can be used to define patterns for the deposited layers.

The SPECTROS system used here has four low-temperature sources for organics and two high-current sources for metals. Donor and acceptor materials were loaded and evaporated in the same chamber from separate sources. When changing sources, the

source shields were cleaned with solvents and the source baked at high temperature with an empty crucible before loading the new material to minimize contamination. Up to three shadow masks can be loaded and swapped in the system without having to break vacuum. One shadow mask was used for defining the metal electrodes, one mask for the organic layers, and a third mask was optionally used for thickness variations of one of the organic layers. With the configuration of four organic sources, two metal sources, and three masks, the organic layers and back metal contact could be deposited without breaking vacuum after the substrates were loaded. Substrate rotation was also used to improve the uniformity of the deposited layers.

After preparation, substrates were loaded into the SPECTROS system for deposition. Because the system is connected to a nitrogen glovebox, substrates were directly loaded from and unloaded into a nitrogen atmosphere to prevent degradation from ambient atmosphere. All depositions were performed at a base pressure of less than 2×10^{-7} Torr, as high pressure has been observed to be detrimental to device performance. Thicknesses and rates were measured with quartz crystal microbalances that were calibrated with thicknesses measured with a profilometer (Dektak 6M, Veeco) on films deposited in prior depositions. Thicknesses are noted for the individual devices in the text, but the deposition rates were consistent for individual materials and were as follows: pentacene (0.5 Å/s), CuPc (1 Å/s), tetracene (0.2 Å/s), TiOPc (1 Å/s), C_{60} (1 Å/s), C_{70} (0.5 Å/s), PTCBI (1 Å/s), BCP (0.5 Å/s), and Al (1-2 Å/s). Following deposition, devices were unloaded and stored in the nitrogen glovebox until testing.

2.3 Characterization

2.3.1 External quantum efficiency

EQE measurements were made by measuring the short-circuit current density under monochromatic light for the test device and a reference calibrated photodiode (S2386-44K, Hamatsu) and calculating the EQE from

$$EQE_{\text{test}} = EQE_{\text{ref}} \frac{J_{\text{test}}}{J_{\text{ref}}}, \tag{2.1}$$

where the subscripts "test" and "ref" refer to the test and reference devices, respectively. The monochromatic light was supplied by a xenon lamp (ASB-XE-175EX, CVI Spectral Products) coupled to a monochromator (CM110, CVI Spectral Products). The light from the monochromator was passed through a filter with a cut-on at 400 nm, to eliminate second-order effects, and a diffuser, to spread the light over the entire device. The current density was measured using a Keithley 2400 sourcemeter in a four-wire scheme controlled by a LabView program. All measurements were made in a nitrogen glovebox.

2.3.2 Current-voltage characteristics

J-V characteristics for all of the devices were measured in a nitrogen-filled glovebox using a Keithley 2400 sourcemeter controlled by a LabView program. A four-wire scheme was used for all measurements, which uses one pair of wires for applying the current and one pair of wires with low current for sensing the voltage, to correct for voltage drop along the wires. Two different light sources were used for illumination, and the source is noted when measurements are presented. One source is a 175 W xenon lamp (ASB-XE-175EC, CVI Spectral Products) with filters to improve the spectrum relative to the AM1.5 G spectrum. A calibrated Si photodiode (S2386-44K, Hamamatsu) was used

with the measured spectrum of the light to estimate the irradiance of the source. The other source is an AM1.5 G solar simulator (91160, Oriel), and the irradiance was measured with a thermal detector (PM100, Thorlabs).

Because of spectral mismatch between the two sources and the AM1.5 G spectrum, the xenon source tends to over-estimate power conversion efficiencies while the solar simulator tends to under-estimate for organic solar cells. In some cases, adjustments were made to correct for spectral mismatch and are noted. In other cases, no corrections were made, so the measurements cannot be interpreted as absolute efficiencies for AM1.5 G illumination. However, the focus of this research is never on comparing the absolute efficiency of devices but rather on changes in devices with different materials and geometries. As such, these trends are still relevant since the devices were measured under the same source when comparing. All measurements were made at ambient conditions in the glovebox without additional cooling.

2.3.3 Temperature dependent measurements

J-V characteristics as a function of temperature were measured under vacuum in a cryostat (VPF-500, Janis) cooled with liquid nitrogen. Figure 2.3 shows a simple diagram of the cryostat. A sample is mounted on a cold finger which removes heat from the sample through thermal conduction to the liquid nitrogen in the dewar. A resistive heater included in the base of the sample mount is used to control the temperature over a wide range and measurements can even be taken above room temperature.

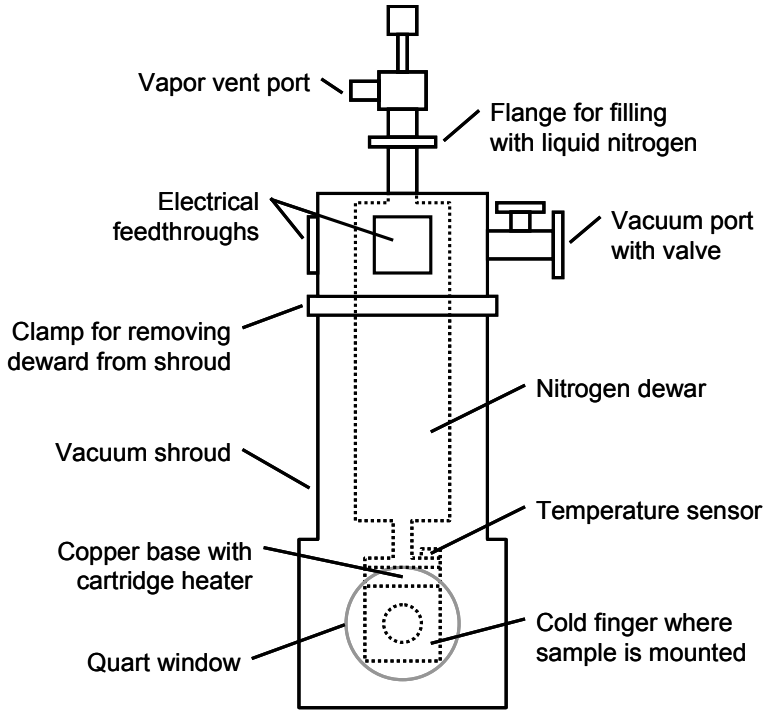

Figure 2.3. Diagram of the cryostat configuration. Dotted lines indicate parts inside the vacuum shroud.

To prevent exposure of the devices to ambient atmosphere, the cryostat was loaded into the glovebox where the sample was mounted and the cryostat sealed. A thin layer of thermal grease (Krytox LVP, Dupont) was applied between the substrate and the cold finger to enhance the thermal contact. The sealed cryostat was removed from the glovebox and pumped to below 10^{-5} Torr using a turbomolecular pump. The cryostat dewar was then filled with liquid nitrogen and allowed to cool to 77 K. After dwelling at 77 K for 20 minutes, measurements began.

Because of difficulties attaching a temperature sensor directly to the substrate, temperature was measured with a Si temperature sensor located just below the cold finger. To adjust for variations in temperature between the sensor and the substrate, a Si temperature sensor (DT-670, Lake Shore) was mounted with thermal epoxy (Stycast,

Lake Shore) to a 1" × 1" glass substrate to mimic the standard test solar cell. Prior to mounting, silver electrodes in the same shape as used in the solar cells were evaporated on the glass and the Si sensor leads connected to the silver electrodes with a silver paint. The Si sensor was then loaded into the cryostat in the same manner as the solar cell samples using the same wire connections, and the set point temperatures needed on the temperature controller (331, Lake Shore), which controls the power to the cartridge heater, to get the desired temperatures at the substrate were found.

Similarly, the intensity for the light source used for measurements under illumination had to be estimated at the substrate surface. Samples were illuminated through a quartz window in the cryostat and hole in the cold finger using a 180 W xenon lamp (66902, Oriel) with an AM1.5 G filter. Intensity was estimated using a photodiode (S1133, Hamamatsu) shown to have low spectral mismatch between many organic solar cells and solar simulators [104]. The photodiode was mounted in the cryostat, and the intensity of the lamp was adjusted to get the same current expected under AM1.5 G at 100 mW/cm^2 (1 sun) as estimated from EQE data.

After cooling a sample in the cryostat, *J-V* characteristics in the dark were taken from 120 K to 340 K in steps of 20 K. After reaching each set point temperature on the temperature controller, samples were given 10 minutes to reach equilibrium before measuring *J-V* characteristics. *J-V* characteristics in the light were measured under illuminations of approximately 1, 0.1, 0.09, and 0.0013 suns at 120, 180, 240, 300, and 340 K. After dwelling for 8 minutes at the initial set temperature, the samples were illuminated under 1 sun for 90 seconds to reach equilibrium and the *J-V* measured. The temperature was slightly raised (as determined by tests with the Si temperature sensor)

and the samples allowed to heat up for 150 seconds before measuring under the lower illuminations and in the dark.

2.3.4 Kelvin probe

The work function of the ITO and the modified ITO was measured in air with a Kelvin probe (Besocke Delta Phi). Kelvin probe measurements work by vibrating a non-contacting probe above the sample surface [105]. The capacitance between the probe and the surface will depend on the distance between the probe and the surface and the surface potential. Since the ac current in the probe caused by the capacitance change is related to the contact potential difference, the contact potential difference can be found from the bias voltage that eliminates the ac current. Kelvin probe is a relative measurement that only gives information on potential differences, so a highly oriented pyrolytic graphite sample with a work function of 4.5 eV was used as a reference.

2.4 Modeling

All of the modeling was performed in the mathematic software MATLAB. To facilitate the fitting of many *J-V* characteristics, a graphical user interface was developed to quickly choose the important fitting ranges, graph the results of the fitting procedures, and provide instant feedback on how changes in parameters affect the model curves.

CHAPTER 3

ORGANIC HETEROJUNCTIONS: PENTACENE / C_{60}

3.1 Introduction

As a relatively new technology, the understanding of the operation of organic solar cells is still relatively nascent and rapidly developing. Having an advanced understanding of the physics in organic solar cells is essential to improving performance and engineering the devices for different applications, and one of the goals of this research is to help develop this understanding. The purpose of this chapter is to first introduce the current state of knowledge regarding the operation and physics of organic solar cells. Once the basic concepts have been reviewed, pentacene / C_{60} solar cells are used as model devices to demonstrate the main characteristics of organic solar cells and how various models regarding performance compare with experimental data. The three main areas of operation that are covered are electrical characteristics, the photocurrent, and the open-circuit voltage. In particular, the origin of the open-circuit voltage is seen to be one area where additional emphasis is needed.

3.2 Organic Solar Cell Physics

The physics of organic solar cells is a heavily researched and rapidly developing area. While new pieces of the picture are being revealed constantly, several key mechanisms have gained traction as ways to explain the basic operation of organic solar cells. Before exploring these mechanisms, the fundamental properties of organic semiconductors and their differences with inorganic semiconductors must be understood.

From these basic concepts, a picture of the most important processes in organic solar cells can be formed.

3.2.1 Energy levels in organic semiconductors

The semiconducting properties of organic materials primarily originate from the delocalization of electrons in molecules with double bonds. In covalently bonded atoms, the shape of the electron orbitals around the atoms will be dependent on the atom and the number and type of bonds made with surrounding atoms. When the four valence electrons of a carbon atom interact with the valence electrons of another atom to form covalent bonds, the shape of the orbitals of the valence electrons is modified depending on the number and type of bonds made, leading to hybrid orbitals. The sp^2 hybridization that occurs when a carbon atom shares two valence electrons with a single atom and the two other valence electrons with two separate atoms is of particular interest. Other atoms (such as nitrogen and sulfur) can also exhibit sp^2 hybridization and are important in organic electronics, but carbon, which is the foundation of organic materials, will be considered here for demonstration purposes.

As shown in Figure 3.1(a), sp^2-hybridized atoms have three orbitals with significant overlap with the orbitals of the adjacent atoms. The large overlap leads to a strong covalent bond called a σ-bond. However, the 2p orbitals which are out of plane form a second bond with the same atoms, called a π-bond, with less overlap. The reduced overlap in π-bonds leads to the electrons being more weakly coupled and more delocalized in space. By alternating single and double bonds in a long chain, as shown in Figure 3.1(b), electrons in π-bonds can be delocalized over a long distance. This

delocalization is what will allow electrons in organic materials to move along molecular chains and hop between molecules.

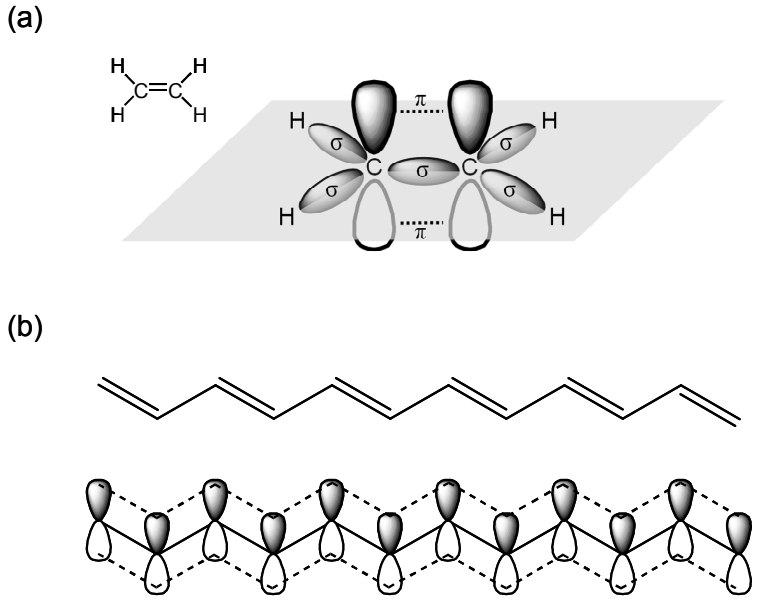

Figure 3.1. (a) Chemical structure and orbital structure of ethylene. (b) Schematic of conjugated carbon chain and p-orbitals showing how electrons can be delocalized over a long distance through π bonds.

The most important electrons to consider in the system will be the ones with the highest energy because they will be the easiest to excite or remove. The interaction of the electron orbitals will lead to a highest occupied molecular orbital (HOMO) that will primarily be determined by the π-electrons because they are more delocalized and have weaker bonding compared to electrons in σ-bonds. The next energy level will be the lowest unoccupied molecular orbital (LUMO), and is the lowest energy level to which electrons from the HOMO can be excited. The LUMO is also the orbital into which an additional electron could be accepted, giving the molecule a negative charge. Overlap of

the π molecular orbitals of adjacent molecules will also enhance the intermolecular coupling that allows electrons to transfer between molecules.

An analogy can be made between the valence and conduction band in inorganic semiconductors and the HOMO and LUMO levels in organic semiconductors. For both types of semiconductors, there is essentially a forbidden gap of energy levels between the valence and conduction band or the HOMO and LUMO levels. The reservoir of electrons in the valence band can be excited into the conduction band in inorganics; similarly, the electrons in organics will be excited from the HOMO into the LUMO. Whereas electrons can be injected into the conduction band of an inorganic semiconductor and move as negative charge carriers, electrons can be injected into the LUMO of organic semiconductors and move by hopping between molecules. In the same way, electrons can be removed from the valence band or HOMO to create mobile positive charges. While often used for convenience, this simplified view of the energy levels is far from complete.

Interactions between holes and electrons can lead to bound electron-hole pairs called excitons. For inorganic semiconductors, the binding energy of the electron and hole in the exciton is generally low because of the high dielectric constant of the materials and the periodicity and rigidity that lead to strong delocalization. On the other hand, excitons are relatively strongly bound in organic semiconductors because of geometry relaxation effects, lower dielectric constant and electron correlation, stronger Coulomb attraction, and stronger localization [106]. Excitons are especially important to consider when a hole and electron are formed in close proximity, as is the case with light absorption, a process essential to solar cells.

The exciton binding energy and changes in electronic structure result in the hole and electron in an exciton sitting at different energies than those of the HOMO and LUMO for a molecule in the ground state. Furthermore, singlet and triplet excitons with different spin multiplicities and energies can also exist [106]. The energy difference between the hole and electron in an exciton is often referred to as the optical gap [107]. To reach a charge-separated state in which the hole and electron can transport more freely, the exciton binding energy must be overcome. Holes and electrons in a charge-separated state will therefore have higher energies relative to those in the exciton. The difference between the energy levels of the hole and electron in a charge-separated state is the transport gap. The exciton binding energy is roughly equal to the difference between the optical gap and the transport gap [107].

The change in energy levels for holes and electrons in different exciton, charge-transfer, and charge-separated states means that the energy levels that must be considered in organic semiconductors are more complicated than simply the HOMO and LUMO in the ground state. The optical gap can be estimated from the onset of optical absorption, and the transport gap from the difference between the ionization potential and the electron affinity [108]. The ionization potential is the amount of energy needed to remove an electron from a molecule in ground state, and the electron affinity is the amount of energy needed to remove an electron from a molecule that already has a single, negative charge. Because HOMO and LUMO energies can only be calculated and not directly measured, ionization potential and electron affinity, measured by experimental methods such as ultraviolet photoemission spectroscopy and inverse photoemission spectroscopy, are often used as approximations to the HOMO and LUMO energies, respectively.

Though the rough analogy of HOMO and LUMO levels as the valence and conduction bands works to simply visualize the behavior of charge carriers in organic semiconductors, there are several significant differences between organic and inorganic semiconductors. Most importantly, charges are more localized in organic semiconductors. Pure inorganic crystals where all of the atoms in the crystal are covalently bonded together can have extremely long-range order and periodicity and rigid molecular structures that lead to delocalization of the electronic orbitals. This strong delocalization allows the charge carriers to have high mobility without being locally bound to atoms. Organic semiconductors do not have such a long-range order because they consist of many organic molecules that are not covalently bound. While electron delocalization is improved by the overlapping π-orbitals, the delocalization is weaker than in crystalline inorganics. Furthermore, the molecular structures are less rigid resulting in geometry changes as electrons are added and removed that can further affect the energy levels. For these reasons, charges are more localized in organic semiconductors and are treated as hopping from molecule to molecule.

The disorder of organic semiconductors significantly complicates the theoretical understanding of what is happening at a molecular level. Orientation of the molecules affects how the orbitals overlap. Geometry relaxations in different excited states change molecular shape and energy levels. Energy levels shift as more molecules are packed together. These, and many other considerations, all ultimately affect the charge transport properties in organic semiconductors and are not easily understood when dealing with systems involving billions of molecules. While advances continue to be made in understanding organic semiconductor processes at the molecular level, primarily

considering the HOMO and LUMO levels gives a simplified framework that has worked well for visualizing a very complex system. However, considerations at the molecular level need to be considered more and more to keep advancing organic electronics.

3.2.2 Photocurrent generation

The absorption of a photon in an inorganic solar cell can promote an electron from the valence band into the conduction band and lead to a free electron-hole pair because the binding energy between the electron and hole is small and easily overcome by the thermal energy (kT) at room temperature. The low binding energy is largely the result of the high dielectric constant of the materials and the periodicity and rigidity that create in the band structure. However, geometry relaxation effects, lower dielectric constant and electron correlation, and stronger Coulomb attraction in organic materials lead to a bound electron-hole pair, called an exciton, when light is absorbed in an organic semiconductor [109]. Excitons in organics, which typically have large binding energies on the order of 500 meV [106], must be dissociated into separate charges before they can contribute to photocurrent in an organic cell. This dissociation can be accomplished at the interface between an appropriately chosen electron donating material (donor) and an electron accepting material (acceptor) where it is energetically favorable for the exciton to dissociate with the electron in the acceptor and the hole in the donor. Figure 3.2(a) shows a simple energy-level diagram of this situation.

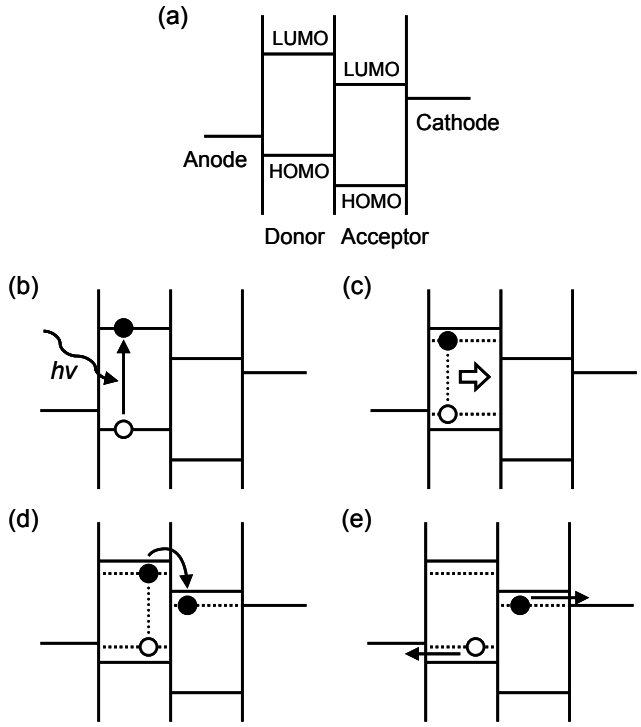

Figure 3.2. (a) Basic energy-level diagram for an organic solar cell. Based on the energy-level diagram, overview of the photocurrent generation process: (b) light absorption to create an exciton; (c) exciton diffusion to donor / acceptor interface; (d) exciton dissociation and charge separation; and (e) charge transport and collection at the electrodes.

Photocurrent generation in an organic solar cell generally occurs in four main steps (Figure 3.2). First, the absorption of a photon excites an electron from the HOMO of the organic material to create an exciton (Figure 3.2b). Next, the exciton must diffuse to the donor / acceptor interface to dissociate into charge carriers (Figure 3.2c). Because excitons have no net charge, their diffusion is generally treated as a random process based on concentration gradients without influence from electric fields [106]. However, excitons can recombine during the diffusion process before reaching the donor / acceptor interface, leading to absorbed photons that do not contribute to the current. The characteristic length an exciton travels before recombining is described by the exciton

diffusion length. Exciton diffusion length affects device design because of the trade-off between light absorption and recombination as layer thickness is changed.

Excitons that do reach the donor / acceptor interface can then dissociate into electrons and holes (Figure 3.2d). However, there is still no clear understanding of exactly how exciton dissociation occurs on a molecular level [106]. Generally, the process is described as the changing of the exciton state at the interface into a charge transfer state between an adjacent donor and acceptor followed by either recombination or dissociation into a charge-separated state. While this is the most repeated description, the entire picture is most likely more complicated, involving processes such as the interaction of additional states, the possibility of energy transfer, and the formation of different types of excitons, with the ultimate outcome determined by the relative rates of all the interactions [106]. While the full story is still the subject of much research, it appears that the energy change in going from a bound electron-hole pair to a hole in the donor (with an energy roughly estimated by the ionization potential) and an electron in the acceptor (roughly estimated by the electron affinity) is what ultimately leads to free charges.

Finally, the charges are transported through the semiconductors and collected by their respective electrodes (Figure 3.2e). Unlike inorganic semiconductors, the charges in organic materials are generally more localized and travel through hopping processes. The different transport mechanisms lead to mobility values typically below 1 $cm^2V^{-1}s^{-1}$ that can have different dependences on temperature and electric field compared to in inorganic materials. Also, choice of electrode materials and modification of the contact

between the electrode and organic is another area undergoing active research that can significantly affect the ability to extract the generated charges.

3.2.3 Photovoltage

Another process that is important to understand is what determines the open-circuit voltage in an organic solar cell. Originally, open-circuit voltage was thought to be determined by the difference in the work function of the two electrodes used to make a device [110, 111]. These observations led to the notion that the open-circuit voltage is primarily determined by a built-in electric field in the devices. It was soon found that the work function of the electrodes only affected the open-circuit voltage when good ohmic contact was not made with the organic layers [112].

By studying cells made with different donor and acceptor materials, several studies have reported a correlation between the open-circuit voltage and the difference between the HOMO, or the ionization potential, of the donor and the LUMO, or the electron affinity, of the acceptor in both planar-heterojunction [108, 113, 114] and bulk-heterojunction [111, 115, 116, 117, 118] devices. While a correlation does appear to exist, values of open-circuit voltage often differ substantially from those predicted by the difference between the HOMO of the donor and the LUMO of the acceptor [119].

From studying these trends, Scharber *et al.* have suggested an empirical equation relating the open-circuit voltage to material properties in bulk-heterojunction cells using PCBM as the acceptor:

$$V_{\mathrm{OC}} = (1/e)\left(\left|E_{\mathrm{HOMO}}^{\mathrm{Donor}}\right| - \left|E_{\mathrm{LUMO}}^{\mathrm{Acceptor}}\right|\right) - 0.3\ \mathrm{V}, \tag{3.1}$$

where e is the elementary charge, and E is the HOMO energy of the donor or the LUMO energy of the acceptor [117]. The additional loss of 0.3 V is an empirical factor that has been attributed to dark current of the diode and the field-driven nature of the photocurrent.

Similarly, Rand *et al.* looked at the maximum open-circuit voltage at any irradiance and temperature and suggested that this voltage is equal to the difference between the ionization potential of the donor and the electron affinity of the acceptor, which are close to the energy that a hole and electron are likely to initially have, minus an additional energy needed to separate the hole and electron [108]. In this case, the maximum open-circuit voltage can be written as

$$eV_{\mathrm{OC}}^{\max} = \mathrm{IP}_D - \mathrm{EA}_A - \frac{e^2}{4\pi\varepsilon_0\varepsilon_r r}, \tag{3.2}$$

where IP_D is the ionization potential of the donor, EA_A is the electron affinity of the acceptor, ε_0 is the vacuum permittivity, ε_r is the relative dielectric constant of the organic material, and r is the initial separation distance of the optically generated hole and electron pair in the donor and acceptor layers immediately after charge transfer. The third term in Equation 3.2 is the energy needed to overcome the Coulombic attraction between a hole on a donor molecule and an electron on an acceptor molecule, thereby separating the hole and electron.

An outcome of these observations is that many researchers have attributed the open-circuit voltage to a built-in field caused by the difference in the HOMO of the donor and the LUMO of the acceptor [111, 117]. While both of these equations generally do a fair job of relating material properties to open-circuit voltage, large variations do often occur [119]. Another limitation of these empirical formulas is that they do not give a good sense of what molecular processes lead to the open-circuit voltage and how the

processes relate back to the *J-V* characteristics of the device. However, it is clear that no correlation between the optical gap and the open-circuit voltage are found as predicted in ideal devices by Shockley and Queisser [119]. Developing a better physical understanding of the processes governing open-circuit voltage and how it is related to molecular interactions in organic solar cells is important.

3.3 Current-Voltage Characteristics of Pentacene / C_{60} Solar Cells

The next sections use pentacene / C_{60} solar cells as a model system to look at how some of the present models and understanding of the physics of organic solar cells apply to real devices and experimental data. A schematic of the basic device structure along with the chemical structures of the organic semiconductors can be found in Figure 3.3. The layer thicknesses used are pentacene (50 nm) / C_{60} (45 nm) / BCP (8 nm) / Al (200 nm). Details of the fabrication can be found in Section 2.2.

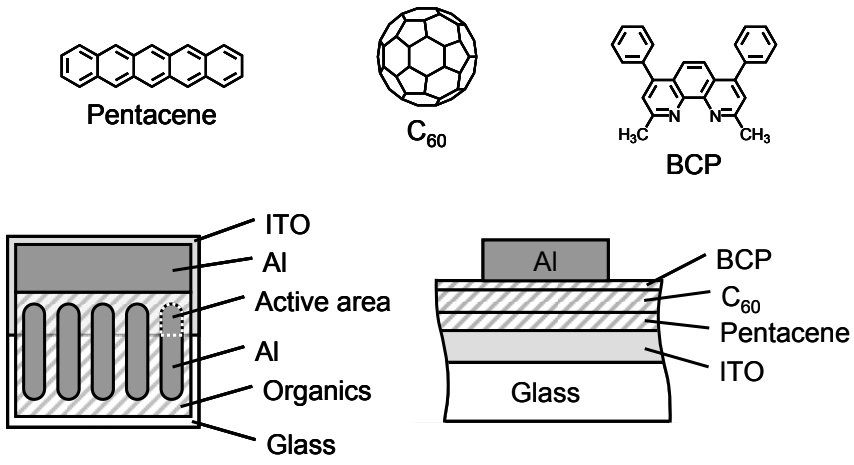

Figure 3.3. Chemical structures of organic semiconductors and top and cross-sectional view of basic pentacene / C_{60} device structure.

3.3.1 Pentacene / C_{60} solar cell performance

Figure 3.4 shows the *J-V* characteristics and EQE for a typical pentacene / C_{60} solar cell with an area of 0.1 cm^2. Averaged over three devices on the same substrate, performance parameters of J_{SC} = 12.1 ± 0.4 mA/cm^2, V_{OC} = 367 ± 2 mV, FF = 0.54 ± 0.01, and η = (3.1 ± 0.1)% were measured under the illumination of a filtered broadband light source with an irradiance of 78 mW/cm^2. In the dark and under illumination, the *J-V* characteristics show the rectifying, exponential behavior of a diode expected for solar cells based on junctions as described in Section 1.3.

To correct for spectral mismatch between the experimental light source and the standard AM1.5 G spectrum, J_{SC} expected under the AM1.5 G spectrum can be calculated from Equation 1.4. Because the EQE was measured at low light intensities, this calculation will only be accurate if the short-circuit current is a linear function of irradiance, as is expected for ideal devices and has been demonstrated in pentacene / C_{60} [120]. For these devices, J_{SC} of 9.3 mA/cm^2 is estimated for the AM1.5 G spectrum, giving η = 1.8% under AM1.5 G illumination.

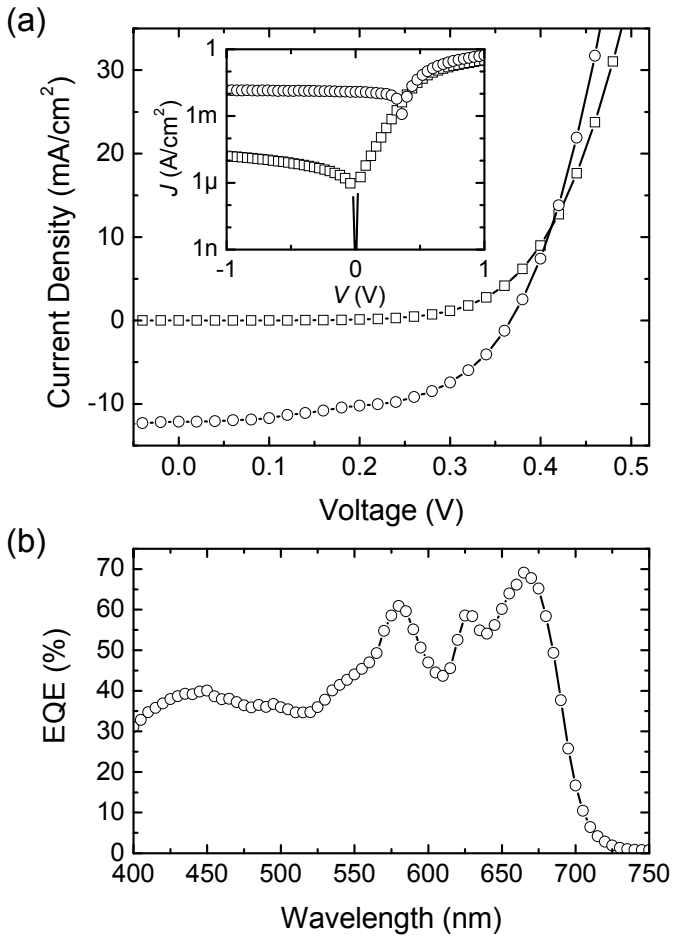

Figure 3.4. (a) Experimental data for a pentacene / C_{60} device in the dark (squares) and under illumination (circles). Inset shows the same data on semilogarithmic axes. (b) The EQE of the device in (a). Lines are merely guides for the eye.

The EQE spectra of organic solar cells also tend to have more complex shapes relative to those of inorganic solar cells. The peaks in the EQE arise from the electronic structure of many organic materials leading to peaks throughout the absorption spectra instead of broad, uniform absorption. These unique absorption spectra can be used to make transparent devices that can be used as colored glass [121, 122, 123, 124, 125, 126].

3.3.2 Equivalent circuit model

Models that can fit *J-V* curves over a wide range of voltages can be very useful for understanding how modifications in devices change their performance and for designing systems that use the devices. The equivalent circuit model that was originally developed to simulate and understand the *J-V* characteristics of inorganic solar cells can also be applied to organic solar cells [15, 120]. The model uses several basic circuit elements that each account for different processes in a solar cell, and *J-V* curves can be calculated from the circuit using basic circuit theory. Figure 3.5 shows a schematic of the equivalent circuit, which consists of a parallel-connected current source, diode, and parallel resistance connected in series with an additional series resistance. It should be noted that, while the model does work well for many organic devices, how to derive the model from basic principles in organic semiconductors is still not clear.

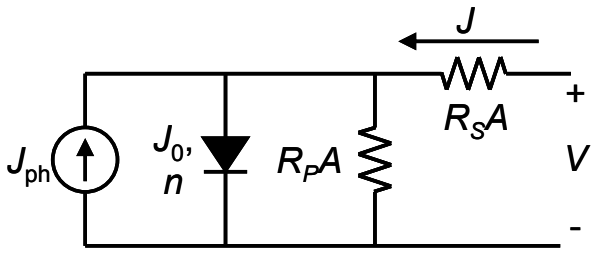

Figure 3.5. Equivalent circuit model for solar cells.

The current source represents the photocurrent J_{ph} generated in the device when under illumination. This term will depend on the spectrum and intensity of the incident light; thus, J_{ph} is zero for a device in the dark. The diode accounts for the rectifying behavior of the donor-acceptor heterojunction and is characterized by the reverse saturation current density J_0 and the ideality factor n. Because diodes follow an

exponential curve, the reverse saturation current density is the current density of an ideal diode when biased with a negative voltage. The ideality factor is related to the slope of the exponential curve, with an ideal diode having an n of unity. Ideality factors greater than unity yield exponential curves that increase more slowly and may be caused by factors such as recombination currents.

The parallel resistance R_PA allows for leakage currents that are not attributed to the diode from sources such as leakage, pinholes, and recombination. Ideally, R_PA should be high to minimize losses from current circumventing the load. Finally, the series resistance R_SA accounts for the finite resistance of the organic layers and electrodes along with the contact resistance between each of the interfaces. The series resistance prevents the exponential diode from increasing to infinitely large currents and should be small to minimize electrical power losses caused by the resistance limiting the current in the device.

From the equivalent circuit model, the equation for the J-V characteristics of a solar cell can be derived as

$$J = J_0\left\{\exp\left(\frac{V - JR_SA}{nkT/e}\right) - 1\right\} + \frac{V - JR_SA}{R_pA} - J_{ph}, \tag{3.3}$$

where k is the Boltzmann constant, T is the temperature, e is the elementary charge, and A is the area of the device. This equation can be fitted to experimental data using R_SA, R_PA, J_0, and n as the fitting parameters. Comparison of these parameters for devices with different materials and geometries can then yield information on how the changes affect different aspects of the device.

Furthermore, the open-circuit voltage can be estimated by solving Equation 3.3 at open-circuit conditions, *i.e.*, $J = 0$ mA/cm^2. Solving the equation and assuming that R_PA is high and $J_{SC}/J_0 >> 1$, as should be the case in most good devices, gives

$$V_{OC} = n\frac{kT}{e}\ln\left\{1+\frac{J_{ph}}{J_0}\left(1-\frac{V_{OC}}{J_{ph}R_PA}\right)\right\} \approx n\frac{kT}{e}\ln\left\{1+\frac{J_{SC}}{J_0}\right\} \approx n\frac{kT}{e}\ln\left\{\frac{J_{SC}}{J_0}\right\}. \qquad (3.4)$$

Therefore, the equivalent circuit model shows that the primary factors influencing V_{OC} should be n, J_{SC}, and J_0. Similarly, J_{SC} can be calculated by setting $V = 0$ V. J_{SC} will be close to J_{ph} if R_SA is small but can decrease substantially with increasing R_SA.

It should be noted that more complicated models have also been proposed using large sets of equations that attempt to include additional effects, like intermolecular-charge-transfer rates, separation probabilities for the excitons, and field dependence of the photocurrent [127, 128, 129, 130]. However, the additional complexity introduces many new parameters that are not well known and must be assumed, such as mobilities, charge transfer and recombination rates, and charge carrier densities. For this reason, the equivalent circuit model can be convenient in that it minimizes the number of fitting parameters needed to fit the curves.

3.3.3 Model fitting

The parameters n, J_0, J_{ph}, R_PA, and R_SA can all be extracted from the *J-V* measurements of a device by fitting the model to experimental data [120]. Estimates of R_SA and R_PA can be found from the inverse slopes of the forward and reverse characteristics, respectively. When fitting data in the dark, the estimates of R_SA and R_PA can be used to effectively remove the effect of the resistances on the diode by defining $V' = V - JR_SA$ and $J' = J - V'/R_PA$. J_0 and n can then be calculated from the *y*-intercept and

slope, respectively, of a straight line fit to the linear portion of ln(J') vs. V' in the forward bias. When fitting data under illumination, the additional experimental parameters of FF and J_{SC} can be used, and J_0 and n can then be calculated as the values that give the same FF and J_{SC} as measured experimentally for the given estimates of R_SA and R_PA. R_SA and R_PA are then varied until the minimum of the sum of the logarithm of the squared error between the experimental and fitted values over the entire curve are found. The logarithm is used to give small values of J, which can vary a wide range, similar weight as the large values.

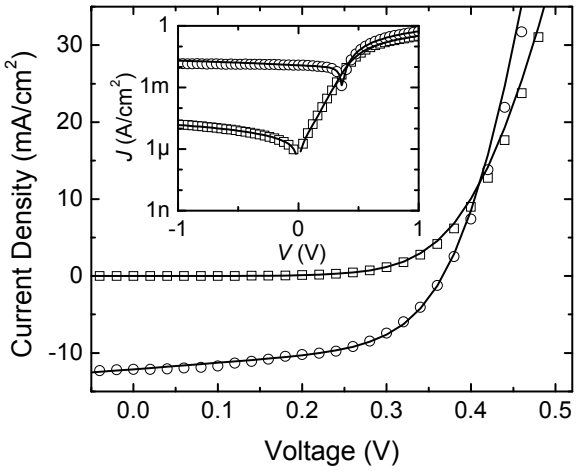

Figure 3.6. Curves fitted to experimental pentacene / C_{60} device data in the dark and light using the equivalent circuit model.

Figure 3.6 shows model curves fitted to the experimental data for the pentacene / C_{60} cell from Figure 3.4. The parameters for the model for these curves are J_0 = 0.757 µA/cm^2, n = 1.57, R_SA = 1.45 Ωcm^2, and R_PA = 70.6 kΩcm^2 in the dark and J_0 = 0.970 µA/cm^2, n = 1.55, R_SA = 0.863 Ωcm^2, and R_PA = 120 Ωcm^2 in the light. Looking at the region where the device is producing power from 0 to 0.36 V, the equivalent circuit

model closely follows the behavior of the device. Furthermore, the semilogarithmic graph indicates that the model can also fit more than just the power-producing region of the *J-V* curves with good agreement all the way to ±1 V. The ability of the model to reproduce the *J-V* characteristics of organic solar cells indicates that studying the change in parameters for different devices will be useful in understanding the origin of the change.

Rather large changes in J_0, n, and $R_P A$ between the model parameters in the light and in the dark are sometimes observed for bulk-heterojunction [131, 132] and other small-molecule solar cells [15, 133]. The origins of these differences have been related to phenomena such as an intensity dependence of J_{SC} that is not accounted for in the simple model [131], photoconductance effects under illumination in organic materials that generally have low intrinsic charge densities in the dark [53, 131, 134], and field dependence of the mobility in organic semiconductors [134]. Various models have been proposed to account for the illumination dependence of the parameters [120, 131, 134], though most rely on finding empirical relations for the changes and add parameters that cannot necessarily be independently verified and may serve more to simply improve the quality of the fitted curves.

For the purposes of this thesis, the model will primarily be applied to experimental data in the dark to minimize the number of fitting parameters while maximizing the usefulness of each one. While certain material combinations may have unique changes in behavior under illumination compared to in the dark, this level of detailed analysis is beyond the scope of the research at this time and may be pursued more in depth in the future using the data that has already been collected here or with further experiments. The observation that large changes in device performance under

illumination are also always accompanied with large changes in the dark characteristics also justifies this approach.

3.4 Short-Circuit Current in Pentacene / C_{60} Solar Cells

As discussed in Section 3.2.2, photocurrent generation in organic solar cells encompasses the processes of photon absorption to create excitons, exciton diffusion to a donor / acceptor interface, exciton dissociation at the donor / acceptor interface into separate charges, and charge transport through the semiconductor for collection at the electrodes. If the donor and acceptors are well chosen, the exciton dissociation at the interface should occur efficiently. The most important material properties regarding photocurrent are then the absorption of the active layer and the exciton diffusion length, the characteristic distance excitons travel before recombination. Because of the relatively simple geometry of planar heterojunction solar cells such as the pentacene / C_{60} being discussed here, models have been developed based on the described photocurrent generation process that can relate EQE and photocurrent to the absorption spectra, layer thicknesses, and exciton diffusion lengths in a device. The main theory behind the model will be explained here to show its applicability to pentacene / C_{60} solar cells, but detailed explanations can be found in [135] and [136].

3.4.1 Model for external quantum efficiency

The main premise of the model for EQE is to treat the layers of a planar heterojunction as ideal, semi-infinite planes with different optical constants and exciton diffusion lengths in each layer. From the optical constants, the distribution of the optical field and the generation rate of excitons from absorbed photons can be calculated. The distribution of excitons in the device can then be calculated from the generation rate by

applying a one-dimensional diffusion model with appropriate boundary conditions and an exciton diffusion length in each layer. Finally, the rate of excitons reaching the donor / acceptor interface for dissociation into electrons and holes can be related to the photocurrent in the device.

Based on the optical constants and the thicknesses of each layer in a device, the optical field in each layer can be elegantly calculated using transfer matrix methods. The outcome of the calculations is that the optical field in each layer can be written as

$$\left|E(z)\right|^2 = \left|t^+\right|^2 \left|E_0^+\right|^2 \left[e^{-\alpha z} + \left|r^{(R)}\right|^2 e^{-\alpha(2d-z)} + 2\left|r^{(R)}\right| e^{-\alpha d} \cos\left\{ \frac{4\pi}{\lambda} n(d-z) + \delta^{(R)} \right\} \right] \quad (3.5)$$

where E is the field, z is the position in the device, E_0^+ is the incident field, α is the absorption coefficient, t^+ and r are the transmission and reflection coefficients, d is the thickness of the current layer, λ is wavelength, n is the index of refraction, and δ is the phase of the reflection coefficient r. The first and second terms in the hard brackets of Equation 3.5 are from the propagating and counter-propagating field, respectively, while the last term is related to the interference effects. Full calculations for the individual coefficients can be found in [135] and [136].

From the optical field, the generation of excitons at each wavelength as a function of thickness is calculated from the absorption in each layer by

$$G(z) = \frac{\frac{1}{2} c \varepsilon_0 \alpha n \left|E(z)\right|^2}{hc/\lambda}, \quad (3.6)$$

where c is the speed of light, ε_0 is the permittivity of free space, and h is Planck's constant. The absorption coefficient is related to the optical constant k by

$$\alpha = 4\pi k/\lambda. \quad (3.7)$$

To find the exciton distribution, the continuity equation can be applied with a one-dimensional diffusion model for exciton movement, the generation rate from Equation 3.6, and recombination in the bulk to get

$$D\frac{\partial^2 p}{\partial z^2} + G - \frac{D \cdot p}{L^2} = 0, \tag{3.8}$$

where p is the exciton distribution and D and L are the diffusion constant and diffusion length, respectively, for excitons in the layer. Boundary conditions must be chosen to solve Equation 3.8 in each layer. A robust solution that can take into account additional effects and be found by applying the concept of surface velocity at each interface expressed as

$$D\frac{\partial p}{\partial z}\bigg|_{z=z_0} = S \cdot p(z_0), \tag{3.9}$$

where z_0 is the interface and S is the interfacial exciton-quenching velocity. S describes the recombination of excitons at the interface, and $S = 0$ corresponds to no recombination while $S = \infty$ corresponds to complete quenching at the interface.

The exciton distribution can then be solved using an ideal case of an infinite surface velocity at the heterojunction interface, indicating that all excitons are being dissociated into charges, and a surface velocity of zero at all other interfaces, indicating that there is no recombination or dissociation of excitons at the other interfaces. These assumptions are for an ideal situation and result in conservative values of the exciton diffusion length since the donor / acceptor interface is assumed to be perfectly efficient at dissociating excitons and recombination only takes place in the bulk and not at the other interfaces. From the distribution, the flow of excitons being dissociated at the

heterojunction interface can be calculated and related back to the current in the device by assuming a carrier collection efficiency, generally of unity.

The final parameters for the model are *n*, *k*, *L*, *S*, and the layer thicknesses. Knowing the optical constants and device geometry and assuming ideal values for *S*, insight into the exciton diffusion length in the donor and acceptor layers can be gained by fitting the model to measured EQE data using the diffusions lengths as the fitting parameters. Additional insight could be gained into the other interfaces in the device by also using *S* as a fitting parameter and looking at devices with different thicknesses.

3.4.2 Results for pentacene / C_{60}

Figure 3.7 shows the optical constants of pentacene and C_{60}, the calculated optical field distribution in a pentacene / C_{60} device, and experimental and modeled EQE values using the previously discussed model for a pentacene / C_{60} solar cell. The optical field distribution in Figure 3.7(b) illustrates the importance of interference effects in the solar cell. Because of the layer thicknesses and interference effects, the optical field at 440 nm is maximized in the C_{60} layer and at 670 nm in the pentacene layer. This field distribution is advantageous because C_{60} has a peak in absorption at 440 nm and pentacene at 670 nm. By carefully choosing the layer thicknesses, optical interference effects can be used to enhance the field in the layers that best absorb those wavelengths. If thicknesses had been chosen such that minimums of the optical field occur in layers at wavelengths that have the highest absorption of those wavelengths, photocurrent could be significantly reduced. Thicknesses cannot be chosen solely based on the optical interference effects because limited exciton diffusion length must also be taken into account, and transparent optical

spacers have been suggested as one way to enhance the optical field and increase photocurrent.

The experimental EQE in Figure 3.7(c) were fitted to the model using the exciton diffusion lengths in pentacene and C_{60} as the fitting parameters. The model yielded exciton diffusion lengths of 19 nm in C_{60} and 70 nm in pentacene. The long exciton diffusion length in pentacene is thought to be important to the high EQE displayed in the portion of the spectrum where pentacene absorbs light. Also plotted in Figure 3.7(c) are EQE curves calculated using the model with exciton diffusion lengths of 19 nm in C_{60} and lengths ranging from 20 nm to 100 nm in pentacene. The calculations show that diffusion lengths of 20 or 40 nm, similar to what have been reported for other materials [137], would lead to a much lower EQE in the pentacene / C_{60} device. However, exciton diffusion lengths in the range of 60 nm to 100 nm have less of an effect on the modeled EQE. This modeling suggests that the exciton diffusion length in pentacene is longer that of many other organic materials and is important for the high EQE values that have been obtained. The blended structure of bulk-heterojunctions makes it difficult to apply this model to those devices.

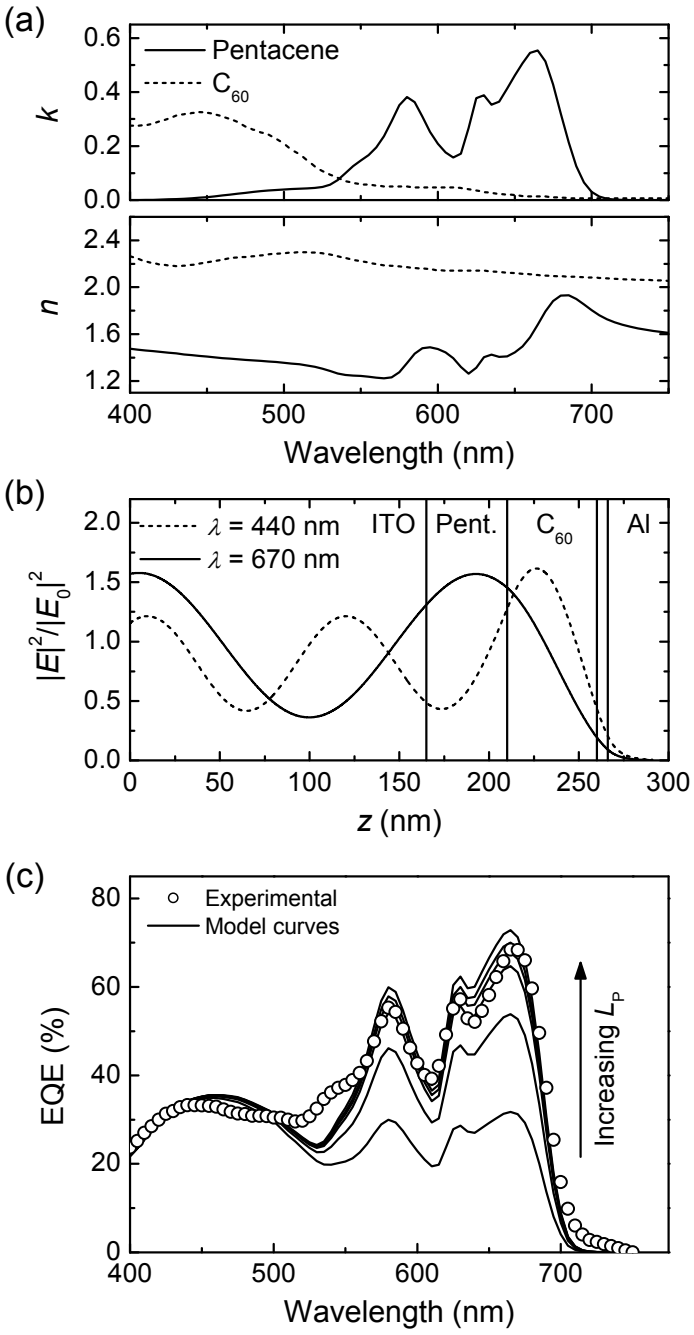

Figure 3.7. (a) Optical constants for pentacene (solid line) and C_{60} (dashed line) measured on glass and silicon, respectively. (b) Calculated field distribution normalized to incident field as a function of depth in an ITO / pentacene / C_{60} / BCP / Al stack at 440 nm (dashed line) and 670 nm (solid line). (c) Experimental EQE (symbols) for pentacene / C_{60} devices with model curves (lines) calculated for an exciton diffusion length of 19 nm in C_{60} and 20, 40, 60, 70, 80, or 100 nm in pentacene.

3.5 Open-Circuit Voltage in Pentacene / C_{60} Solar Cells

Having previously discussed the *J-V* characteristics and short-circuit current in pentacene / C_{60} solar cells, this section will begin to explore what influences V_{OC}. The majority of reports have related V_{OC} in organic solar cells to either the difference in the work function of the electrodes [110, 111] or the difference between the HOMO level of the donor and the LUMO level of the acceptor [108, 117], as detailed in Section 3.2.3. Each of these ideas will now be investigated with pentacene / C_{60} solar cells by first changing the work function of each electrode and then by changing the donor itself. Figure 3.8 shows a simple energy level diagram for the pentacene / C_{60} devices having electrodes with different work functions that will be studied.

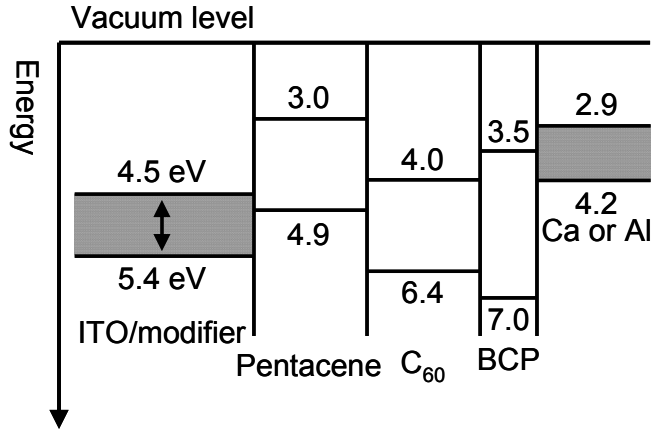

Figure 3.8. Simple energy level diagram of ITO / modifier / pentacene / C_{60} / BCP / metal devices indicating the range of work function changes for the two electrodes that will be explored.

3.5.1 Modification of anode

The work function of the anode can be modified through surface modification of the ITO. The two methods for modifying the surface that will be used are the

incorporation of an organic surface modifier and air plasma treatment [138, 139, 140]. The organic modifier comprises of a phosphonic acid moiety, which attaches to the ITO surface, covalently bonded to various dipolar functional groups. Kelvin probe measurements show that the ITO work function can be varied between 4.5 eV for untreated ITO and 5.4 eV for ITO treated with air plasma. Use of pentafluorobenzyl phosphonic acid (F5BPA, see Figure 3.9) on the surface of the ITO resulted in a work function value of 4.9 eV. Pentacene / C_{60} devices were fabricated on top of the modified ITO in the same way as all of the previously presented devices. Details of the surface modification and fabrication can be found in Section 2.2.

Figure 3.9 shows the *J-V* characteristics for the devices in the dark and under illumination (ASB-XE-175EC, ~100 mW/cm^2). Table 3.1 summarizes the performance parameters for each geometry averaged over three devices. Even with the large change in work function of the ITO, no significant difference in V_{OC}, J_{SC}, or FF is observed. These data are in contradiction to the idea that V_{OC} in organic solar cells is primarily determined by the difference between the work function of the electrodes.

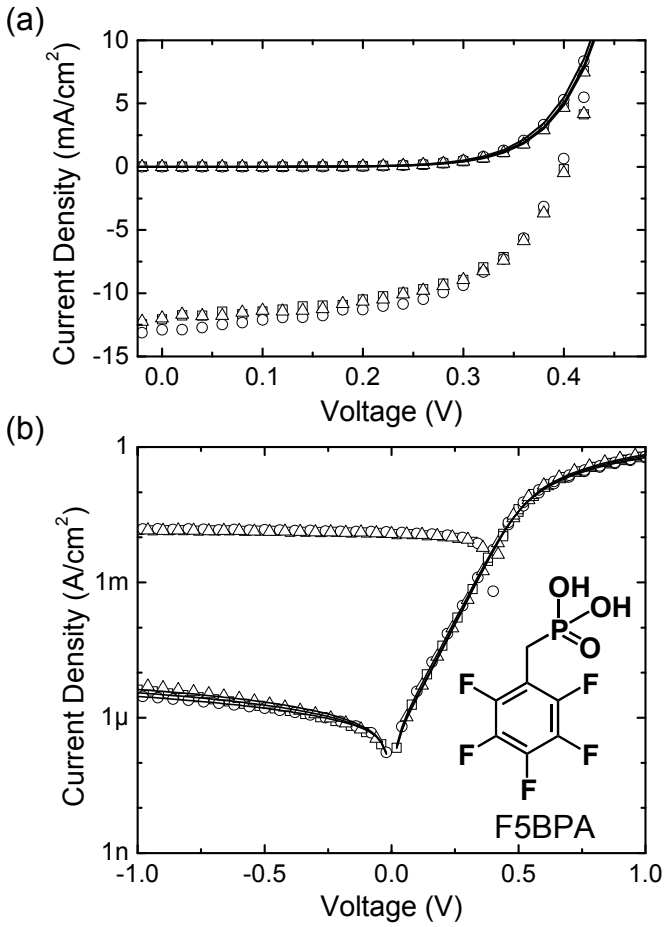

Figure 3.9. (a) Experimental data for pentacene / C_{60} devices on ITO with different surface modifications: unmodified (squares), F5BPA (circles), and air plasma (triangles). Solid lines are curves fitted to the circuit model in the dark. (b) The same data on a semi-logarithmic plot over a wider range of voltages along with the structure of F5BPA.

To verify that changing the work function of the ITO has little discernable effect on the device, experimental data in the dark were fitted to the equivalent circuit model. Figure 3.9(b) shows the experimental data with the model curves using the parameters listed in Table 3.1. With very little difference between each of the parameters, changing the work function of the ITO with surface modification does not appear to have any significant impact on the device that can be associated with a particular parameter or process. Furthermore, modeling of diodes based on single layers of pentacene

sandwiched between modified ITO and Al electrodes suggest that the barrier for injection into the pentacene does not significantly change with the ITO work function, which may be the result of Fermi level pinning [140].

Table 3.1. Performance parameters for pentacene / C_{60} solar cells on ITO with different surface modifications and fitting parameters for the equivalent circuit model.

Surface modifier	V_{OC} **(mV)**	$\lvert J_{SC}\rvert$ **(mA/cm^2)**	***FF***	J_0 **(μA/cm^2)**	***n***	R_SA **(Ω cm^2)**	R_PA **(kΩ cm^2)**
Unmodified	405 ± 2	13 ± 1	0.55 ± 0.01	0.23	1.53	0.648	298
F5BPA	399 ± 2	13 ± 0.2	0.55 ± 0.01	0.30	1.56	0.708	375
Air plasma	402 ± 1	12 ± 0.4	0.56 ± 0.01	0.20	1.52	0.600	247

These results show that the work function of the anode does not necessarily have a strong influence on V_{OC} for organic solar cells. However, the use of different anodes could still significantly alter device performance for other reasons, such as if the morphology of the active layer is modified or if the anode is too resistive. Also, work function can have a stronger influence in bulk-heterojunction devices because of the electrode's role in determining the type of charge collected from the blended active layer [112].

3.5.2 Change of cathode metal

Next, metals with different work functions were used as the cathode to continue to investigate how the work function difference between the two electrodes affects V_{OC} in organic solar cells. Using the same structure without any ITO modification, Al or Ca was deposited as the cathode. With a work function of 2.9 eV, Ca has a work function that is

1.3 eV lower than Al and should lead to a large increase in V_{OC} if organic solar cells follow the operation of metal-insulator-metal devices.

Figure 3.10 shows the experimental *J-V* curves for the devices in the dark and under illumination (ASB-XE-175EC, ~100 mW/cm^2), and the performance parameters averaged over three samples for each cathode are summarized in Table 3.2. The devices with Ca as the cathode yield V_{OC} values only 5 mV larger than the Al cathode devices despite the difference of 1.3 eV in work function. Only J_{SC} differs significantly for the Ca devices and is ~33 % smaller than the Al devices. The decrease in J_{SC} can be attributed to the lower reflectance of Ca compared to Al, which gives less light a second pass through the device and a second chance at absorption [141]. The lower values in V_{OC} and J_{SC} compared to the surface modified devices are within the range expected for batch-to-batch variations.

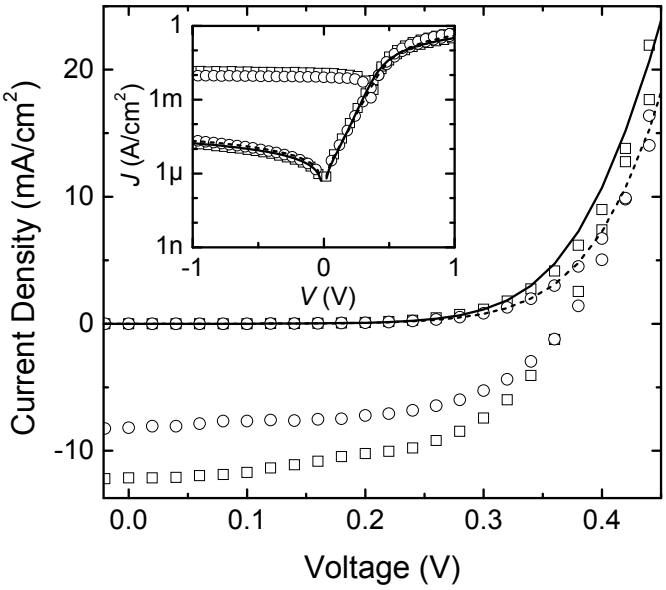

Figure 3.10. Experimental data for pentacene / C_{60} devices with different cathodes: Al (squares) and calcium (circles). The solid line is a model fit for the Al device, and the dashed line for the Ca device. Inset shows the same data on a semi-logarithmic scale.

Table 3.2. Performance parameters for pentacene / C_{60} solar cells with different cathodes and fitting parameters for the equivalent circuit model

Cathode	V_{OC} (mV)	$\|J_{SC}\|$ (mA/cm^2)	*FF*	J_0 (μA/cm^2)	*n*	R_SA (Ω cm^2)	R_PA (kΩ cm^2)
Ca	371 ± 2	8.1 ± 0.1	0.56 ± 0.01	0.615	1.62	1.09	48.4
Al	367 ± 2	12.1 ± 0.4	0.54 ± 0.01	0.414	1.46	1.53	60.1

Again, the equivalent circuit model can be used to more closely evaluate whether the change in cathode had any significant impact on the device that is not obvious by just visually observing the *J-V* characteristics. Included in Figure 3.10 are lines calculated from fitting the model to the experimental data in the dark using the parameters in Table 3.2. Though there is a small difference in J_0 most likely related to batch-to-batch variations, the difference is not large enough to significantly affect V_{OC} because it is related to $\ln(J_{SC}/J_0)$, so much bigger changes in J_0 must be made to impact V_{OC} (see Equation 3.4).

3.5.3 Use of different donor layers

Finally, the pentacene layer was replaced with the donors copper phthalocyanine (CuPc), tetracene, and titanyl phthalocyanine (TiOPc). These donors were chosen because of their difference in HOMO levels, with pentacene having the lowest and TiOPc the highest. While the C_{60} (45 nm) and BCP (8 nm) layers were kept the same thicknesses, the thicknesses of the donor layers were adjusted according to what has been reported in literature to maintain good J_{SC} in the devices since the donors have different exciton diffusion lengths. An additional layer of PEDOT:PSS was used between the ITO and tetracene layer because poor film quality was obtained without the PEDOT:PSS. Representative *J-V* curves for the devices in the dark and under illumination (Oriel 91160,

~100 mW/cm^2) are in Figure 3.11, and Table 3.3 summarizes the donor properties and the performance parameters.

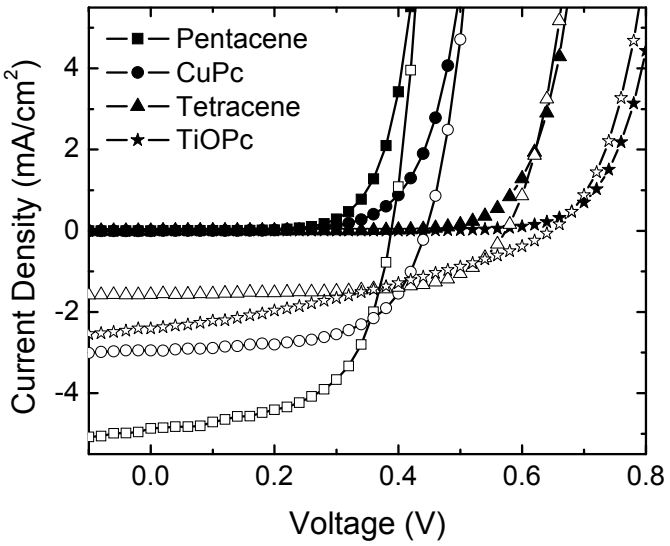

Figure 3.11. Experimental data for donor / C_{60} devices with different donors: pentacene (squares), CuPc (circles), tetracene (triangles), and TiOPc (stars).

Table 3.3. Performance parameters of donor / C_{60} solar cells. The light source is an AM1.5 G solar simulator (91160, Oriel) with an irradiance of 100 mW/cm^2.

Donor	**HOMO (eV)**	**Thickness (nm)**	V_{OC} **(mV)**	$\|J_{SC}\|$ **(mA/cm^2)**	***FF***	η **(%)**
Pentacene	4.9	50	391 ± 3	5.0 ± 0.2	0.58 ± 0.01	1.1 ± 0.1
CuPc	5.3	20	444 ± 1	2.9 ± 0.1	0.61 ± 0.01	0.78 ± 0.02
Tetracene	5.4	80	569 ± 6	1.6 ± 0.1	0.58 ± 0.02	0.58 ± 0.02
TiOPc	5.4	18	649 ± 7	2.4 ± 0.1	0.33 ± 0.02	0.52 ± 0.02

If the electrodes primarily determined V_{OC}, then these devices should all have similar values of V_{OC}. Instead, switching the donor material led to the most dramatic changes in V_{OC} with values ranging from 391 mV for pentacene to 649 mV for TiOPc. Although measurements of HOMO levels are limited in resolution and accuracy, more

overlap might also be expected in the V_{OC} values for tetracene and TiOPc if V_{OC} is mainly determined by the difference in energy between the HOMO of the donor and the LUMO of the acceptor (this will be discussed more in the next chapter).

It should be mentioned that, while all of the V_{OC} values reported here agree reasonably well with what has been previously reported for these donor / acceptor combinations [15, 18, 114], higher values for the J_{SC} have been reported for some of the heterojunctions. However, optimizing the thicknesses of each layer to maximize the interference effects and efficiency are outside the scope of this work. The focus of the present work is V_{OC}, so these devices should suffice for studying the relationship between V_{OC} and the heterojunction. Furthermore, the differences in J_{SC}, which are less than an order of magnitude, are not expected to be larger enough to significantly affect V_{OC} (see Equation 3.4).

Without even explicitly calculating the fitting parameters for the equivalent circuit model, such large shifts in the *J-V* curves must require significant changes in the parameters. Because of the large changes in V_{OC} with the donor material, the properties of the heterojunction materials and the heterojunction itself must be studied in more depth to understand the origin of V_{OC} in organic solar cells. The next chapter will look at a larger set of donors and acceptors, apply the equivalent circuit model, investigate trends in how the heterojunction materials change device parameters, and explore the origin of the V_{OC} in more detail.

3.6 Conclusions

Having reviewed the current theories regarding the operation of organic solar cells, the level of understanding appears to be at different stages of development for

different processes. The basic mechanism for the operation of organic solar cells is the absorption of a photon to create an exciton that is then efficiently dissociated at a donor / acceptor interface where the energetics favor an electron in the acceptor and a hole in the donor. The equivalent circuit model was shown to describe the behavior of the *J-V* characteristics of organic solar cells, though there is presently no way to derive the diode equations from basic principles in organics. Furthermore, the models that have been developed to explain the generation, diffusion, and dissociation of excitons in the organic layers of planar heterojunction devices have shown good agreement with experimental data.

However, the origin of V_{OC} has been the subject of much debate. Though some have suggested a critical role in the electrode work functions and built-in field in determining V_{OC}, pentacene / C_{60} devices with varying electrodes show major change in neither V_{OC} nor equivalent circuit parameters. Only changing the properties of the donor leads to a significant change in V_{OC}. Though many have speculated that V_{OC} is primarily related to the difference in energy between the HOMO of the donor and the LUMO of the acceptor, more experiments are needed to elucidate the origin of the V_{OC} and are pursued in the next chapter.

CHAPTER 4

ORIGIN OF THE OPEN-CIRCUIT VOLTAGE

4.1 Introduction

The previous chapter described and discussed the present understanding of physics in organic solar cells using pentacene / C_{60} devices as a model system. Models for the *J-V* characteristics and short-circuit current were presented that agreed fairly well with experimental results. While there is still room to develop the models in more depth, the results suggest there is a good basic understanding of many of the processes occurring in the devices. On the other hand, open-circuit voltage is usually explained by relating to a built-in field between the contacts or the difference in the HOMO of the donor and the LUMO of the acceptor. Results for bilayer heterojunction solar cells thus far have shown little effect of the work functions of the electrodes on the open-circuit voltage and a large change with different donor materials. To explore the physical processes governing the origin of the open-circuit voltage in more depth, four donor and three acceptor molecules will be studied in this chapter using the equivalent circuit model and exploring the temperature dependence of cell performance.

4.2 Studied Heterojunction Materials

The different donors and acceptors studied here are summarized in Figure 4.1, and their HOMO and LUMO energies are compiled in Figure 4.2. Each of the seven semiconductors has previously been demonstrated in organic solar cells although some of the 12 combinations of donor and acceptor have not been previously reported. These materials were chosen because they present a range of different HOMO energies for the

donors and LUMO energies for the acceptors, which are thought to be important in determining the open-circuit voltage. However, these energy levels should not be thought of as absolute values for the semiconductors as measured values can vary depending on the measurement technique, deposition conditions, substrate, and other factors. Though the HOMO-LUMO energies cannot be interpreted as absolute values, they at least suggest that there is variety in the electronic properties for the semiconductors under study.

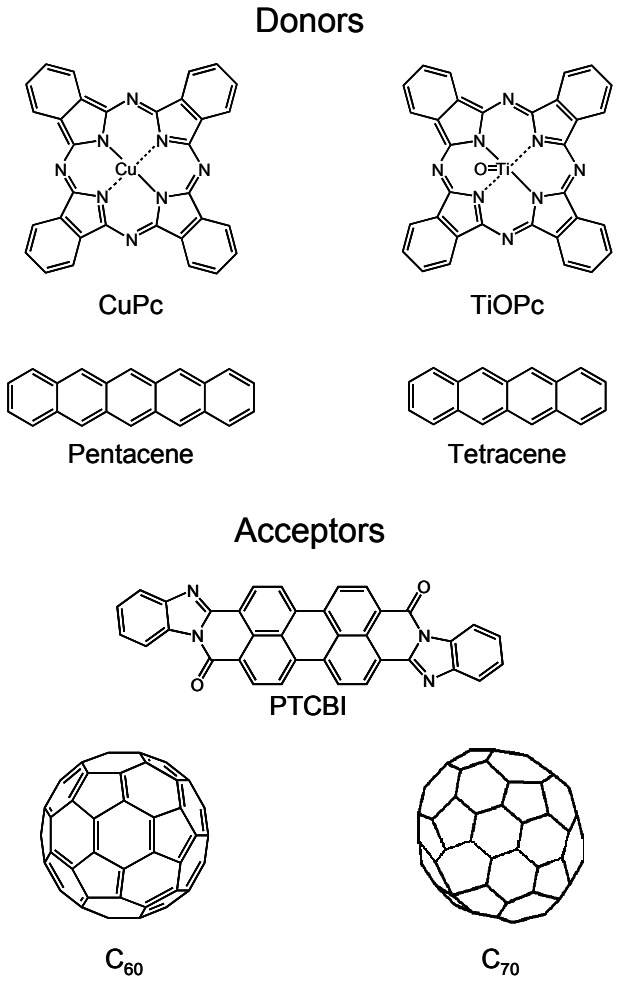

Figure 4.1. Chemical structures of donor and acceptor compounds for the study.

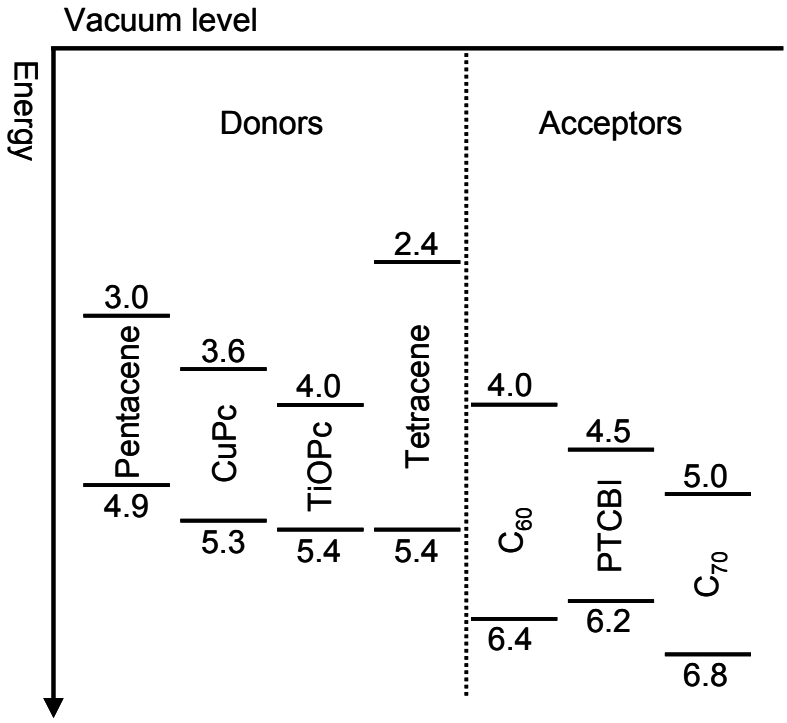

Figure 4.2. HOMO and LUMO levels from the literature for pentacene [16], CuPc [142], TiOPc [143], tetracene [18], C_{60} [114], PTCBI [54], and C_{70} [59].

The structure for the devices was ITO / donor / acceptor / BCP (8 nm) / Al. A constant layer thickness was not used for all of the donors and acceptors because of the varying exciton diffusion lengths in the materials. The thicknesses were 50 nm for pentacene, 20 nm for CuPc, 18 nm for TiOPc, 80 nm for tetracene, 45 nm for C_{60}, 25 nm for C_{70}, and 30 nm for PTCBI. Additionally, a thin layer of PEDOT:PSS was spin-coated onto the ITO before deposition of tetracene for all of the devices with tetracene as the donor. Without the PEDOT:PSS layer, the deposited tetracene layer was highly dispersive and devices had erratic *J-V* characteristics. Other details of the devices fabrication can be found in Section 2.2.

4.3 Open-Circuit Voltage of Different Heterojunctions

Initially, each of the heterojunctions was tested under a ~100 mW/cm^2 solar simulator inside a nitrogen-filled glovebox. Figure 4.3 shows the *J-V* characteristics in the dark and under illumination for one representative device for each heterojunction. The measurements were not corrected for spectral mismatch of the lamp with true AM1.5 G. Reproducible *J-V* curves could be obtained for all of the heterojunctions. While the fill factors for the TiOPc devices were relatively low, J_{SC} and V_{OC} values for the TiOPc / C_{60} devices did match well with what has been reported in literature [114]. All of the devices have *J-V* without any unexpected features, photocurrents within an order of magnitude, and good fill factors (except for the TiOPc devices). These characteristics suggest that these devices can serve as model devices for exploring the effect of the material properties on the open-circuit voltage.

The performance parameters for all of the heterojunctions are summarized in Table 4.1 grouped by the acceptor. Switching from C_{60} to C_{70} generally leads to a decrease in V_{OC}; however, the magnitude of the change varies with the donor, which does not follow the trend expected if V_{OC} is primarily determined by the difference between the HOMO of the donor and the LUMO of the acceptor, as predicted by Equation 3.1. While the V_{OC} of pentacene and CuPc decrease ~40 mV when changing from C_{60} to C_{70}, the V_{OC} of tetracene drops by only ~25 mV and that of TiOPc barely changes. While J_{SC} could also lead to changes in the V_{OC} (see Equation 3.4), the changes in J_{SC} are not large enough to lead to significant changes in V_{OC} since V_{OC} depends on the natural logarithm of the J_{SC}.

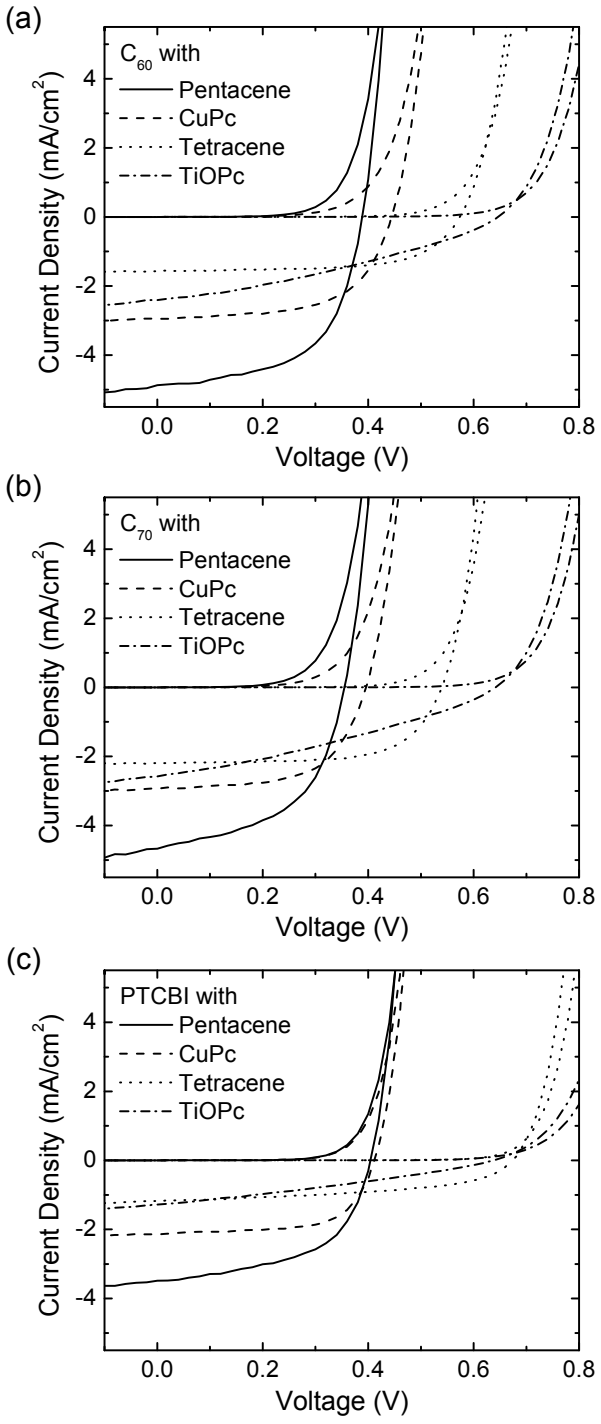

Figure 4.3. *J-V* characteristics in the dark and under illumination (Oriel 91160, ~100 mW/cm^2) with pentacene (solid), CuPc (dash), tetracene (dot), or TiOPc (dash dot) as the donor and (a) C_{60}, (b) C_{70}, or (c) PTCBI as the acceptor.

Table 4.1. Performance parameters of donor / acceptor solar cells averaged over three to five devices. The light source is an AM1.5 G solar simulator (91160, Oriel) with an irradiance of 100 mW/cm^2.

Acceptor	Donor	V_{OC} (mV)	$\|J_{SC}\|$ (mA/cm^2)	*FF*	η (%)
C_{60}	Pentacene	391 ± 3	5.0 ± 0.2	0.58 ± 0.01	1.1 ± 0.1
	CuPc	444 ± 1	2.9 ± 0.1	0.61 ± 0.01	0.78 ± 0.02
	Tetracene	569 ± 6	1.6 ± 0.1	0.58 ± 0.02	0.58 ± 0.02
	TiOPc	649 ± 7	2.4 ± 0.1	0.33 ± 0.02	0.52 ± 0.02
C_{70}	Pentacene	353 ± 4	4.6 ± 0.1	0.52 ± 0.01	0.85 ± 0.03
	CuPc	397 ± 2	2.9 ± 0.1	0.60 ± 0.01	0.71 ± 0.01
	Tetracene	544 ± 5	2.2 ± 0.1	0.67 ± 0.01	0.83 ± 0.04
	TiOPc	644 ± 7	2.6 ± 0.1	0.32 ± 0.01	0.56 ± 0.02
PTCBI	Pentacene	406 ± 2	3.5 ± 0.1	0.55 ± 0.01	0.79 ± 0.01
	CuPc	405 ± 5	2.1 ± 0.1	0.63 ± 0.02	0.54 ± 0.04
	Tetracene	672 ± 6	1.2 ± 0.1	0.50 ± 0.01	0.40 ± 0.02
	TiOPc	640 ± 3	1.3 ± 0.1	0.31 ± 0.01	0.26 ± 0.01

Comparing devices with C_{60} and PTCBI reinforces that the trend is not as clear as just the change in HOMO and LUMO values. Pentacene and TiOPc have only a small change in V_{OC} for C_{60} compared with PTCBI that is not likely to be statistically significant. In contrast, the V_{OC} of tetracene-based devices increases nearly 100 mV when changing from C_{60} to PTCBI while the V_{OC} of CuPc-based devices decreases by 40 mV. The inconsistency in how V_{OC} changes as the LUMO of acceptor is changed suggests that the relationship between the V_{OC} and materials is more complicated than just the difference between the HOMO of the donor and the LUMO of the acceptor. In particular, how the acceptor and donor molecules interact, especially at the heterojunction interface, may be of importance.

To probe in more depth what is changing in the solar cells as the donor and acceptor are varied, the equivalent circuit model can again be applied. By solving the *J-V*

equation for a solar cell (Equation 3.3) at open-circuit conditions, *i.e.*, $J = 0$ mA/cm^2, and assuming the devices are ideal enough to have negligible effects from $R_S A$ and $R_P A$, V_{OC} can be written as

$$V_{OC} \approx n\frac{kT}{e}\ln\left\{\frac{J_{SC}}{J_0}\right\}. \tag{4.1}$$

Equation 4.1 shows that V_{OC} is expected to be related to the ideality factor, short-circuit current density, and reverse saturation current density. As V_{OC} is related to the natural logarithm of J_{SC}, the small changes in J_{SC} here are not enough to account for large changes in the V_{OC} (with kT/e = 25.9 mV and assuming n = 1.5, a 20% change in J_{SC} should only result in a 7-9 mV change in V_{OC}). While values of n usually stay between 1.6 and 1.9 for organic solar cells, the largest variations are often observed in J_0. More information can be gathered on J_0 by studying the *J-V* characteristics as a function of temperature and is the focus of the next section. Temperature-dependent data can also provide general information on the charge transport mechanisms in a device because each transport mechanism responds to temperature changes differently.

4.4 Reverse Saturation Current in Organic Heterojunctions

4.4.1 Characteristics in the dark as a function of temperature

J-V characteristics in the dark for each of the heterojunctions were measured under vacuum in a cryostat from 120 K to 340 K in steps of 20 K to study J_0 and carrier transport. Figure 4.4 shows representative curves for two devices at some of the temperatures in the measured range. For all of the heterojunctions, good fit to the equivalent circuit model was hard to obtain below 260 K. However, the equivalent circuit model did generally agree well with the *J-V* characteristics above 260 K. The

heterojunctions in Figure 4.4 show the curves fitted to the equivalent circuit model at 120 K, 260 K, 300 K, and 340 K and two common deviations from the model that were observed at lower temperatures.

One common observation at low temperature that is not accounted for by the equivalent circuit model is that the current at forward bias does not follow a series resistance limited behavior as can be seen in the curves for a pentacene / C_{70} device in Figure 4.4(a). At low forward bias, all of the curves are fairly straight lines as predicted for a diode with exponential behavior in a semi-logarithmic graph. At high forward bias, the high current is expected to become limited by the series resistance, which imposes a linear behavior on current with voltage. However, the dependence at high bias and low temperature was more exponential than linear. Fitting with the equivalent circuit model at 120 K shows the difficulty in reproducing the experimental behavior at high bias with a resistance-limited current. Possible reasons for the unexpected current-voltage dependence include space-charge limited current because of the lower mobility or intrinsic carrier concentration in organic semiconductors at low temperatures and mobility with a field dependence that may change with temperature [134, 144].

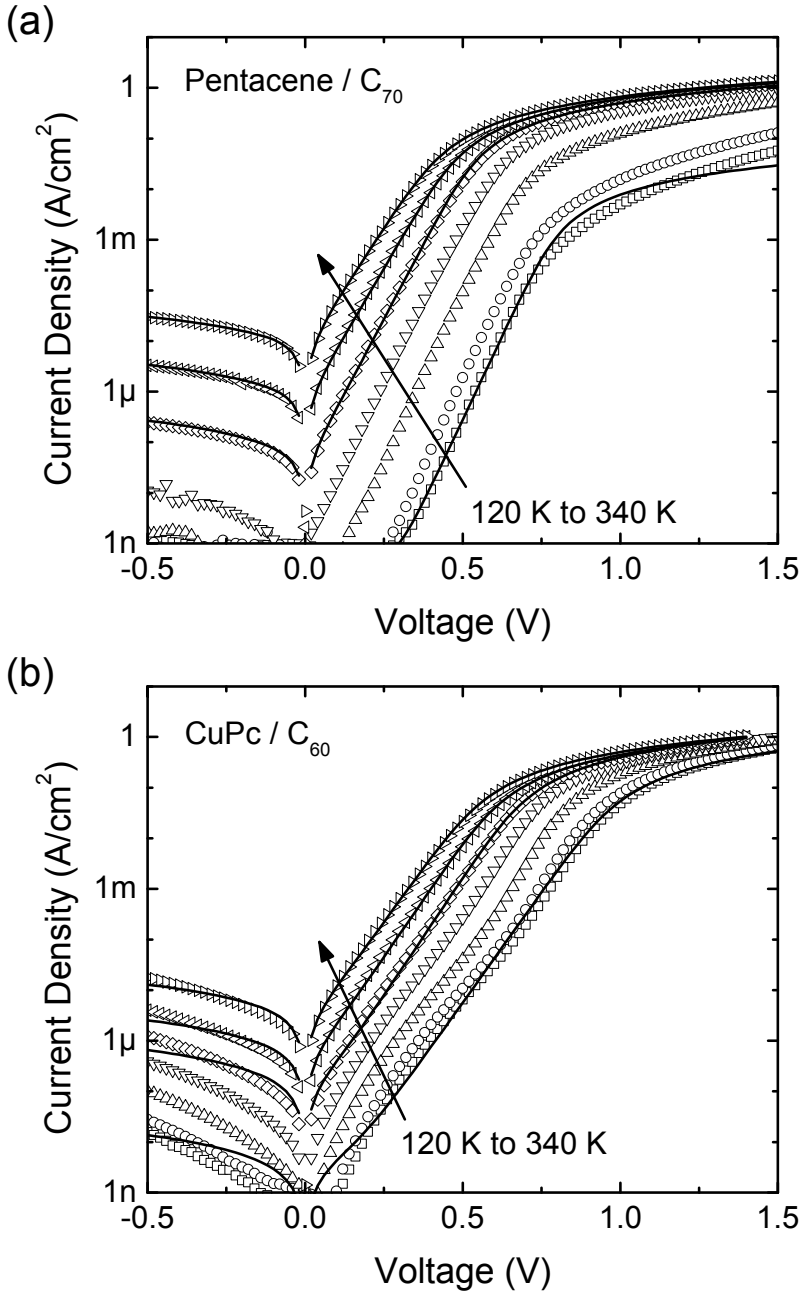

Figure 4.4. *J-V* characteristics for (a) pentacene / C_{70} and (b) CuPc / C_{60} heterojunctions under vacuum in a cryostat without illumination at 120 K, 140 K, 180 K, 220 K, 260 K, 300 K, and 340 K. Curves fitted to the equivalent circuit model are shown with solid lines.

Another non-ideal occurrence at low temperature was an additional hump in the *J-V* characteristics at low bias as shown for CuPc / C_{60} in Figure 4.4(b). A low parallel resistance can sometimes account for this type of behavior. In this case, the parallel resistance alone cannot model the hump because a similar magnitude of current would be expected in reverse bias, which is not observed. It is still not clear yet whether a two diode model, which has been applied to inorganic and organic solar cells, would fit the experimental data or if more modifications of the model are needed. Again, above 260 K, the extra feature in the curves becomes almost negligible and good agreement is obtained with the equivalent circuit model.

Extension of the equivalent circuit to model these additional features at lower temperature and further investigation into their origin could provide useful information for understanding more of the physical processes occurring in organic heterojunctions. However, these investigations are not the subject of the present study and will be explored in the future. Because of the good fit to the circuit model above 260 K, the data from 260 K to 340 K can be studied for trends in the circuit parameters that may help to explain the origin of J_0. It should be noted that similar deviations can be found in other papers reporting the temperature-dependent *J-V* characteristics of organic solar cells [108], though deviations from the model were not mentioned. While the equivalent circuit model was still used in that report at low temperatures, using a model at temperatures where clear features appear in the experimental data that the model cannot explain does not seem prudent and will be not be done here.

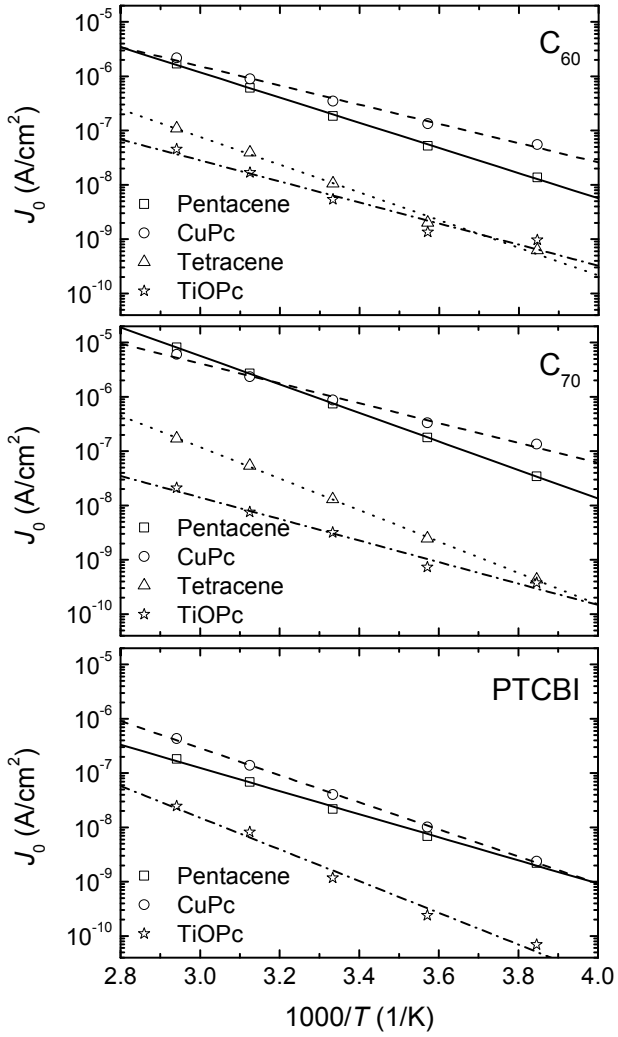

Figure 4.5. J_0 values extracted by fitting the equivalent circuit model to the *J-V* characteristics in the dark of different heterojunctions from 260 K to 340 K. Lines indicate fitted values according to Equation 4.2.

Looking only at the temperatures where the equivalent circuit model holds (260 K to 340 K), Figure 4.5 summarizes the J_0 values extracted for each of the heterojunctions at the different temperatures. The tetracene / PTCBI devices are excluded because this is the one heterojunction for which good agreement with the circuit model was not found. A large variation of about three orders of magnitude among all of the different heterojunctions at 300 K can be seen for J_0. The tetracene and TiOPc devices tended to

have the highest V_{OC} and also do have the lowest J_0. Pentacene and CuPc have both V_{OC} and J_0 that tend to be closer in value. However, both the J_0 and V_{OC} of the CuPc devices with C_{60} and PTCBI are slightly higher than pentacene. In these cases, a slightly larger n is responsible for the higher V_{OC}. Therefore, the nature of n in organic solar cells will need to be studied more in the future.

Comparing the J-V characteristics and dependence of J_0 on temperature with the forms of known current mechanisms such as Schottky emission, Frenkel-Poole emission, and field emission [145], the reverse saturation current density best fits a thermally activated process with the form

$$J_0 = J_{00} \exp\left(\frac{-\phi_B}{kT}\right), \tag{4.2}$$

where ϕ_B is the effective barrier and J_{00} is a prefactor. This is similar to the equation for Schottky emission

$$J_0 = A^{**} T^2 \exp\left(\frac{-\phi_B}{kT}\right), \tag{4.3}$$

where A^{**} is an effective Richardson's constant [146]; however, there is not sufficient evidence to justify the inclusion of the T^2 term as it does not affect the agreement to the experimental data over this temperature range. Relationships similar to Equation 4.2 are often observed in thin-film inorganic solar cells [147, 148, 149]. In the inorganic devices, J_0 and ϕ_B are often found to be primarily determined by a distribution of states in the absorber layer, with the band gap of the window layer doing little to change the barrier height [148, 149].

Table 4.2. Parameters related to J_0 for different heterojunctions calculated by fitting Equation 4.2 to the data in Figure 4.5 along with the V_{OC} of the individual devices.

Acceptor	Donor	V_{OC} (mV)	J_{00} (mA/cm^2)	ϕ_B (eV)
C_{60}	Pentacene	391	10,800	0.46
	CuPc	444	311	0.35
	Tetracene	574	3,410	0.51
	TiOPc	641	18	0.39
C_{70}	Pentacene	351	440,000	0.52
	CuPc	394	1,270	0.36
	Tetracene	544	58,500	0.58
	TiOPc	641	12	0.39
PTCBI	Pentacene	406	305	0.42
	CuPc	408	905	0.50
	Tetracene	665	-	-
	TiOPc	640	8,790	0.58

Table 4.2 lists the parameters extracted by fitting Equation 4.2 to the data in Figure 4.5. Unlike for inorganic cells, ϕ_B in these organic heterojunctions often varies regardless of which layer is changed instead of being primarily determined by only one of the layers. This may not be too surprising as both layers in organic solar cells are of similar thickness while the window layer is often significantly thinner than the absorber in inorganic thin-film solar cells. Because of the dependence of ϕ_B on both layers, the reverse saturation current is thought to be closely related to interactions between donor and acceptor molecules at the heterojunction interface. However, exactly what determines ϕ_B is still not clear. The barrier could potentially be related to the energy gap between the HOMO of the donor and the LUMO of the acceptor ΔE_{HL} by a factor *n'* to yield

$$J_0 = J_{00} \exp\left(\frac{-\phi_B}{kT}\right) = J_{00} \exp\left(\frac{-\Delta E_{HL}}{n'kT}\right). \quad (4.4)$$

The variation of ϕ_B from ΔE_{HL} could be related to effects such as vacuum level misalignments at the heterojunction caused by energy level bending and interface dipoles and the formation of charge-transfer states [150]. More investigations are needed to understand the true nature of ϕ_B.

Variations in J_{00} of several orders of magnitude mean that J_{00} also plays an important role in determining J_0. For many of the donors, J_{00} is higher with C_{70} compared to C_{60}. TiOPc shows a different trend with a J_{00} that only increases significantly when PTCBI is used as the acceptor. Variations in J_{00} suggest that properties of both materials affect the final value.

4.4.2 Explanation for reverse saturation current

Variations in the parameters determining J_0 when either the donor or acceptor layer is changed suggest that the interaction between the donor and acceptor molecules is important in determining J_0. Because the reverse saturation current appears to be thermally activated, one possible explanation for this current in reverse bias would be the thermal excitation at the donor / acceptor heterojunction through a reaction of the type $D + \underline{A} \rightarrow D^+ + A^-$, where D and A refer to the donor and acceptor, respectively, in which an electron gets transferred from the HOMO of a donor molecule to the LUMO of an acceptor molecule. Conversely, the current forward bias would be the result of recombination at the interface, $D^+ + A^- \rightarrow D + \underline{A}$.

From theoretical chemistry, the rate for the reaction $D + \underline{A} \rightarrow D^+ + A^-$ can be described at the molecular level by a semiclassical Marcus theory expression

$$k_{et} = \frac{2\pi}{\hbar}\left|V_{if}\right|^2 \sqrt{\frac{1}{4\pi\Lambda kT}} \exp\left(-\frac{(\Delta G_0 + \Lambda)^2}{4\Lambda kT}\right), \tag{4.5}$$

where Λ is the reorganization energy induced by the electron transfer, ΔG_0 is the variation of the Gibbs free energy during the reaction, and V_{if} is the electronic coupling matrix element [151]. The steady-state reverse saturation current density can then be written as

$$J_0 = ek_{\text{et}}N_{\text{CT}}, \tag{4.6}$$

where e is the elementary charge and N_{CT} is the surface density of interacting donor and acceptor pairs that can be thermally excited with a rate k_{et} given by Equation 4.5. Combining Equations 4.2, 4.5, and 4.6, the pre-factor J_{00} can also be expressed as

$$J_{00} = eN_{\text{CT}}\frac{2\pi}{\hbar}\left|V_{if}\right|^2\sqrt{\frac{1}{4\pi\Lambda kT}}, \tag{4.7}$$

and the thermal activation barrier ϕ_B in Equation 4.2 can be correlated with $(\Delta G_0 + \Lambda)^2/4\Lambda$ in the argument of the exponential term in the Marcus expression in Equation 4.5.

The energy barrier ϕ_B presented by the heterojunction has already been shown to impact the reverse saturation current density and may be strongly influenced by the molecular energy levels of the donor and acceptor molecules that form the organic heterojunction. However, Equation 4.7 illustrates that the electronic coupling and reorganization energy are equally important in influencing the reverse saturation current. Hence, great consideration must be given to molecular shape, geometry, charge densities, relaxation due to vibrational modes, and packing when designing new donor and acceptor molecules. The energetics and electronic coupling between donor and acceptor molecules will simultaneously impact the short-circuit current and the open-circuit voltage. To maximize exciton dissociation, large energy level offsets and a strong electronic coupling are desirable for charge transfer reactions of the type $D^* + A \rightarrow D^+ + A^-$ or $D + A^* \rightarrow D^+$

+ A^- that involve molecules or polymers in the excited state, where D^* and A^* indicate an excited donor or acceptor. To achieve large open-circuit voltages, large values for ϕ_B and a weak electronic coupling between the donor and acceptor materials is expected to be required to minimize the charge transfer reactions of the type $D + A \rightarrow D^+ + A^-$. This analysis gives insight into one way that the reverse saturation current in organic devices might be related back to the molecular properties.

4.5 Temperature Dependence of Characteristics under Illumination

The performance characteristics of the heterojunctions were also measured as a function of temperature under illumination (Oriel 66902, ~100 mW/cm^2). *J-V* characteristics were measured at 120 K, 180 K, 240 K, 300 K, and 340 K to give a wide range of temperatures and include temperatures where deviations from the equivalent circuit model are known to exist. Figure 4.6 depicts typical *J-V* curves observed for some of the heterojunctions, and Figure 4.7 summarizes V_{OC}, J_{SC}, and FF for several of the heterojunctions as a function of temperature. While there are several general trends in the change in performance with temperature, the trends do not always hold for all of the tested heterojunctions. In all cases, V_{OC} increased with decreasing temperature.

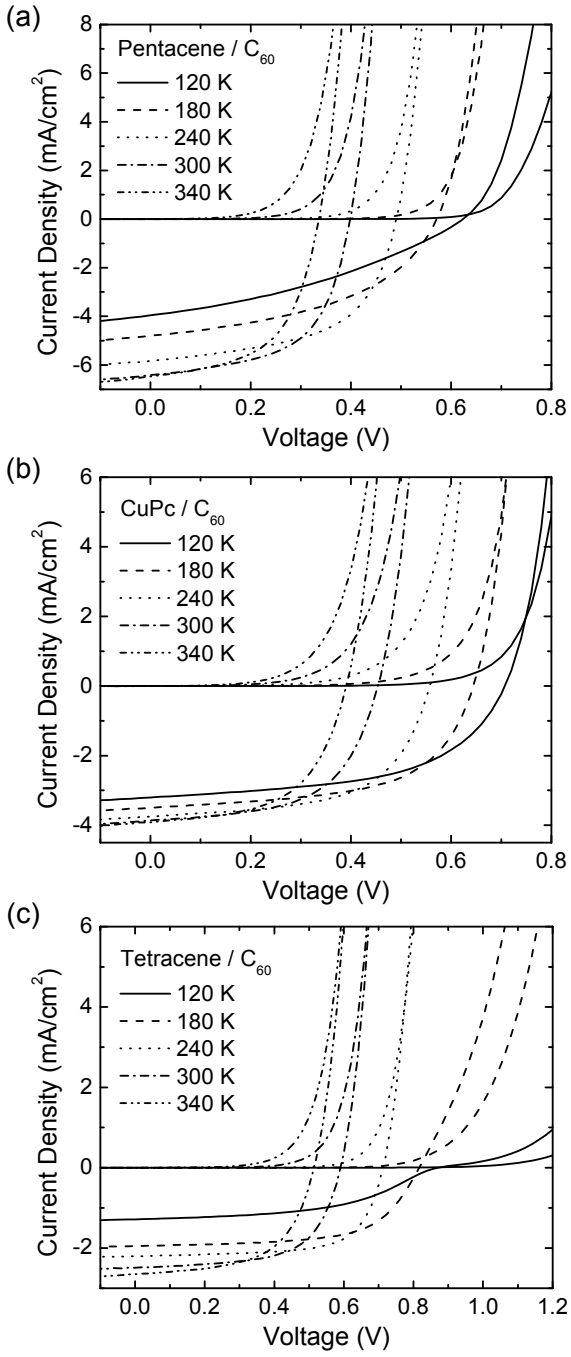

Figure 4.6. *J-V* characteristics in the dark and under illumination (66902, ~100 mW/cm^2) for (a) pentacene / C_{60}, (b) CuPc / C_{60}, and (c) tetracene / C_{60} heterojunctions at 120 K (solid), 180 K (dash), 240 K (dot), 300 K (dash dot), and 340 K (dash dot dot).

As shown in Figure 4.6(a) for pentacene / C_{60}, several of the heterojunctions had a strong dependence of short-circuit current density on temperature. The primary cause of the strong temperature dependence is not certain, but possible reasons include a decrease in exciton diffusion length or charge mobility with temperature, a thermal component to exciton dissociation, or changes in absorption with temperature. EQE measurements at different temperature could be combined with the previously presented EQE model (see Section 3.4.1) to begin to explain the processes leading to the strong temperature dependence. Fill factor also changes significantly with decreasing temperature. The change in fill factor may also be related to changes in charge mobility or additional barriers at the contacts that become important at low temperatures.

However, not all of the organic heterojunctions have the same behavior as pentacene / C_{60}. Unlike pentacene / C_{60}, the CuPc / C_{60} devices in Figure 4.6(b) have a much weaker dependence of both J_{SC} and FF on temperature. Possible reasons for the different behavior include differences in the temperature dependent effects of the properties listed previously for pentacene such as mobility [152, 153], exciton diffusion length, exciton dissociation, and absorption. However, the temperature dependence of J_{SC} and FF are much stronger when CuPc is combined with PTCBI, as shown in Figure 4.7. This reinforces that understanding the properties of both the donor and acceptor is essential to forming a complete picture of what determines photovoltaic performance.

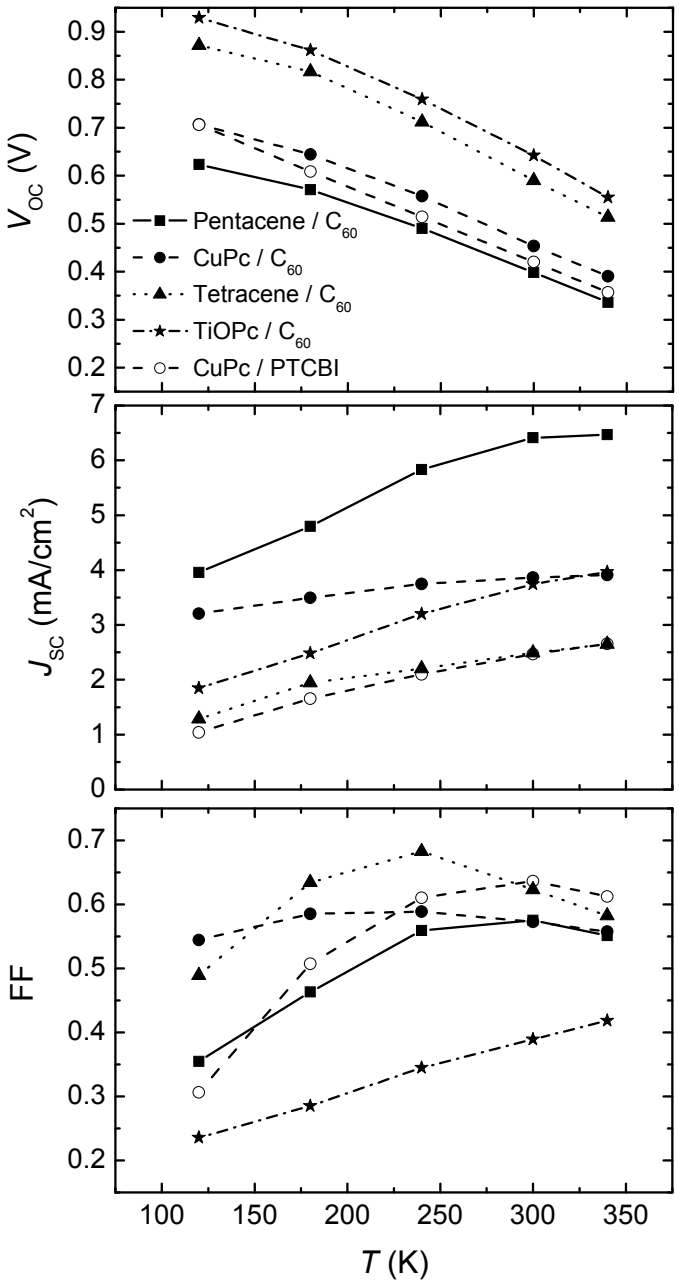

Figure 4.7. V_{OC}, J_{SC}, and FF as a function of temperature for heterojunctions of pentacene / C_{60} (squares), CuPc / C_{60} (filled circles), tetracene / C_{60} (triangles), TiOPc / C_{60} (stars), and CuPc / PTCBI (empty circles). Lines are merely guides for the eye.

At 120 K, the tetracene / C_{60} devices exhibit a kink in the *J-V* curves under illumination, which was also observed in the tetracene / C_{70} devices, as shown in Figure 4.6(c). Similar behaviors are often seen in CdTe and CIS thin film solar cells and are usually attributed to a barrier at one of the contacts [148, 154]. However, some differences appear to exist between the kink in organic and inorganic devices. Primarily, the *J-V* curves remain fairly flat after the kink in most archetypical curves shown for inorganic devices whereas the *J-V* curves in the organic devices return to an exponential behavior after the kink. Kinks have also been observed at room temperature in organic devices [155, 156, 157], though low temperature was needed to see the kink in tetracene / C_{60}. The kink here is thought to be related to a barrier at either the ITO / PEDOT:PSS or PEDOT:PSS / tetracene interface that becomes significant only at low temperatures.

General trends in the temperature-dependent performance can be seen in Figure 4.7. For all organic devices, V_{OC} increases as temperature decreases, which would be expected because J_0 also decreases with temperature. For many organic devices, J_{SC} is a strong function of temperature, increasing over 50% from 120 K to 340 K in many cases. However, some heterojunctions, such as CuPc / C_{60}, have a weaker dependence on temperature. Finally, fill factor is seen to be a complicated function of temperature that does not necessarily vary monotonically.

4.6 Comparison with Inorganic Devices

The temperature-dependent data presented here can give some insight into how the physics of organic devices compares with that of inorganic solar cells. For both crystalline and thin-film inorganic solar cells, FF generally increases and J_{SC} often only slightly decreases with decreasing temperature [147, 158, 159, 160]. This type of

behavior is in contrast to organic devices where FF was observed to both increase and decrease with decreasing temperature and J_{SC} was a relatively strong function of the temperature. However, V_{OC} does follow the same trend of increasing with lower temperatures in organic and inorganic devices.

There are several differences in the physics of organic and inorganic semiconductors that require that their electrical properties be treated differently. Of course, one major difference is the generation of excitons instead of free carriers when photons are absorbed. The additional processes of exciton diffusion and dissociation must be considered in organic solar cells and do not follow the same behavior as free carriers. Furthermore, the existence of singlet and triplet excitons and recent studies suggesting the fission of a singlet exciton into two spin-triplet excitons indicate that there is still more to learn about the behavior of excitons [161].

Another major difference is the transport of charge carriers in inorganic and organic semiconductors. The weakness of electronic couplings, large electron-vibration couplings, and disorder effects in organic semiconductors result in localized charge carriers that move by hopping [106]. Thus, the charge carriers in organics have low mobility values (reaching ~1 $cm^2\ V^{-1}\ s^{-1}$ in highly order materials) that increase with temperature. This is in contrast to crystalline semiconductors with high mobilities that decrease with increasing temperature [145]. However, it may be possible to draw more parallels with some of the inorganic thin-film materials that also have lower mobilities that decreases with temperature [147].

Though some similarities with the behavior of inorganic thin-film solar cells do exist, there are still several differences. For example, both the donor and acceptor in an

organic device play a role in absorbing light and contributing current, and decreasing the band gap can often increase the open-circuit voltage. Furthermore, while intrinsic carrier concentration is an important parameter in inorganic semiconductors and dependent on band gap, the intrinsic carrier concentration is low in organic semiconductors [134], and how applicable the concept even is to pure, undoped organic semiconductors with their different band structure and charge localization is not clear. Finally, the active semiconductor layers of organic solar cells are often a total of 100 nm whereas inorganic cells tend to be on the order of a micron. The thinner layers could lead to additional effects that are not observed in thicker films. Though there are many similarities between inorganic and organic solar cells, each technology has its own unique processes to unravel to completely understand the device physics.

4.7 Conclusions

The open-circuit voltage of organic heterojunctions was found to not be solely determined by the HOMO level of the donor and the LUMO level of the acceptor because switching the acceptor material did not always lead to consistent changes in V_{OC} for various donors. Using the equivalent circuit model, V_{OC} is known to be largely related to the reverse saturation current. To better understand the origin of J_0, temperature dependent studies of J_0 were performed on the various heterojunctions. At temperatures above 260 K, devices were found to operate in accordance to the equivalent circuit model, and J_0 follows a thermally activated behavior. Both the effective barrier and the prefactor in the thermally activated process can change significantly as the donor and acceptor materials are varied.

The thermally activated process dependent on the two compounds forming the heterojunction suggests that the heterojunction interface itself may be important in determining J_0. Parallels can be found between the behavior of the reverse saturation current and the theoretical charge transfer rate between organic molecules from semiclassical Marcus theory. The energy of the reaction and the electronic coupling of the molecules affecting charge transfer rates could be analogs for the effective barrier and the prefactor determining J_0. These parallels suggest that both the energy levels and the electronic coupling of the molecules forming a heterojunction must be considered to design organic solar cells with low J_0 and high V_{OC}.

Additional behaviors were found as temperature was lowered such as a large change in J_{SC}, decreasing FF, and deviations from the equivalent circuit model. Some of these changes may be related to different mechanisms of charge transport in organic semiconductors, the reliance on excitons, which are generally avoided in inorganics, and exciton dissociation, and other unique properties of organic materials that may not be found in inorganic semiconductors. Progress is being made in clarifying the physics behind the operation of organic solar cells and electronics, but many questions still remain to be answered.

CHAPTER 5

AREA SCALING

5.1 Introduction

While the previous chapter focused on understanding the physics of organic solar cells, this chapter shifts focus to the applications related problem of increasing area in solar cells. Reviews of the literature show that the majority of devices being reported are on the scale of 0.1 cm^2, as supported by Table 1.1. Even the cells with the highest reported efficiencies and an area of 0.1 cm^2 would still produce less than 1 mW, hardly enough power for many applications. While multiple small devices could be connected in series or parallel to produce large amounts of energy, the additional complexity and space requirements of the interconnections and the need for devices with well-matched characteristics would be a major obstacle for such small devices. Instead, devices with a large area must also be pursued. This chapter discusses the main challenges of increasing the area of organic solar cells, proposes a metal-grid architecture, which is independent of the organic active layers, for improving large-area cell performance, and demonstrates and compares the performance of large-area organic solar cells with and without the grid. In particular, cells with areas of 0.11 cm^2, 7 cm^2, and 36.4 cm^2 will be studied to cover a wide range of areas.

5.2 Challenges of Area Scaling

5.2.1 Series resistance power loss

While much attention has been given to trying to increase power conversion efficiency in organic solar cells, reports dealing with how efficiency scales with device

area are relatively scarce [162, 163]. Because solar cells, like all electronic devices, exhibit series resistances that can never be completely avoided, some generated power will be lost by dissipation through the internal resistance of the device. Therefore, another important quantity to consider in the optimization of the efficiency of a cell is the total resistive power loss per unit area P_R which is given by

$$P_R = \frac{R_S I_{max}^2}{A} = \frac{R_S (J_{max} A)^2}{A} = R_S A J_{max}^2, \tag{5.1}$$

where I_{max} and J_{max} are the current and current-density at the maximum power point, R_S is the series resistance in the device, and A is the area of the device. Equation 5.1 clearly illustrates that the resistive power loss per unit area is proportional to the series resistance ($R_S A$) and that consequently the effects of parasitic series resistance are likely to play a more prominent role as the area of the cell is increased.

The resistive power loss density depends on the resistivities of the electrodes and the organic semiconductors and the contacts between film interfaces. The loss can be represented by the sum

$$P_R = P_{ITO} + P_{organic} + P_{contacts} + P_{Al}, \tag{5.2}$$

where P_{ITO} and $P_{organic}$ are the resistive power loss densities of the ITO and organic semiconductors, respectively. $P_{contacts}$ include all the interfacial contact power loss densities between films, such as metal-organic and organic-organic interfaces. P_{Al} is the resistive power loss of the metal electrode, which is aluminum in this case.

Looking at the device in Figure 5.1, the contributions from the organic layers and contact resistances are not expected to vary with device area since current flows through these resistances in the z-direction and should only change with the thickness of the device. However, resistance from the electrodes will increase with area since increasing

the active area makes the photogenerated current travel a longer distance before it is collected at the external electrodes. Specifically, the position of the contacts in the device here causes current to flow primarily in the *x*-direction, so resistance and power loss density should depend only on length *L* and not width *W*.

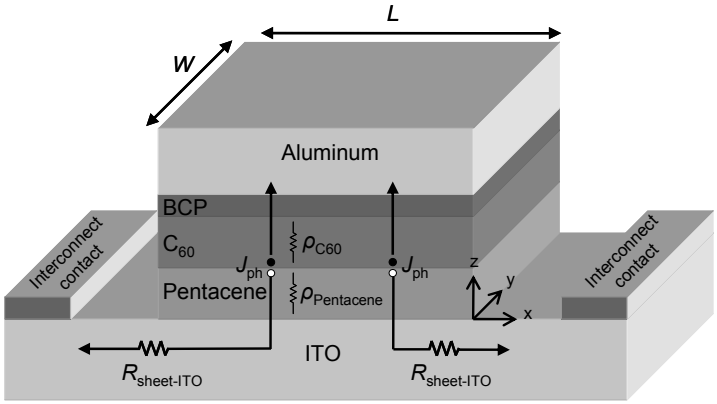

Figure 5.1. Three-dimensional schematic of typical solar cell architecture indicating sources of resistance.

Because the organic and interfacial power loss densities are independent of area and the aluminum has a high conductivity relative to ITO, only contributions of the ITO to power loss will be considered for now. For the device structure in Figure 5.1, the power loss density of the ITO layer (P_{ITO}) is given by [164]

$$P_{ITO} = \frac{1}{\alpha} J_{max}{}^{2} L^{2} R_{sheet-ITO} \tag{5.3}$$

where $R_{sheet\text{-}ITO}$ is the sheet resistance of the ITO in Ω/sq., L is the length of the solar cell, and α is determined by the number of interconnect contacts. For example, α is 3 when only one of the interconnect contacts is used whereas it is 12 when both contacts are used.

The series resistance of the ITO layer can be estimated by dividing the power loss of Equation 5.3 by J_{max}^2 (see Equation 5.1) to give

$$R_S A = \frac{1}{\alpha} L^2 R_{sheet-ITO}. \tag{5.4}$$

It should be noted that Equation 5.4 is only an estimate for the series resistance from the ITO. For a more accurate calculation relative to equivalent circuit parameters, finite element analysis based on many small solar cells connected in parallel could be used.

The equivalent circuit model from inorganic solar cells (see Section 3.3.2), which has already been shown to work well for describing many organic solar cells, can be used to understand in detail how $R_S A$ affects performance and what other changes may be expected as area increases. The parameters for the equivalent circuit model are n, J_0, J_{ph}, $R_P A$, and $R_S A$. Considering the device in Figure 5.1, n, J_0, J_{ph}, and $R_P A$ are primarily related to the junction in the z-direction and not the area in the x-y plane. While the values may change because of uniformity, edge effects, or other non-idealities, the values are not expected to be a strong function of the area.

From Equation 5.4 and a sheet resistance of 15 Ω/sq. for ITO, resistive power losses in ITO for devices with a square geometry and lengths of 1 cm, 5 cm, and 10 cm would correspond to $R_S A$ values of 1.25 Ωcm^2, 31.3 Ωcm^2, and 125 Ωcm^2. Using this range of values as an estimate for $R_S A$ in the equivalent circuit model, Figure 5.2 shows the effect that the increased series resistance will have on the performance of a device using typical parameters for a pentacene / C_{60} solar cell. Such large changes in $R_S A$ cause significant reduction in FF, J_{SC}, and η. Therefore, methods for reducing the contribution of ITO to the $R_S A$ must be developed to realize large-area organic solar cells.

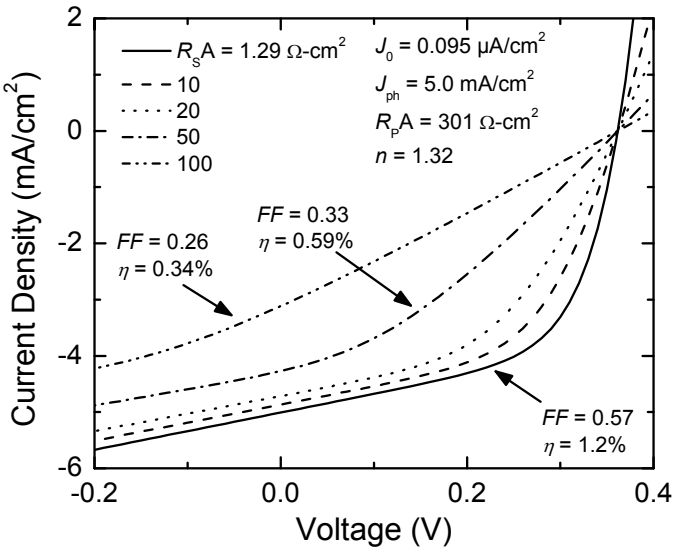

Figure 5.2. Expected effect of series resistance (R_SA) on organic photovoltaic performance.

5.2.2 Current strategies in organics

Presently, two main strategies are being pursued for dealing with the resistance of the transparent electrode in large-area organic solar cells: stripe geometries [51, 96] and metal grids [165, 166, 167, 168]. Both strategies were originally developed for inorganic solar cells and are being adopted with modifications that are required because of some unique differences with organic solar cells.

A basic schematic of a cross section through the stripe geometry is depicted in Figure 5.3. The stripe geometry limits the increase in series resistance from the transparent electrode by keeping the length of individual cells short and increasing the width, which should not affect R_SA according to Equation 5.4. Several individual cells can be connected in series to create a module with an overall longer length. As a result of the series connections, V_{OC} is also increased; however, photocurrent will be limited by the

device with the lowest photocurrent and overall performance will be significantly affected by one bad or shadowed cell [169].

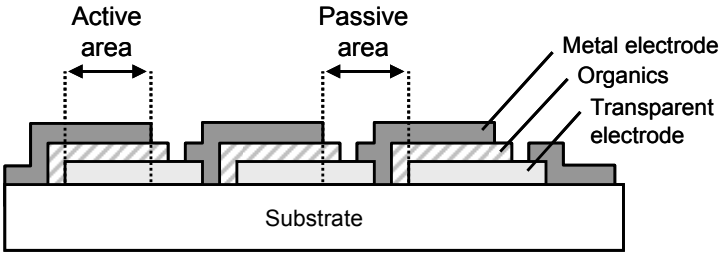

Figure 5.3. Schematic of a cross section through the stripe geometry.

The biggest drawback to the stripe geometry is that active area must be conceded to make space for the connections between individual devices, resulting in a lower use of the overall area. While shorter cell lengths are better for lower series resistance, the overhead required for cell connections limits the minimum length of the cells to maintain a high fraction of active area over the entire surface. Recent results for stripe devices required 2 mm gaps between cells with a length of 13 mm yielding a loss of more than 13% of the surface area [51].

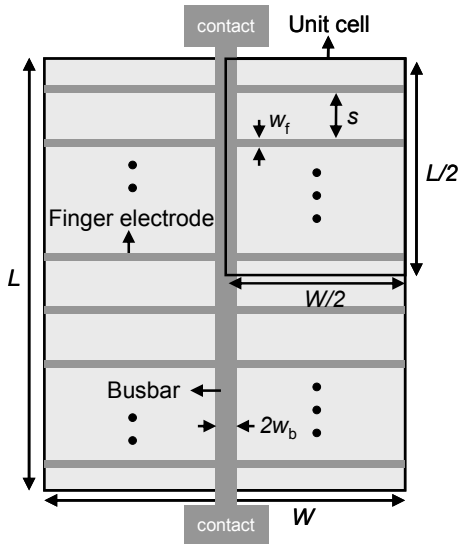

Figure 5.4. Schematic of large-area solar cell with a grid. The unit cell is defined such that the total photogenerated current leaves the unit cell only through the busbar and no photogenerated current flows across any of the unit cell edges.

Another way to decrease the overall resistance of the transparent electrode is by fabricating metal grids on top of the transparent electrode that can provide an alternative, low-resistance pathway for current. The metallic grids consist of finger electrodes branching out from a busbar electrode as shown in Figure 5.4. Photogenerated current travels through the transparent electrode, gets collected by the nearest finger electrode, and then is delivered into the busbar electrode which is connected directly to the external leads. The key is to have a grid with high conductivity through proper choice of metal and the thicknesses and widths of the fingers and busbar. Though some active area is lost because of shadowing from the opaque grid, the shadowing losses of grids can be kept lower than the area losses demonstrated so far in stripe geometries.

Similar grids have been demonstrated with a PEDOT:PSS film as the anode in an attempt to develop a transparent anode that is a cheaper alternative to ITO [165, 166, 167, 168]. While the PEDOT:PSS alone can act as a transparent anode, a grid was needed to

lower the series resistance because PEDOT:PSS has a significantly higher resistance relative to ITO. However, the grids in the previous research are still generally too thin (tens of nanometers) and resistive to maintain device performance in large-area solar cells and are only sufficient in bringing the sheet resistive down to that similar of ITO; thus, they would suffer the same limitations discussed in Section 5.2.1.

Another novel approach is to insert connections from a top transparent electrode through via holes to a backside metallic electrode [170]. However, the thin grids and via-hole connections of this approach generally suffer from resistances that are still too high and limit the current in large-area cells.

In this research, a thick grid will be applied to maintain a low effective resistance of the ITO even as the area of the solar cell becomes large. This approach could also be applied to other, cheaper transparent electrodes that are not ITO in the future.

5.2.3 Difference from inorganics

Metal grids are also used in conventional silicon solar cells, but there are several important differences in the implementation with organic solar cells. In silicon solar cells, the grids are placed on top of the n-type semiconductor as a cathode. The grid can be placed on top because no transparent electrode covering the entire area is needed since the n-type semiconductor is sufficiently conducting in the plane of the device to act as a moderately resistive cathode. Since the silicon wafer is between the metal grid and the anode, which coats the back of the wafer, both electrodes are well isolated.

Considering Figure 5.5, the grid for an organic device must be fabricated directly on top of the ITO with the organic layers and metal electrode subsequently deposited. Additional passivation is therefore needed on top of the metal grid because the thin

organic layers (100 nm) might not adequately coat the thick metal grid (5 μm) to isolate the grid from the metal electrode. This is in contrast to inorganic cells where the grid can be fabricated on top of the active layers.

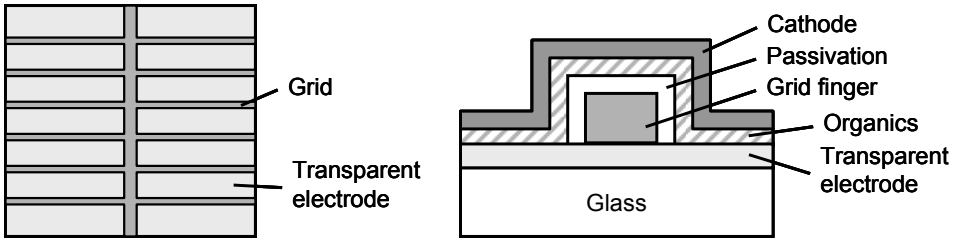

Figure 5.5. Schematic of basic grid design and cross section through grid finger for a complete device.

An alternative would be to switch the metal and transparent electrodes so that the smooth, high conductivity, metal electrode is between the organic layers and the substrate and the transparent electrode is on top of the organic layers. A grid would still be necessary on top of the transparent electrode to reduce the overall resistance but would no longer risk shorting with the metal electrode. However, fabrication of a metal grid on organic layers would be difficult because organics are generally very sensitive to chemical and high temperature (above 150 °C) processing. A fine grid, to minimize shadowing, with thick metal, to maximize conductivity, would also be hard to achieve with low-temperature vacuum evaporation.

5.3 Electrode Design

To evaluate the grid design before fabrication, we again turn to the power loss density analysis to estimate the series resistance throughout the solar cell. In addition to the resistive power losses of the ITO and organic semiconductors, the metal grid structure

introduces additional power losses such as contact loss between the ITO and the grid, resistive power losses from the grid itself, and a shadow power loss. The shadow power loss is associated with shadow areas which are created by the metal grid blocking incoming sunlight. As with the devices without a grid, the total resistive power loss density can be written as a sum of power loss densities for a device with a grid as

$$P_{\mathrm{R}}^{\mathrm{grid}} = P_{\mathrm{ITO}}^{\mathrm{grid}} + P_{\mathrm{organic}} + P_{\mathrm{contacts}} + P_{\mathrm{Al}} + P_{\mathrm{finger}} + P_{\mathrm{busbar}}, \tag{5.5}$$

where $P_{\mathrm{ITO}}^{\mathrm{grid}}$ is the power loss density from the ITO when a grid is present, and P_{finger} and P_{busbar} are the power densities dissipated in the fingers and busbars of the grid, respectively. The contribution from the metal electrode will be neglected because of its high conductivity.

Power loss densities of a solar cell with an integrated metal grid can be calculated based on the unit cell concept [171] The unit cell is defined such that the total photogenerated current leaves the unit cell only through the busbar and no photogenerated current flows across any of the unit cell edges. The individual power loss calculations for each component of the unit cell are well explained elsewhere [1, 171] and the corresponding series resistance equations calculated from the power loss densities using Equation 5.1 are summarized in Table 5.1 for a grid with the geometry shown in Figure 5.4, where $R_{\mathrm{sheet\text{-}ITO}}$ is the sheet resistance of the ITO in Ω/sq., s is the space between finger electrodes, ρ_{Cu} and t_{g} are the resistivity of the grid metal (copper in this case) and grid thickness, respectively, r_{specific} is the specific contact resistance in $\Omega\mathrm{cm}^2$ between the ITO and the grids, ρ_{p} and ρ_{C60} are the resistivity of the pentacene and C_{60}, respectively, t_{p} and t_{C60} are the film thicknesses of the pentacene and C_{60}, respectively,

and w_f and w_b are the width of the finger electrodes and busbar electrode, respectively. The total series resistance is estimated by adding all of the series resistances in Table 5.1.

Table 5.1. Contributions to $R_S A$ for the unit cell in a solar cell with metal grids. P_{shadow} is the shadow power loss density.

Contributor	$\boldsymbol{R_S A}$ **(Ωcm^2)**	**Contributor**	$\boldsymbol{R_S A}$ **(Ωcm^2)**
ITO	$\frac{1}{12} R_{\text{sheet-ITO}} s^2$	Contact	$r_{\text{specific}} \frac{s}{w_f}$
Finger electrode	$\frac{1}{12} W^2 \frac{\rho_{Cu}}{t_g} \frac{s}{w_f}$	Organic layers	$(t_p \rho_p + t_{C60} \rho_{C60})$
Busbar	$\frac{1}{24} L^2 W \frac{\rho_{Cu}}{t_g} \frac{1}{w_b}$	P_{shadow} (mW/cm^2)	$J_{max} \cdot V_{max} \left(\frac{w_f}{s} + 2 \frac{w_b}{W} \right)$

One key change with the grid is that the ITO contribution is now related to the spacing between the fingers instead of the length of the device. As long as the spacing between fingers is kept small, the contribution from the ITO will remain small regardless of the area of the device. Only the contributions from the finger electrodes and busbar are dependent on the length and width of the device, but these can still be small by using a metal with low resistivity and making the grid thick and wide. Because widening the grid increases the shadow losses, a narrow and thick grid is preferred.

With these constraints in mind, two grids were designed, one for a 7 cm^2 device and one for a 36.4 cm^2 device. The 36.4 cm^2 used a grid with finger electrodes and busbar as depicted in Figure 5.4 whereas the 7 cm^2 used a grid based on the unit cell with a busbar running along the edge of the device and not through the middle. Because of this

slight modification, the busbar contribution for the 7 cm^2 device can be ignored and minor changes made to the width when calculating the finger electrode contributions.

Electroplated copper was chosen for the grid metal because of the high conductivity of copper and the ability to electroplate thick, narrow structures through molds, which yields low shadowing and low grid sheet resistance. A finger width of 50 μm and thickness of 5 μm were chosen to keep contact resistance with the ITO low and stress in the thin finger electrodes minimal. Table 5.2 lists all the dimensions and parameters of the devices needed for the power loss calculations.

Table 5.2. Dimensions and parameters for $R_S A$ calculations for the fabricated devices. Length and width for the 7 cm^2 are the same for the active area and the unit cell because of the grid geometry.

Parameter (Units)	Value	Parameter (Units)	Value
w_f (μm)	50	$r_{specific}$ (μΩcm^2)	117
w_b (mm)	6	$R_{sheet\text{-}ITO}$ (Ω/sq.)	13.7
s (mm)	2	ρ_{Cu} (μΩcm)	0.36
t_g (μm)	5	$\rho_P t_P$ (Ωcm^2)	1.4
		$\rho_{C60} t_{c60}$ (Ωcm^2)	1.1
0.11 cm^2 cell, $\alpha = 3$		L (cm)	0.4
		W (cm)	0.28
7 cm^2 cell without grid, $\alpha = 12$		L (cm)	2.85
		W (cm)	2.45
7 cm^2 cell with grid		L (cm)	3.06
		W (cm)	2.3
36.4 cm^2 cell, $\alpha = 12$		L (cm)	6.45
		W (cm)	5.65

Table 5.3 lists the calculated contributions to $R_S A$ for the small- and large-area devices with and without a grid. Though series resistance rapidly increases for the large-area devices without a grid, the calculations suggest the designed grid should keep the

total R_SA of large-area devices similar to that of the small-area device by reducing the ITO contribution. As mentioned before, thin (tens of nanometers) grid structures have been demonstrated to lower the sheet resistance of electrodes in organic solar cells to the order of 10 Ωcm^2. However, this analysis can be used to show that the sheet resistance of these grid electrodes is still too high to keep losses low as the device length is significantly scaled up.

Table 5.3. Calculated contributions to R_SA for small- and large-area devices with and without a metal grid.

Area (cm^2)		Calculated Contributions to R_SA (Ωcm^2)				Total R_SA (Ωcm^2)
		ITO	Organic	Grid	Grid Contact	
0.11		0.73	2.5	-	-	3.2
7	No grid	9.27	2.5	-	-	12
	Grid	0.05	2.5	0.36	0.005	2.9
36.4	No grid	48	2.5	-	-	50
	Grid	0.05	2.5	0.54	0.005	3.1

5.4 Device Performance

5.4.1 Devices without grid

To verify the effect of increasing the ITO area on organic solar cell performance, cells with the structure ITO / pentacene (50 nm) / C_{60} (45 nm) / BCP (8 nm) / Al (200 nm) were fabricated without a metal grid and tested using the dimensions in Table 5.2 (see Section 2.2 for fabrication details). *J-V* characteristics of the devices in the dark and under illumination (Oriel 91160, ~100 mW/cm^2) are shown in Figure 5.6, and the performance parameters for the devices are summarized in Table 5.4. As was expected, the J_{SC}, FF, and η all significantly drop as the active area increases from 0.11 cm^2 up to

36.4 cm^2. Compared to the 0.11 cm^2 cell, the efficiency of the 36.4 cm^2 falls by over 90%, and even the 7 cm^2 cell has an efficiency that is only one-third that of the 0.11 cm^2 device.

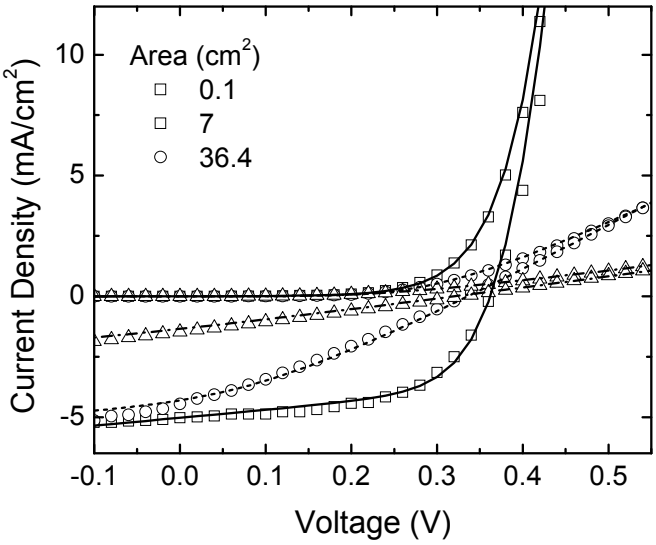

Figure 5.6. Experimental data in the light and dark for pentacene / C_{60} solar cells without a grid and with active areas of 0.11 cm^2 (squares), 7 cm^2 (circles), and 36.4 cm^2 (triangles). Lines are curves fitted to the data with the equivalent circuit model.

Table 5.4. Summary of performance parameters for pentacene / C_{60} solar cells without a grid and with varying active areas.

Area (cm^2)	**J_{SC} (mA/cm^2)**	**V_{OC} (mV)**	***FF***	**$R_S A$ (Ωcm^2)**	**η (%)**
0.11	5.0	368	0.57	1.3	1.2
7	2.5	338	0.29	53	0.41
36.4	1.5	327	0.26	200	0.15

Values of series resistance, calculated by fitting the equivalent circuit model to the experimental data, differ by two orders of magnitude between the 0.11 cm^2 and the 36.4 cm^2 cells (see Table 5.4). Referring to Figure 5.2, the changes in performance are on

par with what was expected from the equivalent circuit model for a small-area cell as $R_S A$ alone is increased. Though the $R_S A$ for the devices differs from what was calculated using the power loss density analysis (see Table 5.3), both sets of values follow the same trends. Discrepancies were expected because the power loss density analysis does not take into account voltage drops along the highly resistive ITO that lead to non-uniform biasing and ultimately affect parameters extracted from the equivalent circuit model. Regardless, the increased series resistance clearly leads to poor performance in the large-area devices.

5.4.2 Devices with grid

To demonstrate the effectiveness of the proposed grid at reducing the contribution to series resistance from ITO for large-area cells, pentacene / C_{60} devices were fabricated with a metal grid and tested using the dimensions in Table 5.2 (see Section 2.2 for fabrication details). Photoresist was used as a passivation layer on top of the grid to prevent shorts between the thick grid (5 μm) and the metal electrode through the thin, vacuum-deposited organic layers (100 nm). Overall, the active area lost from shadowing by the grid and the passivation was 4.6% for the 7 cm^2 cell and 6.6% for the 36.4 cm^2 cell. These losses for the grid are a significant improvement compared to the over 13% loss recently reported for devices in a stripe geometry [51]. Photographs of the completed devices can be found in Figure 5.7.

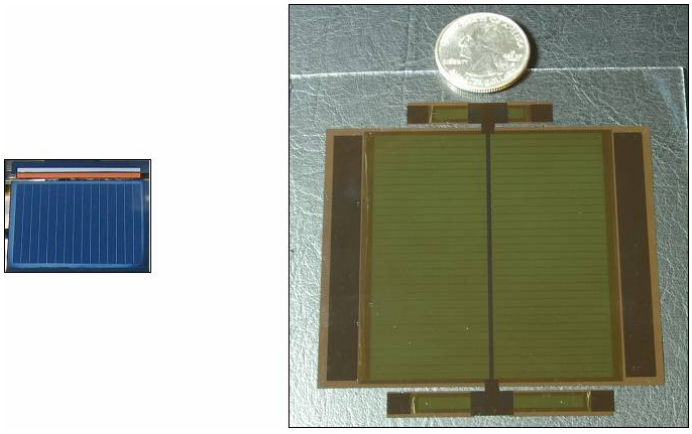

Figure 5.7. Photographs of 7 cm^2 cell (left) and 36.4 cm^2 cell (right) with grid.

Figure 5.8 shows the *J-V* curves of the cells with a grid in the dark and under illumination along with the 0.11 cm^2 cell without a grid as reference. Measurement details are listed in Table 5.5. Inclusion of the grid dramatically improved overall performance of the large-area devices. For the 7 cm^2 device, a reduction of almost one order of magnitude was achieved for R_SA, thereby increasing FF more than 80% and J_{SC} more than 25% even with the shadowing from the metal grids. Overall, the efficiency is greatly increased to 1.0% compared to 0.4% for the 7 cm^2 device without a grid. The 36.4 cm^2 device benefited even more from the grid, and FF and J_{SC} more than doubled to 0.53 and 3.8 mA/cm2 compared to without a grid, thereby increasing the power conversion efficiency to 0.8%. Use of the grid led to large-area devices that exhibited comparable performance to the small-area device in terms of FF and R_SA. However, the photocurrent is still 24% lower for the 36.4 cm^2 device with a grid, which is lower than would be expected based on 6.6% shadowing alone. The origin of these discrepancies is currently under investigation.

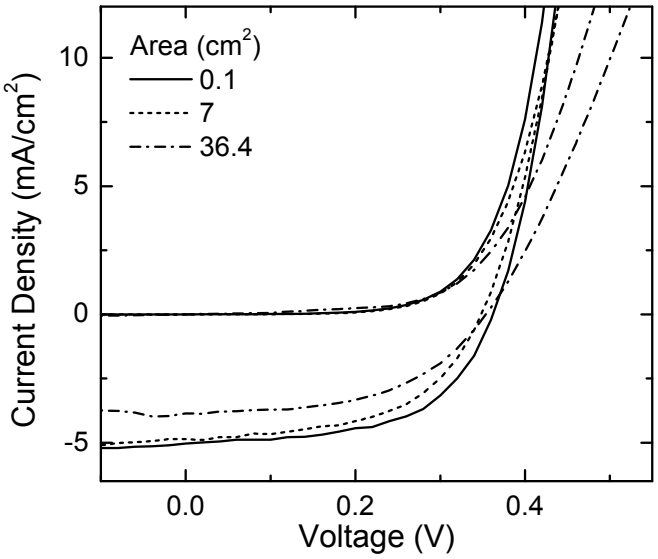

Figure 5.8. Experimental data in the light and dark for pentacene / C_{60} solar cells with a grid and with active areas of 7 cm^2 (dash) and 36.4 cm^2 (dot dash). Also shown is experimental data for the 0.11 cm^2 device without a grid (solid).

Table 5.5. Summary of performance parameters for pentacene / C_{60} solar cells with a grid and with varying active areas.

Area (cm^2)	**J_{SC} (mA/cm^2)**	**V_{OC} (mV)**	***FF***	**$R_S A$ (Ωcm^2)**	**η (%)**
7	4.9	347	0.53	2.5	1.0
36.4	3.8	352	0.53	3.6	0.8

5.5 Conclusions

This chapter demonstrated that a thick, electroplated, metal grid could be used to significantly improve the performance of organic solar cells as the area is increased. Analysis showed that decrease in performance for large-area cells without a grid was primarily caused by an increasing contribution to the series resistance from the transparent electrode with a relatively high sheet resistivity. Inclusion of a thick, high-conductivity grid provides alternative, low-resistance pathways for current in large-area

devices to effectively reduce the contribution to series resistance from the transparent electrodes. While similar grids are also used in inorganic solar cells, organic cells presented unique challenges because of difficulties fabricating a thick, fine grid on top of the active organic layers that are very sensitive to chemical and high-temperature processing. Instead, the grid was fabricated on top of the transparent electrode with the organic layers and metal electrode subsequently deposited. A passivation layer on top of the grid was needed to prevent shorts between the thick grid and metal electrode through the thin organic layers. Large-area devices with grids were found to maintain low series resistance and high efficiency.

The grid solution pursued here has several potential advantages. First, the amount of active area lost because of shadowing or interconnections can be kept low with a thick, narrow grid, only 6.6% for the presented designs. Next, the grid fabrication is independent of the active organic layers. Therefore, the grid could easily be applied to solar cells using newly developed organic materials without any significant modification. Furthermore, the grid can be fabricated and supplied with the substrate and transparent electrode in manufacturing processes separate from the organic layers. Finally, there is the potential to replace the traditionally used the transparent electrode of ITO, which is brittle and expensive, with different transparent conductors. The transparent electrode could even have a higher sheet resistance since the grid significantly shortens the path current has to travel through the resistive layer.

Further research is still needed to understand the uniformity of the organic layers and device performance over large areas. Processing methods to reduce the time and steps needed to make the grid would be of interest; however, maintaining fine features

can be a major challenge. Also, burying the grid in the substrate and depositing the transparent electrode on top would eliminate the need for a passivation layer and could provide additional benefits in terms of uniformity and reliability.

CHAPTER 6

CONCLUSIONS AND RECOMMENDATIONS

6.1 Conclusions

Many solar cell technologies exist for the direct conversion of light into electricity, each with its own advantages and disadvantages. One of the most important metrics for determining the competitiveness of different solar cell technologies is the expected cost per Watt produced. There are many strategies being pursued to achieve cost efficiency such as improving efficiency of standard silicon cells, reducing the amount of expensive raw materials with thin films, developing lower cost manufacturing methods, and designing high-efficiency devices with small areas. Organic solar cells are a newer technology in this field and have the potential for low manufacturing and material costs.

Many challenges still remain for moving organic solar cells from the laboratory into high-volume commercial applications. In particular, some of the needs in organics are a clearer understanding of the device physics, refinement of high-volume fabrication techniques, improvements in overall power conversion efficiency, development of large-area devices, flexible encapsulation, and evaluation and, most likely, improvement of stability under operation. To effectively attack many of these issues, a highly developed sense of the physical and electrical processes in organic solar cells is essential. However, organic semiconductors are still a relatively new field with unique properties, and many of the processes in the devices are still the subject of debate and not clearly understood.

This thesis looked at organic solar cells based on bilayer heterojunctions as model systems to review many of the current theories regarding electrical processes in the devices and to expand on what mechanisms could be responsible for the open-circuit

voltage and reverse saturation current. First, pentacene / C_{60} heterojunctions were considered to demonstrate how well different models for the *J-V* characteristics, photocurrent, and open-circuit voltage apply to experimental data. In many cases, the equivalent circuit model from inorganic solar cells is found to accurately describe the behavior of organic solar cells.

The photocurrent and external quantum efficiency could be well explained in multilayer devices using a one-dimensional exciton diffusion model. While good agreement of the model with experimental data does imply that the applied model for the behavior of excitons has similarities with the reality of what is occurring, many assumptions were used and new results suggest that refinement of the model may be needed to better reflect exciton behavior. For example, new reports point to the possibility of singlet exciton fission into two triplet excitons, which would affect the number of excitons generated from a single photon and their diffusion rate in the model [161]. Furthermore, assumptions were made about exciton quenching at surfaces and efficiency of exciton dissociation at the heterojunction that could be refined with more tests.

On the other hand, the origin of the open-circuit voltage is the subject of more debate. The two primary explanations for the open-circuit voltage are a built-in field, determined by the electrodes or heterojunction [110, 111], or the difference in energy of the HOMO level of the donor and the LUMO of the acceptor minus additional small energy losses [108, 117]. Changing the work function of the electrodes of pentacene / C_{60} cells with different metals and surface modifications, which also have good electrical contact with the organic layers, did not change the open-circuit voltage as would be

expected if determined by a built-in field. When exploring heterojunctions with different donor and acceptor materials, large changes in the open-circuit voltage were obtained. Similar changes in the open-circuit voltage for each donor as the acceptor is replaced with one having a different LUMO value would be expected if the open-circuit voltage is primarily determined by the difference between the HOMO of the donor and the LUMO of the acceptor. Since HOMO and LUMO values cannot be directly measured, experimental values of ionization potential and electron affinity can be used as first approximations for the HOMO and LUMO values, respectively. However, the change in open-circuit voltage for different combinations of donors and acceptors is not always consistent in magnitude or sign with the change in ionization potentials and electron affinities.

To probe the relation between open-circuit voltage and molecular properties more deeply, temperature-dependent measurements of the different heterojunctions were performed. From the *J-V* characteristics and equivalent circuit, the reverse saturation current is known to greatly affect the open-circuit voltage. Study of the reverse saturation current for the different heterojunctions revealed a thermally activated process that could be related to charge transfer at the donor / acceptor interface. The analysis shows that the energy levels are not solely responsible for the open-circuit voltage and that the strength of the electronic coupling between the donor and acceptors is also important. Decreasing the electronic coupling can lead to lower transfer rates and reverse saturation current yielding a higher open-circuit voltage. Indeed, more detailed reports are now starting to be published with more experimental data confirming this shift of understanding the

open-circuit voltage as not just dependent on the energy levels but also the charge transfer complexes and electronic coupling at the donor / acceptor interface [119, 172].

Even as efficiency continues to increase in organic solar cells through improved materials and knowledge of the physical processes, one fundamental way to increase power production that will need to be exploited in practical applications is by simply increasing area. Most reported organic solar cells are still quite small (< 0.1 cm^2), and proportionally increasing the device area without modifications to the geometry decreases performance because of higher series resistance resulting in lower fill factor. One method to limit the resistance losses is using a stripe geometry, but the geometry can suffer from loss of active area. Instead, a grid geometry was borrowed from inorganic solar cells that uses a low resistance metal grid to collect current from the high resistance electrode.

While electrical design of the grid was similar to what has been developed for inorganic solar cells, the geometry had to be modified because of basic differences between inorganic and organic solar cells. Whereas a grid can be fabricated on top of inorganic semiconductors since they are generally hard with good thermal stability, fabrication of a thick metal grid on top of thin, soft, thermally sensitive organic semiconductors is difficult. Instead, the grid had to be fabricated between the transparent electrode, which is on top of the substrate, and organic semiconductors. Application of a passivation layer to prevent shorts between the back metal electrode and the thick metal grid was necessary because of how thin the separating organic semiconductor layers are. Application of the grid yielded significant improvement in the efficiency of large-area solar cells (from 0.4% to 0.8% for a 36 cm^2 cell) that was inline with what was expected from analysis of the grid.

The grid can also be applied to alternative electrodes, even with higher sheet resistance, and to organic semiconductors with higher efficiencies. While ITO with a sheet resistance of 14 Ω/sq. was used here, electrodes with sheet resistances up to 100 Ω/sq. are expected to increase series resistance by only 10% in the grid structure. As ITO, an expensive and brittle semiconductor, is the transparent electrode used in most organic solar cells today, methods that can keep the effective resistance of new transparent electrodes low are very desirable. However, recent discussions with and reviews from others in the field of organic solar cells indicate there is still a misguided focus primarily on the sheet resistance of the transparent electrode even though the analysis here shows that only reduction of sheet resistance by several orders of magnitude, which is highly unlikely, could maintain high performance in large-area devices without a grid.

Many pieces of a large, complex puzzle must come together before organic solar cells see widespread application. The work in this thesis helps to shed light on some of these areas by studying the basic mechanisms present in organic solar cells, extending the scope of processes that should be considered when designing molecules and structures with high open-circuit voltage, and demonstrating how to analyze and improve performance in large-area cells. As organic solar cells continue to be studied and developed, more pieces of the puzzle will come together to lift the technology to new heights. While never expected to be the highest efficiency of the solar technologies, organic solar cells have great potential for many low-cost and light-weight applications. Only time will tell how far organic solar cells will go toward reaching their potential and making an impact.

6.2 Recommendations for Future Work

Several opportunities exist for the continuation of the work in this thesis to further deepen the understanding and development of organic solar cells. One possible avenue would be to continue work with the EQE model to evaluate the actual value and role of some of the boundary conditions that were assumed. For example, layer thickness could be varied and interfaces modified to study exciton recombination at the contacts. Modeling of the EQE at different temperatures could also lead to useful information on properties of the excitons regarding diffusion and dissociation. While carrier collection efficiency is often considered to be high, temperature and thickness dependent measurements could also be used to evaluate the actual collection efficiency and how strategies such as doping affect it.

There are still many other recombination and interfacial properties that could affect open-circuit voltage and need to be investigated in more detail. Relating to the work here, studies on the electronic coupling between donor and acceptor molecules should be continued. Opportunities exist for collaborations between synthetic and theoretical chemists to develop similar compounds with different intermolecular interactions and calculate expected electronic coupling and transfer energies for comparison with experimentally measured results in solar cells. Changes in intermolecular interactions could also potentially be induced by modifying substrates and deposition conditions to control molecule alignment, and the effect on open-circuit voltage can be observed.

Especially at lower temperatures, the equivalent circuit model was found to not always account for all of the features in the *J-V* characteristics of organic heterojunctions. Some basic areas that need improvement are modeling the non-ohmic resistance at high

forward bias and additional humps at low bias. Furthermore, the model often has difficulty in reverse bias, where organic devices tend to have a slightly super-linear slope, and few papers deal with this phenomenon. Many papers also claim a bias dependence of the photocurrent only supported by differences in the *J-V* curves in the light and dark. EQE measurements under bias could be used to better evaluate the bias dependence. Furthermore, EQE measurements under bias could be coupled with the EQE model and measurements at various temperatures to further develop the models for exciton and carrier transport in the devices.

Finally, alternative transparent electrodes using the grid structure to keep series resistance low and minimize the impact of the sheet resistance of the electrode could be explored. Slight modifications may be needed to the grid structure to ensure compatibility with other electrode materials, but cheaper electrodes with higher series resistance could be adopted without a significant drop in performance. One example that is an extension of this work is the use of a solution-processed polymer electrode of PEDOT:PSS with a grid modified to improve connection of the grid to solution-processed electrode [173]. Even with the higher sheet resistance of PEDOT:PSS compared to that of ITO (98 Ω/sq. vs. 14 Ω/sq.), similar performance could be obtained with the inclusion of a grid. Another improvement would be to bury the grid structure within the substrate, but simple fabrication methods for such a structure are not clear at this time.

6.3 List of Publications

Potscavage, W. J., Jr., Sharma, A., & Kippelen, B. (2009). Critical interfaces in organic solar cells and their influence on the open-circuit voltage. *Accounts of Chemical Research*, *42*, 1758-1767.

Choi, S., Potscavage, J., W. J., & Kippelen, B. (2009). Area-scaling of organic solar cells. *Journal of Applied Physics*, *106*, 054507.

Potscavage, W. J., Jr., Yoo, S., & Kippelen, B. (2008). Origin of the open-circuit voltage in multilayer heterojunction organic solar cells. *Applied Physics Letters*, *93*, 193308.

Potscavage, W. J., Yoo, S., Domercq, B., & Kippelen, B. (2007). Encapsulation of pentacene/C_{60} organic solar cells with Al_2O_3 deposited by atomic layer deposition. *Applied Physics Letters*, *90*, 253511.

REFERENCES

[1] Green, M. A. (1998). *Solar cells: Operating principles, technology and system applications*. Kensington: The University of New South Wales.

[2] Hegedus, S. S., & Luque, A. (2003). Status, trends, challenges, and the bright future of solar electricity from photovoltaics. In A. Luque & S. S. Hegedus (Eds.), *Handbook of Photovoltaic Science and Engineering* (pp. 1-43). Hoboken, NJ: John Wiley & Sons.

[3] International Energy Agency. Electricity/heat in world in 2005. Retrieved February 18, 2008, from http://www.iea.org/Textbase/stats/electricitydata.asp?COUNTRY_CODE =29

[4] Markvart, T. (2000). Electricity from the sun. In T. Markvart (Ed.), *Solar Electricity* (pp. 1-4). Chichester, England: John Wiley.

[5] Solarbuzz. Solar cell technologies. Retrieved September 27, 2010, from http://www.solarbuzz.com/Technologies.htm

[6] Green, M. A. (2007). Thin-film solar cells: Review of materials, technologies and commercial status. *Journal of Materials Science: Materials in Electronics*, *18*, S15-S19.

[7] Green, M. A., Emery, K., Hishikawa, Y., & Warta, W. (2010). Solar cell efficiency tables (version 36). *Progress in Photovoltaics: Research and Applications*, *18*, 346-352.

[8] Kurtz, S., & Geisz, J. (2010). Multijunction solar cells for conversion of concentrated sunlight to electricity. *Optics Express*, *18*, A73-A78.

[9] Heliatek. Heliatek and IAPP achieve production-relevant efficiency record for organic photovoltaic cells. Retrieved November 8, 2010, from http://www.heliatek.com/news-19

[10] Pierret, R. F. (1996). *Semiconductor device fundamentals*. New York: Addison-Wesley Publishing Company, Inc.

[11] Tang, C. W. (1986). Two-layer organic photovoltaic cell. *Applied Physics Letters*, *48*, 183-185.

[12] Chamberlain, G. A. (1983). Organic solar cells: A review. *Solar Cells*, *8*, 47-83.

[13] Peumans, P., Bulović, V., & Forrest, S. R. (2000). Efficient photon harvesting at high optical intensities in ultrathin organic double-heterostructure photovoltaic diodes. *Applied Physics Letters*, *76*, 2650-2652.

[14] Peumans, P., & Forrest, S. R. (2001). Very-high-efficiency double-heterostructure copper phthalocyanine/C_{60} photovoltaic cells. *Applied Physics Letters*, *79*, 126-128.

[15] Xue, J., Uchida, S., Rand, B. P., & Forrest, S. R. (2004). 4.2% efficient organic photovoltaic cells with low series resistances. *Applied Physics Letters*, *84*, 3013-3015.

[16] Yoo, S., Domercq, B., & Kippelen, B. (2004). Efficient thin-film organic solar cells based on pentacene/C_{60} heterojunctions. *Applied Physics Letters*, *85*, 5427-5429.

[17] Yoo, S., Potscavage, W. J., Jr., Domercq, B., Han, S.-H., Li, T.-D., Jones, S. C., Szoszkiewicz, R., Levi, D., Riedo, E., Marder, S. R., & Kippelen, B. (2007). Analysis of improved photovoltaic properties of pentacene/C_{60} organic solar cells: Effects of exciton blocking layer thickness and thermal annealing. *Solid-State Electronics*, *51*, 1367-1375.

[18] Chu, C.-W., Shao, Y., Shrotriya, V., & Yang, Y. (2005). Efficient photovoltaic energy conversion in tetracene-C_{60} based heterojunctions. *Applied Physics Letters*, *86*, 243506.

[19] Schulze, K., Uhrich, C., Schüppel, R., Leo, K., Pfeiffer, M., Brier, E., Reinold, E., & Bäuerle, P. (2006). Efficient vacuum-deposited organic solar cells based on a new low-bandgap oligothiophene and fullerene C_{60}. *Advanced Materials*, *18*, 2872-2875.

[20] Cheyns, D., Rand, B. P., & Heremans, P. (2010). Organic tandem solar cells with complementary absorbing layers and a high open-circuit voltage. *Applied Physics Letters*, *97*, 033301.

[21] Wei, G., Wang, S., Renshaw, K., Thompson, M. E., & Forrest, S. R. (2010). Solution-processed squaraine bulk heterojunction photovoltaic cells. *ACS Nano*, *4*, 1927-1934.

[22] Chan, M. Y., Lai, S. L., Fung, M. K., Lee, C. S., & Lee, S. T. (2007). Doping-induced efficiency enhancement in organic photovoltaic devices. *Applied Physics Letters*, *90*, 023504.

[23] Chen, W.-B., Xiang, H.-F., Xu, Z.-X., Yan, B.-P., Roy, V. A. L., Che, C.-M., & Lai, P.-T. (2007). Improving efficiency of organic photovoltaic cells with pentacene-doped CuPc layer. *Applied Physics Letters*, *91*, 191109.

[24] Kinoshita, Y., Hasobe, T., & Murata, H. (2007). Control of open-circuit voltage in organic photovoltaic cells by inserting an ultrathin metal-phthalocyanine layer. *Applied Physics Letters*, *91*, 083518.

[25] Sista, S., Yao, Y., Yang, Y., Tang, M. L., & Bao, Z. (2007). Enhancement in open circuit voltage through a cascade-type energy band structure. *Applied Physics Letters*, *91*, 223508.

[26] Lloyd, M. T., Mayer, A. C., Tayi, A. S., Bowen, A. M., Kasen, T. G., Herman, D. J., Mourey, D. A., Anthony, J. E., & Malliaras, G. G. (2006). Photovoltaic cells from a soluble pentacene derivative. *Organic Electronics*, *7*, 243-248.

[27] Hiramoto, M., Fujiwara, H., & Yokoyama, M. (1991). Three-layered organic solar cell with a photoactive interlayer of codeposited pigments. *Applied Physics Letters*, *58*, 1062-1064.

[28] Peumans, P., Uchida, S., & Forrest, S. R. (2003). Efficient bulk heterojunction photovoltaic cells using small-molecular-weight organic thin films. *Nature*, *425*, 158-162.

[29] Heutz, S., Sullivan, P., Sanderson, B. M., Schultes, S. M., & Jones, T. S. (2004). Influence of molecular architecture and intermixing on the photovoltaic, morphological and spectroscopic properties of CuPc-C_{60} heterojunctions. *Solar Energy Materials & Solar Cells*, *83*, 229-245.

[30] Xue, J. G., Rand, B. P., Uchida, S., & Forrest, S. R. (2005). A hybrid planar-mixed molecular heterojunction photovoltaic cell. *Advanced Materials*, *17*, 66-71.

[31] Yang, F., Shtein, M., & Forrest, S. R. (2005). Controlled growth of a molecular bulk heterojunction photovoltaic cell. *Nature Materials*, *4*, 37-41.

[32] Pfuetzner, S., Meiss, J., Petrich, A., Riede, M., & Leo, K. (2009). Improved bulk heterojunction organic solar cells employing C_{70} fullerenes. *Applied Physics Letters*, *94*, 223307.

[33] Sariciftci, N. S., Braun, D., Zhang, C., Srdanov, V. I., Heeger, A. J., Stucky, G., & Wudl, F. (1993). Semiconducting polymer-buckminsterfullerene heterojunctions: Diodes, photodiodes, and photovoltaic cells. *Applied Physics Letters*, *62*, 585-587.

[34] Halls, J. J. M., Walsh, C. A., Greenham, N. C., Marseglia, E. A., Friend, R. H., Moratti, S. C., & Holmes, A. B. (1995). Efficient photodiodes from interpenetrating polymer networks. *Nature*, *376*, 498-500.

[35] Yu, G., & Heeger, A. J. (1995). Charge separation and photovoltaic conversion in polymer composites with internal donor/acceptor heterojunctions. *Journal of Applied Physics*, *78*, 4510-4515.

[36] Yu, G., Gao, J., Hummelen, J. C., Wudl, F., & Heeger, A. J. (1995). Polymer photovoltaic cells: Enhanced efficiencies via a network of internal donor-acceptor heterojunctions. *Science*, *270*, 1789-1791.

[37] Ma, W., Yang, C., Gong, X., Lee, K., & Heeger, A. J. (2005). Thermally stable, efficient polymer solar cells with nanoscale control of the interpenetrating network morphology. *Advanced Functional Materials*, *15*, 1617-1622.

[38] Li, G., Shrotriya, V., Huang, J., Yao, Y., Moriarty, T., Emery, K., & Yang, Y. (2005). High-efficiency solution processable polymer photovoltaic cells by self-organization of polymer blends. *Nature Materials*, *4*, 864-868.

[39] Peet, J., Kim, J. Y., Coates, N. E., Ma, W. L., Moses, D., Heeger, A. J., & Bazan, G. C. (2007). Efficiency enhancement in low-bandgap polymer solar cells by processing with alkane dithiols. *Nature Materials*, *6*, 497-500.

[40] Liang, Y., Wu, Y., Feng, D., Tsai, S.-T., Son, H.-J., Li, G., & Yu, L. (2009). Development of new semiconducting polymers for high performance solar cells. *Journal of the American Chemical Society*, *131*, 56-57.

[41] Park, S. H., Roy, A., Beaupré, S., Cho, S., Coates, N., Moon, J. S., Moses, D., Leclerc, M., Lee, K., & Heeger, A. J. (2009). Bulk heterojunction solar cells with internal quantum efficiency approaching 100%. *Nature Photonics*, *3*, 297-303.

[42] Peet, J., Soci, C., Coffin, R. C., Nguyen, T. Q., Mikhailovsky, A., Moses, D., & Bazan, G. C. (2006). Method for increasing the photoconductive response in conjugated polymer/fullerene composites. *Applied Physics Letters*, *89*, 252105.

[43] Lee, J. K., Ma, W. L., Brabec, C. J., Yuen, J., Moon, J. S., Kim, J. Y., Lee, K., Bazan, G. C., & Heeger, A. J. (2008). Processing additives for improved efficiency from bulk heterojunction solar cells. *Journal of the American Chemical Society*, *130*, 3619-3623.

[44] Moulé, A. J., Tsami, A., Bünnagel, T. W., Forster, M., Kronenberg, N. M., Scharber, M., Koppe, M., Morana, M., Brabec, C. J., Meerholz, K., & Scherf, U. (2008). Two novel cyclopentadithiophene-based alternating copolymers as potential donor components for high-efficiency bulk-heterojunction-type solar cells. *Chemistry of Materials*, *20*, 4045-4050.

[45] Lee, J. K., Coates, N. E., Cho, S., Cho, N. S., Moses, D., Bazan, G. C., Lee, K., & Heeger, A. J. (2008). Efficacy of TiO_x optical spacer in bulk-heterojunction solar cells processed with 1,8-octanedithiol. *Applied Physics Letters*, *92*, 243308.

[46] Walker, B., Tomayo, A. B., Dang, X.-D., Zalar, P., Seo, J. H., Garcia, A., Tantiwiwat, M., & Nguyen, T.-Q. (2009). Nanoscale phase separation and high photovoltaic efficiency in solution-processed, small-molecule bulk heterojunction solar cells. *Advanced Functional Materials*, *19*, 3063-3069.

[47] Shaheen, S. E., Radspinner, R., Peyghambarian, N., & Jabbour, G. E. (2001). Fabrication of bulk heterojunction plastic solar cells by screen printing. *Applied Physics Letters*, *79*, 2996-2998.

[48] Hoth, C. N., Choulis, S. A., Schilinsky, P., & Brabec, C. J. (2007). High photovoltaic performance of inkjet printed polymer:fullerene blends. *Advanced Materials*, *19*, 3973-3978.

[49] Kopola, P., Aernouts, T., Guillerez, S., Jin, H., Tuomikoski, M., Maaninen, A., & Hast, J. (2010). High efficient plastic solar cells fabricated with a high-throughput gravure printing method. *Solar Energy Materials & Solar Cells*, *94*, 1673-1680.

[50] Kim, S.-S., Na, S.-I., Jo, J., Tae, G., & Kim, D.-Y. (2007). Efficient polymer solar cells fabricated by simple brush painting. *Advanced Materials*, *19*, 4410-4415.

[51] Krebs, F. C., Tromholt, T., & Jørgensen, M. (2010). Upscaling of polymer solar cell fabrication using full roll-to-roll processing. *Nanoscale*, *2*, 873-886.

[52] Hiramoto, M., Suezaki, M., & Yokoyama, M. (1990). Effect of thin gold interstitial-layer on the photovoltaic properties of tandem organic solar cell. *Chemistry Letters*, *3*, 327-330.

[53] Xue, J., Uchida, S., Rand, B. P., & Forrest, S. R. (2004). Asymmetric tandem organic photovoltaic cells with hybrid planar-mixed molecular heterojunctions. *Applied Physics Letters*, *85*, 5757-5759.

[54] Yakimov, A., & Forrest, S. R. (2002). High photovoltage multiple-heterojunction organic solar cells incorporating interfacial metallic nanoclusters. *Applied Physics Letters*, *80*, 1667-1669.

[55] Drechsel, J., Männig, B., Kozlowski, F., Gebeyehu, D., Werner, A., Koch, M., Leo, K., & Pfeiffer, M. (2004). High efficiency organic solar cells based on single or multiple PIN structures. *Thin Solid Films*, *451-452*, 515-517.

[56] Drechsel, J., Männig, B., Kozlowski, F., Pfeiffer, M., Leo, K., & Hoppe, H. (2005). Efficient organic solar cells based on a double *p-i-n* architecture using doped wide-gap transport layers. *Applied Physics Letters*, *86*, 244102.

[57] Schueppel, R., Timmreck, R., Allinger, N., Mueller, T., Furno, M., Uhrich, C., Leo, K., & Riede, M. (2010). Controlled current matching in small molecule

organic tandem solar cells using doped spacer layers. *Journal of Applied Physics*, *107*.

[58] Sato, Y., Yamagishi, K., & Yamashita, M. (2005). Multilayer structure photovoltaic cells. *Optical Review*, *12*, 324-327.

[59] Inoue, J., Yamagishi, K., & Yamashita, M. (2007). Photovoltaic properties of multilayer organic thin films. *Journal of Crystal Growth*, *298*, 782-786.

[60] Cheyns, D., Gommans, H., Odijk, M., Poortmans, J., & Heremans, P. (2007). Stacked organic solar cells based on pentacene and C_{60}. *Solar Energy Materials and Solar Cells*, *91*, 399-404.

[61] Triyana, K., Yasuda, T., Fujita, K., & Tsutsui, T. (2004). Effects of different materials used for internal floating electrode on the photovoltaic properties of tandem type organic solar cell. *Japanese Journal of Applied Physics Part 1: Regular Papers, Short Notes, & Review Papers*, *43*, 2352-2356.

[62] Taima, T., Yamanari, T., Sakai, J., & Yoshida, Y. (2010). Tandem organic photovoltaic cells based on low-molecular-weight semiconductors. *Japanese Journal of Applied Physics*, *49*, 01AC04.

[63] Triyana, K., Yasuda, T., Fujita, K., & Tsutsui, T. (2005). Tandem-type organic solar cells by stacking different heterojunction materials. *Thin Solid Films*, *477*, 198-202.

[64] Dennler, G., Prall, H.-J., Koeppe, R., Egginger, M., Autengruber, R., & Sariciftci, N. S. (2006). Enhanced spectral coverage in tandem organic solar cells. *Applied Physics Letters*, *89*, 073502.

[65] Colsmann, A., Junge, J., Kayser, C., & Lemmer, U. (2006). Organic tandem solar cells comprising polymer and small-molecule subcells. *Applied Physics Letters*, *89*, 203506.

[66] Lee, B. J., Kim, H. J., Jeong, W.-I., & Kim, J.-J. (2010). A transparent conducting oxide as an efficient middle electrode for flexible organic tandem solar cells. *Solar Energy Materials & Solar Cells*, *94*, 542-546.

[67] Kawano, K., Ito, N., Nishimori, T., & Sakai, J. (2006). Open circuit voltage of stacked bulk heterojunction organic solar cells. *Applied Physics Letters*, *88*, 073514.

[68] Sakai, J., Kawano, K., Yamanari, T., Taima, T., Yoshida, Y., Fujii, A., & Ozaki, M. (2010). Efficient organic photovoltaic tandem cells with novel transparent conductive oxide interlayer and poly (3-hexylthiophene): fullerene active layers. *Solar Energy Materials & Solar Cells*, *94*, 376-380.

[69] Hadipour, A., de Boer, B., Wildeman, J., Kooistra, F. B., Hummelen, J. C., Turbiez, M. G. R., Wienk, M. M., Janssen, R. A. J., & Blom, P. W. M. (2006). Solution-processed organic tandem solar cells. *Advanced Functional Materials*, *16*, 1897-1903.

[70] Hadipour, A., de Boer, B., & Blom, P. W. M. (2007). Solution-processed organic tandem solar cells with embedded optical spacers. *Journal of Applied Physics*, *102*, 074506.

[71] Sista, S., Park, M.-H., Hong, Z., Wu, Y., Hou, J., Kwan, W. L., Li, G., & Yang, Y. (2010). Highly efficient tandem polymer photovoltaic cells. *Advanced Materials*, *22*, 380-383.

[72] Gilot, J., Wienk, M. M., & Janssen, R. A. J. (2007). Double and triple junction polymer solar cells processed from solution. *Applied Physics Letters*, *90*, 143512.

[73] Gilot, J., Wienk, M. M., & Janssen, R. A. J. (2010). Optimizing polymer tandem solar cells. *Advanced Materials*, *22*, E67-E71.

[74] Kim, J. Y., Lee, K., Coates, N. E., Moses, D., Nguyen, T.-Q., Dante, M., & Heeger, A. J. (2007). Efficient tandem polymer solar cells fabricated by all-solution processing. *Science*, *317*, 222-225.

[75] Yang, F., Sun, K., & Forrest, S. R. (2007). Efficient solar cells using all-organic nanocrystalline networks. *Advanced Materials*, *19*, 4166-4171.

[76] Forbes. Solarmer Energy, Inc. Breaks Psychological Barrier with 8.13% OPV Efficiency. Retrieved September 18, 2010, from http://www.forbes.com/feeds/businesswire/2010/07/27/businesswire142993163.html

[77] Neugebauer, H., Brabec, C., Hummelen, J. C., & Sariciftci, N. S. (2000). Stability and photodegradation mechanisms of conjugated polymer/fullerene plastic solar cells. *Solar Energy Materials & Solar Cells*, *61*, 35-42.

[78] Krebs, F. C., Carlé, J. E., Cruys-Bagger, N., Andersen, M., Lilliedal, M. R., Hammond, M. A., & Hvidt, S. (2005). Lifetimes of organic photovoltaics: Photochemistry, atmosphere effects and barrier layers in ITO-MEHPPV:PCBM-aluminium devices. *Solar Energy Materials & Solar Cells*, *86*, 499-516.

[79] Madakasira, P., Inoue, K., Ulbricht, R., Lee, S. B., Zhou, M., Ferraris, J. P., & Zakhidov, A. A. (2005). Multilayer encapsulation of plastic photovoltaic devices. *Synthetic Metals*, *155*, 332-335.

[80] Potscavage, W. J., Yoo, S., Domercq, B., & Kippelen, B. (2007). Encapsulation of pentacene/C_{60} organic solar cells with Al_2O_3 deposited by atomic layer deposition. *Applied Physics Letters*, *90*, 253511.

[81] Waldauf, C., Morana, M., Denk, P., Schilinsky, P., Coakley, K., Choulis, S. A., & Brabec, C. J. (2006). Highly efficient inverted organic photovoltaics using solution based titanium oxide as electron selective contact. *Applied Physics Letters*, *89*.

[82] White, M. S., Olson, D. C., Shaheen, S. E., Kopidakis, N., & Ginley, D. S. (2006). Inverted bulk-heterojunction organic photovoltaic device using a solution-derived ZnO underlayer. *Applied Physics Letters*, *89*, 143517.

[83] Dennler, G., Lungenschmied, C., Neugebauer, H., Sariciftci, N. S., & Labouret, A. (2005). Flexible, conjugated polymer-fullerene-based bulk-heterojunction solar cells: Basics, encapsulation, and integration. *Journal of Materials Research*, *20*, 3224-3233.

[84] Lewis, J. S., & Weaver, M. S. (2004). Thin-film permeation-barrier technology for flexible organic light-emitting devices. *IEEE Journal of Selected Topics in Quantum Electronics*, *10*, 45-57.

[85] Yun, S. J., Ko, Y.-W., & Lim, J. W. (2004). Passivation of organic light-emitting diodes with aluminum oxide thin films grown by plasma-enhanced atomic layer deposition. *Applied Physics Letters*, *85*, 4896-4898.

[86] Huang, W., Wang, X., Sheng, M., Xu, L., Stubhan, F., Luo, L., Feng, T., Wang, X., Zhang, F., & Zou, S. (2003). Low temperature PECVD SiN_x films applied in OLED packaging. *Materials Science and Engineering B*, *98*, 248-254.

[87] Mandlik, P., Gartside, J., Han, L., Cheng, I.-C., Wagner, S., Silvernail, J. A., Ma, R.-Q., Hack, M., & Brown, J. J. (2008). A single-layer permeation barrier for organic light-emitting displays. *Applied Physics Letters*, *92*, 103309.

[88] Park, S.-H. K., Oh, J., Hwang, C.-S., Lee, J.-I., Yang, Y. S., & Chu, H. Y. (2005). Ultrathin film encapsulation of an OLED by ALD. *Electrochemical and Solid-State Letters*, *8*, H21-H23.

[89] Park, S.-H. K., Oh, J., Hwang, C.-S., Lee, J.-I., Yang, Y. S., Chu, H. Y., & Kang, K.-Y. (2005). Ultra thin film encapsulation of organic light emitting diode on a plastic substrate. *ETRI Journal*, *27*, 545-550.

[90] Ghosh, A. P., Gerenser, L. J., Jarman, C. M., & Fornalik, J. E. (2005). Thin-film encapsulation of organic light-emitting devices. *Applied Physics Letters*, *86*, 223503.

[91] Chwang, A. B., Rothman, M. A., Mao, S. Y., Hewitt, R. H., Weaver, M. S., Silvernail, J. A., Rajan, K., Hack, M., Brown, J. J., Chu, X., Moro, L., Krajewski, T., & Rutherford, N. (2003). Thin film encapsulated flexible organic electroluminescent displays. *Applied Physics Letters*, *83*, 413-415.

[92] Kim, N., Potscavage, W. J., Jr., Domercq, B., Kippelen, B., & Graham, S. (2009). A hybrid encapsulation method for organic electronics. *Applied Physics Letters*, *94*, 163308.

[93] Chang, C.-Y., Chou, C.-T., Lee, Y.-J., Chen, M.-J., & Tsai, F.-Y. (2009). Thin-film encapsulation of polymer-based bulk-heterojunction photovoltaic cells by atomic layer deposition. *Organic Electronics*, *10*, 1300-1306.

[94] Weaver, M. S., Michalski, L. A., Rajan, K., Rothman, M. A., Silvernail, J. A., Brown, J. J., Burrows, P. E., Graff, G. L., Gross, M. E., Martin, P. M., Hall, M., Mast, E., Bonham, C., Bennett, W., & Zumhoff, M. (2002). Organic light-emitting devices with extended operating lifetimes on plastic substrates. *Applied Physics Letters*, *81*, 2929-2931.

[95] Yan, M., Kim, T. W., Erlat, A. G., Pellow, M., Foust, D. F., Liu, H., Schaepkens, M., Heller, C. M., McConnelee, P. A., Feist, T. P., & Duggal, A. R. (2005). A transparent, high barrier, and high heat substrate for organic electronics. *Proceedings of the IEEE*, *93*, 1468-1477.

[96] Krebs, F. C., Spanggard, H., Kjær, T., Biancardo, M., & Alstrup, J. (2007). Large area plastic solar cell modules. *Materials Science and Engineering B*, *138*, 106-111.

[97] Lungenschmied, C., Dennler, G., Neugebauer, H., Sariciftci, S. N., Glatthaar, M., Meyer, T., & Meyer, A. (2007). Flexible, long-lived, large-area, organic solar cells. *Solar Energy Materials & Solar Cells*, *91*, 379-384.

[98] Niggemann, M., Zimmermann, B., Haschke, J., Glatthaar, M., & Gombert, A. (2008). Organic solar cell modules for specific applications - From energy autonomous systems to large area photovoltaics. *Thin Solid Films*, *516*, 7181-7187.

[99] Tipnis, R., Bernkopf, J., Jia, S., Krieg, J., Li, S., Storch, M., & Laird, D. (2009). Large-area organic photovoltaic module - Fabrication and performance. *Solar Energy Materials & Solar Cells*, *93*, 442-446.

[100] Wöhrle, D., Kreienhoop, L., Schnurpfeil, G., Elbe, J., Tennigkeit, B., Hiller, S., & Schlettwein, D. (1995). Investigations of n/p-junction photovoltaic cells of perylenetetracarboxylic acid diimides and phthalocyanines. *Journal of Materials Chemistry*, *5*, 1819-1829.

[101] Salzman, R. F., Xue, J., Rand, B. P., Alexander, A., Thompson, M. E., & Forrest, S. R. (2005). The effects of copper phthalocyanine purity on organic solar cell performance. *Organic Electronics*, *6*, 242-246.

[102] Forrest, S. R. (1997). Ultrathin organic films grown by organic molecular beam deposition and related techniques. *Chemical Reviews*, *97*, 1793-1896.

[103] Park, J. Y., & Allen, M. G. (2000). Integrated electroplated micromachined magnetic devices using low temperature fabrication processes. *IEEE Transactions on Electronics Packaging Manufacturing*, *23*, 48-55.

[104] Shrotriya, V., Li, G., Yao, Y., Moriarty, T., Emery, K., & Yang, Y. (2006). Accurate measurement and characterization of organic solar cells. *Advanced Functional Materials*, *16*, 2016-2023.

[105] Schroder, D. K. (2001). Surface voltage and surface photovoltage: History, theory and applications. *Measurement Science and Technology*, *12*, R16-R31.

[106] Brédas, J.-L., Norton, J. E., Cornil, J., & Coropceanu, V. (2009). Molecular understanding of organic solar cells: The challenges. *Accounts of Chemical Research*, *42*, 1691-1699.

[107] Zahn, D. R. T., Gavrila, G. N., & Gorgoi, M. (2006). The transport gap of organic semiconductors studied using the combination of direct and inverse photoemission. *Chemical Physics*, *325*, 99-112.

[108] Rand, B. P., Burk, D. P., & Forrest, S. R. (2007). Offset energies at organic semiconductor heterojunctions and their influence on the open-circuit voltage of thin-film solar cells. *Physical Review B*, *75*, 115327.

[109] Kippelen, B., & Brédas, J.-L. (2009). Organic photovoltaics. *Energy & Environmental Science*, *2*, 251-261.

[110] Ramsdale, C. M., Barker, J. A., Arias, A. C., MacKenzie, J. D., Friend, R. H., & Greenham, N. C. (2002). The origin of the open-circuit voltage in polyfluorene-based photovoltaic devices. *Journal of Applied Physics*, *92*, 4266-4270.

[111] Brabec, C. J., Cravino, A., Meissner, D., Sariciftci, N. S., Fromherz, T., Rispens, M. T., Sanchez, L., & Hummelen, J. C. (2001). Origin of the open circuit voltage of plastic solar cells. *Advanced Functional Materials*, *11*, 374-380.

[112] Mihailetchi, V. D., Blom, P. W. M., Hummelen, J. C., & Rispens, M. T. (2003). Cathode dependence of the open-circuit voltage of polymer:fullerene bulk heterojunction solar cells. *Journal of Applied Physics*, *94*, 6849-6854.

[113] Kietzke, T., Egbe, D. A. M., Hörhold, H.-H., & Neher, D. (2006). Comparative study of M3EH-PPV-based bilayer photovoltaic devices. *Macromolecules*, *39*, 4018-4022.

[114] Brumbach, M., Placencia, D., & Armstrong, N. R. (2008). Titanyl phthalocyanine/C_{60} heterojunctions: Band-edge offsets and photovoltaic device performance. *Journal of Physical Chemistry C*, *112*, 3142-3151.

[115] Gadisa, A., Svensson, M., Andersson, M. R., & Inganäs, O. (2004). Correlation between oxidation potential and open-circuit voltage of composite solar cells based on blends of polythiophenes/fullerene derivative. *Applied Physics Letters*, *84*, 1609-1611.

[116] Deng, X., Zheng, L., Yang, C., Li, Y., Yu, G., & Cao, Y. (2004). Polymer photovoltaic devices fabricated with blend MEHPPV and organic small molecules. *Journal of Physical Chemistry B*, *108*, 3451-3456.

[117] Scharber, M. C., Mühlbacher, D., Koppe, M., Denk, P., Waldauf, C., Heeger, A. J., & Brabec, C. J. (2006). Design rules for donors in bulk-heterojunction solar cells - Towards 10 % energy-conversion efficiency. *Advanced Materials*, *18*, 789-794.

[118] Kooistra, F. B., Knol, J., Kastenberg, F., Popescu, L. M., Verhees, W. J. H., Kroon, J. M., & Hummelen, J. C. (2007). Increasing the open circuit voltage of bulk-heterojunction solar cells by raising the LUMO level of the acceptor. *Organic Letters*, *9*, 551-554.

[119] Vandewal, K., Tvingstedt, K., Gadisa, A., Inganäs, O., & Manca, J. V. (2009). On the origin of the open-circuit voltage of polymer-fullerene solar cells. *Nature Materials*, *8*, 904-909.

[120] Yoo, S., Domercq, B., & Kippelen, B. (2005). Intensity-dependent equivalent circuit parameters of organic solar cells based on pentacene and C_{60}. *Journal of Applied Physics*, *97*, 103706.

[121] Shrotriya, V., Wu, E. H.-E., Li, G., Yao, Y., & Yang, Y. (2006). Efficient light harvesting in multiple-device stacked structure for polymer solar cells. *Applied Physics Letters*, *88*, 064104.

[122] Gadisa, A., Tvingstedt, K., Admassie, S., Lindell, L., Crispin, X., Andersson, M. R., Salaneck, W. R., & Inganäs, O. (2006). Transparent polymer cathode for organic photovoltaic devices. *Synthetic Metals*, *156*, 1102-1107.

[123] Ng, G.-M., Kietzke, E. L., Kietzke, T., Tan, L.-W., Liew, P.-K., & Zhu, F. (2007). Optical enhancement in semitransparent polymer photovoltaic cells. *Applied Physics Letters*, *90*, 103505.

[124] Zhou, Y., Li, F., Barrau, S., Tian, W., Inganäs, O., & Zhang, F. (2009). Inverted and transparent polymer solar cells prepared with vacuum-free processing. *Solar Energy Materials and Solar Cells*, *93*, 497-500.

[125] Nickel, F., Puetz, A., Reinhard, M., Do, H., Kayser, C., Colsmann, A., & Lemmer, U. (2010). Cathodes comprising highly conductive poly(3,4-ethylenedioxythiophene): poly(styrenesulfonate) for semi-transparent polymer solar cells. *Organic Electronics*, *11*, 535-538.

[126] Lee, J.-Y., Connor, S. T., Cui, Y., & Peumans, P. (2010). Semitransparent organic photovoltaic cells with laminated top electrode. *Nano Letters*, *10*, 1276-1279.

[127] Nelson, J., Kirkpatrick, J., & Ravirajan, P. (2004). Factors limiting the efficiency of molecular photovoltaic devices. *Physical Review B*, *69*, 035337.

[128] Koehler, M., Roman, L. S., Inganäs, O., & da Luz, M. G. E. (2004). Modeling bilayer polymer/fullerene photovoltaic devices. *Journal of Applied Physics*, *96*, 40-43.

[129] Koster, L. J. A., Smits, E. C. P., Mihailetchi, V. D., & Blom, P. W. M. (2005). Device model for the operation of polymer/fullerene bulk heterojunction solar cells. *Physical Review B*, *72*, 085205.

[130] Martin, C. M., Burlakov, V. M., Assender, H. E., & Barkhouse, D. A. R. (2007). A numerical model for explaining the role of the interface morphology in composite solar cells. *Journal of Applied Physics*, *102*, 104506.

[131] Schilinsky, P., Waldauf, C., Hauch, J., & Brabec, C. J. (2004). Simulation of light intensity dependent current characteristics of polymer solar cells. *Journal of Applied Physics*, *95*, 2816-2819.

[132] Riedel, I., Parisi, J., Dyakonov, V., Lutsen, L., Vanderzande, D., & Hummelen, J. C. (2004). Effect of temperature and illumination on the electrical characteristics of polymer-fullerene bulk-heterojunction solar cells. *Advanced Functional Materials*, *14*, 38-44.

[133] Rostalski, J., & Meissner, D. (2000). Photocurrent spectroscopy for the investigation of charge carrier generation and transport mechanisms in organic p/n-junction solar cells. *Solar Energy Materials and Solar Cells*, *63*, 37-47.

[134] Huynh, W. U., Dittmer, J. J., Teclemariam, N., Milliron, D. J., Alivisatos, A. P., & Barnham, K. W. J. (2003). Charge transport in hybrid nanorod-polymer composite photovoltaic cells. *Physical Review B*, *67*, 115326.

[135] Pettersson, L. A. A., Roman, L. S., & Inganäs, O. (1999). Modeling photocurrent action spectra of photovoltaic devices based on organic thin films. *Journal of Applied Physics*, *86*, 487-496.

[136] Yoo, S. (2005). *Organic solar cells based on liquid crystalline and polycrystalline thin films.* Doctoral dissertation, The University of Arizona, Tuscon.

[137] Peumans, P., Yakimov, A., & Forrest, S. R. (2003). Small molecular weight organic thin-film photodetectors and solar cells. *Journal of Applied Physics*, *93*, 3693-3723.

[138] Sharma, A., Haldi, A., Hotchkiss, P. J., Marder, S. R., & Kippelen, B. (2009). Effect of phosphonic acid surface modifiers on the work function of indium tin oxide and on the charge injection barrier into organic single-layer diodes. *Journal of Applied Physics*, *105*, 074511.

[139] Sharma, A., Hotchkiss, P. J., Marder, S. R., & Kippelen, B. (2009). Tailoring the work function of indium tin oxide electrodes in electrophosphorescent organic light-emitting diodes. *Journal of Applied Physics*, *105*, 084507.

[140] Sharma, A., Haldi, A., Potscavage, W. J., Jr., Hotchkiss, P. J., Marder, S. R., & Kippelen, B. (2009). Effects of surface modification of indium tin oxide electrodes on the performance of molecular multilayer organic photovoltaic devices. *Journal of Materials Chemistry*, *19*, 5298-5302.

[141] Pandey, A. K., Shaw, P. E., Samuel, I. D. W., & Nunzi, J.-M. (2009). Effect of metal cathode reflectance on the exciton-dissociation efficiency in heterojunction organic solar cells. *Applied Physics Letters*, *94*, 103303.

[142] Kao, P.-C., Chu, S.-Y., Liu, S.-J., You, Z.-X., & Chuang, C.-A. (2006). Improved performance of organic light-emitting diodes using a metal-phthalocyanine hole-injection layer. *Journal of the Electrochemical Society*, *153*, H122-H126.

[143] Tanaka, H., Yasuda, T., Fujita, K., & Tsutsui, T. (2006). High efficiency polarization-sensitive organic photovoltaic devices. *Applied Physics Letters*, *88*, 253506.

[144] Haldi, A., Sharma, A., Potscavage, W. J., Jr., & Kippelen, B. (2008). Equivalent circuit model for organic single-layer diodes. *Journal of Applied Physics*, *104*, 064503.

[145] Sze, S. M., & Ng, K. K. (2007). *Physics of semiconductor devices*. Hoboken, NJ: John Wiley & Sons.

[146] Rhoderick, E. H. (1982). Metal-semiconductor contacts. *IEE Proceedings*, *129*, 1-14.

[147] Fahrenbruch, A., & Bube, R. H. (1983). *Fundamentals of solar cells: Photovoltaic solar energy conversion*. New York: Academic Press.

[148] Phillips, J. E., Birkmire, R. W., McCandless, B. E., Meyers, P. V., & Shafarman, W. N. (1996). Polycrystalline heterojunction solar cells: A device perspective. *Physica Status Solidi (b)*, *194*, 31-39.

[149] Hegedus, S. S., & Shafarman, W. N. (2004). Thin-film solar cells: Device measurements and analysis. *Progress in Photovoltaics*, *12*, 155-176.

[150] Drori, T., Sheng, C.-X., Ndobe, A., Singh, S., Holt, J., & Vardeny, Z. V. (2008). Below-gap excitation of π-conjugated polymer-fullerene blends: Implications for bulk organic heterojunction solar cells. *Physical Review Letters*, *101*, 037401.

[151] Brédas, J.-L., Beljonne, D., Coropceanu, V., & Cornil, J. (2004). Charge-transfer and energy-transfer processes in π-conjugated oligomers and polymers: A molecular picture. *Chemical Reviews*, *104*, 4971-5003.

[152] Kim, K., Kwak, T. H., Cho, M. Y., Lee, J. W., & Joo, J. (2008). Comparison of electrical characteristics for p-type and n-type organic thin film transistors using copper phthalocyanine. *Synthetic Metals*, *158*, 553-555.

[153] Dunn, L., & Dodabalapur, A. (2010). Temperature dependent transient velocity and mobility studies in an organic field effect transistor. *Journal of Applied Physics*, *107*.

[154] McCandless, B. E., & Sites, J. R. (2003). Cadmium telluride solar cells. In A. Luque & S. S. Hegedus (Eds.), *Handbook of Photovoltaic Science and Engineering* (pp. 617-662). Hoboken, NJ: John Wiley & Sons.

[155] Chikamatsu, M., Taima, T., Yoshida, Y., Saito, K., & Yase, K. (2004). Mg-doped C_{60} thin film as improved *n*-type organic semiconductor for a solar cell. *Applied Physics Letters*, *84*, 127-129.

[156] Glatthaar, M., Riede, M., Keegan, N., Sylvester-Hvid, K., Zimmermann, B., Niggemann, M., Hinsch, A., & Gombert, A. (2007). Efficiency limiting factors of organic bulk heterojunction solar cells identified by electrical impedance spectroscopy. *Solar Energy Materials & Solar Cells*, *91*, 390-393.

[157] Zhou, Y., Cheun, H., Potscavage, W. J., Jr., Fuentes-Hernandez, C., Kim, S.-J., & Kippelen, B. (2010). Inverted organic solar cells with ITO electrodes modified with an ultrathin Al_2O_3 buffer layer deposited by atomic layer deposition. *Journal of Materials Chemistry*, *20*, 6189-6194.

[158] Stiebig, H., Eickhoff, T., Zimmer, J., Beneking, C., & Wagner, H. (1996). Measured and simulated temperature dependence of a-Si:H solar cell parameters. *Materials Research Society Symposium Proceedings*, *426*, 19-24.

[159] Contreras, M. A., Nakada, T., Hongo, M., Pudov, A. O., & Sites, J. R. (2003). ZnO/ZnS(O,OH)/Cu(In,Ga)Se_2/Mo solar cell with 18.6% efficiency. *Proceedings of 3rd World Conference on Photovoltaic Energy Conversion*, *1*, 570-573.

[160] Kulkarni, S. S. (2008). *Effect of composition, morphology and semiconducting properties on the efficiency of* $CuIn_{1-x}Ga_xSe_{2-y}S_y$ *thin-film solar cells prepared by rapid thermal processing.* Doctoral dissertation, The University of Central Florida, Orlando.

[161] Rao, A., Wilson, M. W. B., Hodgkiss, J. M., Albert-Seifried, S., Bässler, H., & Friend, R. H. (2010). Exciton fission and charge generation via triplet excitons in pentacene/C_{60} bilayers. *Journal of the American Chemical Society*, *132*, 12698-12703.

[162] Gupta, D., Bag, M., & Narayan, K. S. (2008). Area dependent efficiency of organic solar cells. *Applied Physics Letters*, *93*, 163301.

[163] Pandey, A. K., Nunzi, J. M., Ratier, B., & Moliton, A. (2008). Size effect on organic optoelectronics devices: Example of photovoltaic cell efficiency. *Physics Letters A*, *372*, 1333-1336.

[164] Meier, D. L., & Schroder, D. K. (1984). Contact resistance: Its measurement and relative importance to power loss in a solar cell. *IEEE Transactions on Electron Devices*, *31*, 647-653.

[165] Aernouts, T., Vanlaeke, P., Geens, W., Poortmans, J., Heremans, P., Borghs, S., Mertens, R., Andriessen, R., & Leenders, L. (2004). Printable anodes for flexible organic solar cell modules. *Thin Solid Films*, *451-452*, 22-25.

[166] Glatthaar, M., Niggemann, M., Zimmermann, B., Lewer, P., Riede, M., Hinsch, A., & Luther, J. (2005). Organic solar cells using inverted layer sequence. *Thin Solid Films*, *491*, 298-300.

[167] Tvingstedt, K., & Inganäs, O. (2007). Electrode grids for ITO-free organic photovoltaic devices. *Advanced Materials*, *19*, 2893-2897.

[168] Kang, M.-G., Kim, M.-S., Kim, J. S., & Guo, L. J. (2008). Organic solar cells using nanoimprinted transparent metal electrodes. *Advanced Materials*, *20*, 4408-4413.

[169] Steim, R., Schilinsky, P., Choulis, S. A., & Brabec, C. J. (2009). Flexible polymer photovoltaic modules with incorporated organic bypass diodes to address module shading effects. *Solar Energy Materials & Solar Cells*, *93*, 1963-1967.

[170] Zimmermann, B., Glatthaar, M., Niggemann, M., Riede, M. K., Hinsch, A., & Gombert, A. (2007). ITO-free wrap through organic solar cells - A module concept for cost-efficient reel-to-reel production. *Solar Energy Materials and Solar Cells*, *91*, 374-378.

[171] Serreze, H. B. (1978). Optimizing solar cell performance by simultaneous consideration of grid pattern design and interconnect configuration. *Conference Record of the Thirteenth IEEE Photovoltaic Specialists Conference*, 609-614.

[172] Perez, M. D., Borek, C., Forrest, S. R., & Thompson, M. E. (2009). Molecular and morphological influences on the open circuit voltages of organic photovoltaic devices. *Journal of the American Chemical Society*, *131*, 9281-9286.

[173] Choi, S., Potscavage, W. J., Jr., & Kippelen, B. (2010). ITO-free large-area organic solar cells. *Optics Express*, *18*, A458-A466.